CZTS (Cu_2ZnSnS_4) photocathode for solar energy conversion and storage

by

Animesh Mondal

A dissertation submitted to the Graduate Faculty of
Auburn University
in partial fulfillment of the
requirements for the Degree of
Doctor of Philosophy
Auburn, Alabama
May 4, 2019

Approved by

James G. Radich, Chair, Assistant Professor, Chemical Engineering
Bryan Beckingham, Co-chair, Assistant Professor, Chemical Engineering
Allan David, John W. Brown Associate Professor, Chemical Engineering
Xinyu Zhang, Associate Professor, Chemical Engineering
Bart Prorok, Professor, Director, Analytical Microscopy Center, Mechanical Engineering

Abstract

Sunlight provides abundant, renewable energy on earth's surface. Photoelectrochemical photovoltaic cells (PEPC) are one of the most convenient ways to capture this solar energy and convert into electricity. Cu_2ZnSnS_4 (CZTS) is a p-type semiconductor which holds great opto-electronic and economic advantages over traditional solar absorbing materials such as silicon. The elements in CZTS are earth abundant and environment friendly and CZTS has an energy band gap of ~1.5 eV which is considered to be optimum for solar absorption. The high absorption coefficient ~ 10^4 cm^{-1} of CZTS thin films allow for 95% absorption of the incident energy within 1μm. However, there are significant challenges with CZTS in separating the photogenerated charge carriers. These challenges results from the narrow thermodynamic window for chemical stability and the high density of intrinsic defects within the film. During the deposition of this quaternary material, domains of binary compounds develop within the thin film. The interface between these binary impurities and quaternary CZTS induces recombination of the charge carriers that are generated through the absorption of light.

To minimize the impure phases, we developed a facile and reproducible CZTS thin film deposition protocol using an air stable precursor solution. Initially, the solution was sprayed onto a preheated FTO substrate for instantaneous film deposition. The film was then annealed under S and SnS atmosphere at 470 ºC with inert gas (N_2) flow. The precursor composition was varied to study evolution of impure phases with compositional changes in the film. The thin film was employed as a photocathode in a three-electrode photoelectrochemical cell (PEC) to study the electrode performance as a solar absorbing layer.

The thin film deposited using the precursor solution requires high temperature annealing which is energy intensive. In a different approach, CZTS nanocrystals can be presynthesized in the solution at low temperature (~270^{o}C). Cu_2ZnSnS_4 (CZTS) nanocrystals are important materials for next generation solar energy capture and conversion strategies. However, progress in utilizing CZTS nanocrystals is impeded by the numerous crystal and morphological defects present without high temperature annealing. These defects commonly result in reduced carrier diffusion length and carrier lifetime. One recent and promising direction for employing CZTS nanocrystals in solar energy capture and conversion strategies is through remediation of defects by doping with alkali Earth metal ions such as Li^+, Na^+, and/or K^+. We focused on the K^+ cationic doping since it has demonstrated the highest efficiencies but without fundamental investigation into the underlying drivers. A flexible and reproducible synthesis route was developed to prepare K^+-doped CZTS nanocrystals with low polydispersity. We employed undoped and K^+-doped nanocrystals to fabricate CZTS photocathodes and evaluated their photoresponsiveness in a photoelectrochemical cell. K^+-doped CZTS nanocrystals showed the previously-reported trend of improved photocurrent density. We obtained further insight into the role of K^+ dopant using Raman spectroscopy, x-ray photoelectron spectroscopy, and transient absorption spectroscopy. K^+-doping of CZTS nanocrystals boosts charge carrier lifetime and enables better charge extraction efficiency to boost photocurrent. Improved carrier lifetime is attributed to remediation of binary/tertiary impurity phases and surface anion vacancies to yield higher degree of phase purity and lower degree of surface electron traps in CZTS. Ligand exchange reactions using Na_2S and pyridine have been exploited to reduce the carbon content which serves as the recombination site for the charge carriers.

The selenized CZTS nanocrystal (CZTSSe) provides an opportunity for tuning the band gap energy of the thin film. Achieving a homogenous precursor solution of selenium in organic solvent (high boiling point) is vital to the synthesis of CZTSSe nanocrystals. We dissolved elemental Se in oleylamine at room temperature by using thioacetamide as a reducing agent. The Se precursor was utilized to synthesize selenized CZTS nanocrystals via hot injection route. The characterization of nanocrystals revealed improved grain growth and reduced binary phases in CZTSSe compared to pristine CZTS. The electrodes of CZTSSe nanocrystal showed significant improvement on photocurrent generation over the CZTS counterparts under AM1.5 illumination.

Cost-effective industrial-scale energy storage system is a great challenge for accommodating contributions from unpredictable renewable sources (solar, wind, and hydro) to the power grid. Polysulfide (S_n^{2-}/S_{n-1}^{2-}) redox couple has received much attention among researchers as an affordable energy storing system. Sulfur, a by-product in crude oil production, is considered a cheap industrial waste with potential for megawatt scale energy storage systems such as redox flow batteries (RFB). We demonstrate photo-assisted reduction of polysulfide by developing a Cu_2ZnZnS_4 (CZTS) nanocrystal-based photocathode which provides opportunities for in-situ solar energy conversion and storage in a polysulfide based solar rechargeable RFB. The electrode performance was improved first by doping the nanocrystal with K^+ and then by using Cu^+ as an electrocatalyst. Electrochemical tools were used to show that Cu^+ dramatically reduces electrode overpotential by reducing charge transfer resistance. The electron injection rate was probed using ultrafast laser absorption spectroscopy which reveals that K^+-CZTS\Cu^+ electrodes show 8 times faster electron injection rates than the bare K^+-CZTS electrode.

Acknowledgments

I would like to express my deepest gratitude to my academic advisor Dr. James G. Radich for his supervision during my doctoral study.

I would also express gratitude to my committee members, Dr. Bryan Beckingham, Dr. Allan David, Dr. Bart Prorok, and Dr. Xinyu Zhang for their professional advice. A special thanks to Dr. Zhongyang Cheng for being the university reader of my dissertation.

I acknowledge the support by the department of chemical engineering at Auburn University for funding the equipment and supplies required for this research. Furthermore, I would like to thank all my collaborators Dr. Mehmet Zeki Billor, Dr. Carlos Carrero, Dr. Virginia Davis, Dr. Tae-Sik Oh, Dr. Bruce Tatarchuk, Dr. Curtis Shannon, Dr. Michael Miller, Dr. Joyanta Goswami, Mingyang Chi, Jorge Moncada, and Steven Moore.

I appreciate the professional assistance from my lab mates- Rohit Kanungo, Rong Zhao, and Fatima Hamade. Many thanks go to the undergraduate students- Chirstopher Scheinert, Joseph Harris, and Matthew Newton who helped me in the laboratory. Last but not least, many thanks go to my wife Nawrin Sultana and my parents for their continued support.

Table of Contents

List of Tables

List of Figures

Chapter 1

1 Introduction

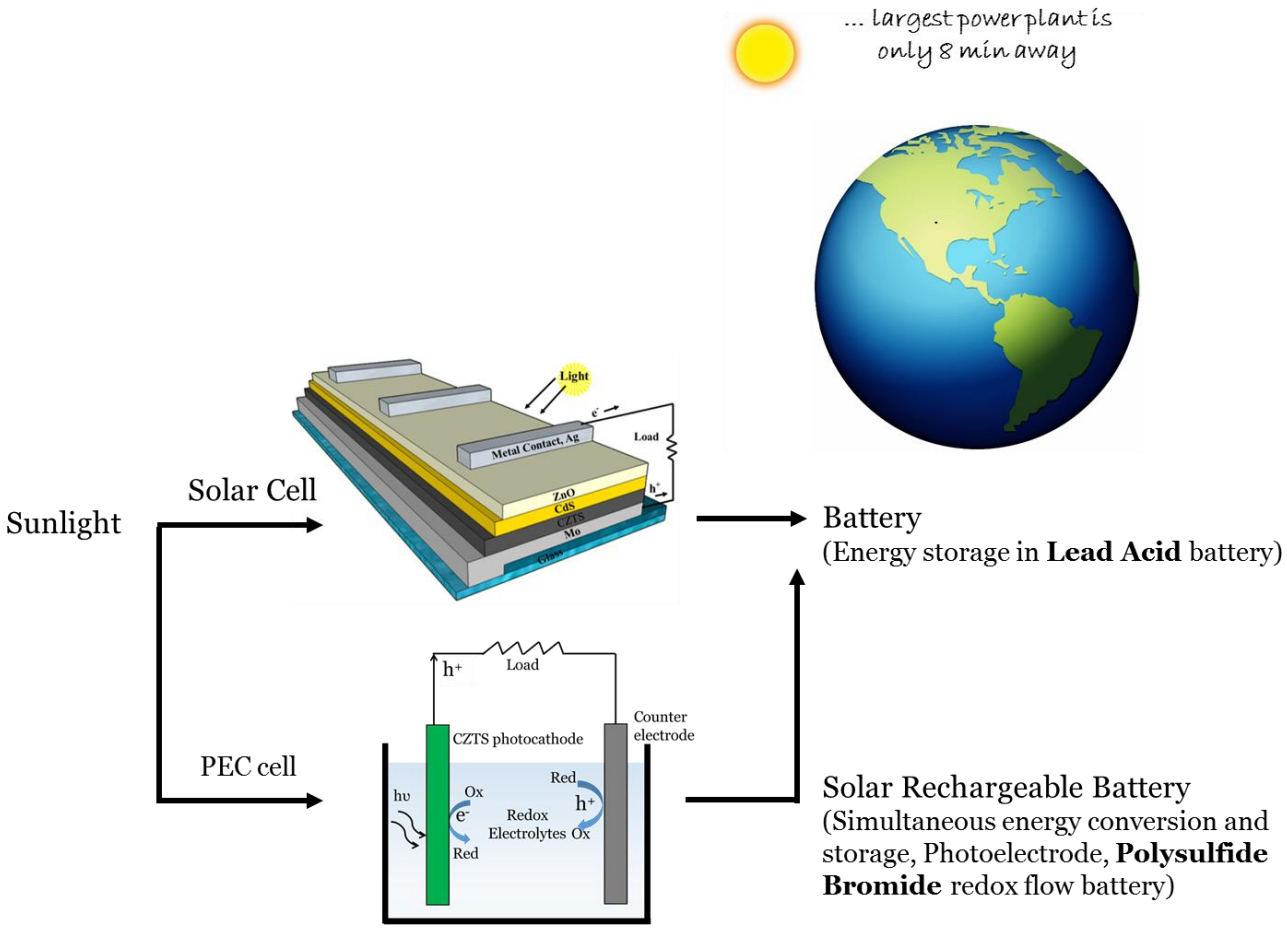

1.1 Green technology for power generation

Global energy consumption is largely dominated by nonrenewable energy sources. Burning fossil fuels releases greenhouse gasses, which trap reflecting heat from the earth and give rise to global warming. Global warming in turn is causing sea level rise and poses a serious threat to the human kind. Eventually, fossil fuels will be depleted at such a rate that economic production of new petroleum will become too expensive to drive the economic output and consumption. Researchers have focused on capturing abundant solar radiation and turning it into useful work since the sun provides nearly 120,000 TW of power to the earth's surface daily.[1] The most direct and benign technology utilizes semiconductor to capture the solar radiation and generate electrical current in a photovoltaic and/or photoelectrochemical cell.

1.2 Physics of semiconductors as a solar absorbing material

The electronic structure of semiconductors, as explained[2] by the molecular orbital theory, allow us to fabricate device for converting of light into electrical energy. These semiconductors are characterized by two separated energy bands. Figure 1-1A shows a simplified energy band configuration of semiconductors. The valence band (VB) are completely filled with valence electrons while the conduction band (CB) remains empty in absence of excitation. The separation energy of the two energy bands is called band gap energy (E_g) which sets prerequisites for light absorption. Since the energy remains conserved (the 1st law of thermodynamics) in a photon-electron interaction, the energy of the photon must be equal to or greater than the band gap energy. The interaction with photons, excite the electrons (e^-) to the CB. The absence of electrons leaves an unbalanced electronic state in the VB which behaves as a positively charged particle or holes (h^+). The excited electrons quickly (~picoseconds)[3] relax back to the conduction band edge by

thermalization and the light energy greater than E_g is lost as heat.[4] The electron in the CB and hole in the VB gain lateral mobility and are called free charge carriers. These charge carriers must be separated and flown through an external circuit to generate electricity before they recombine.

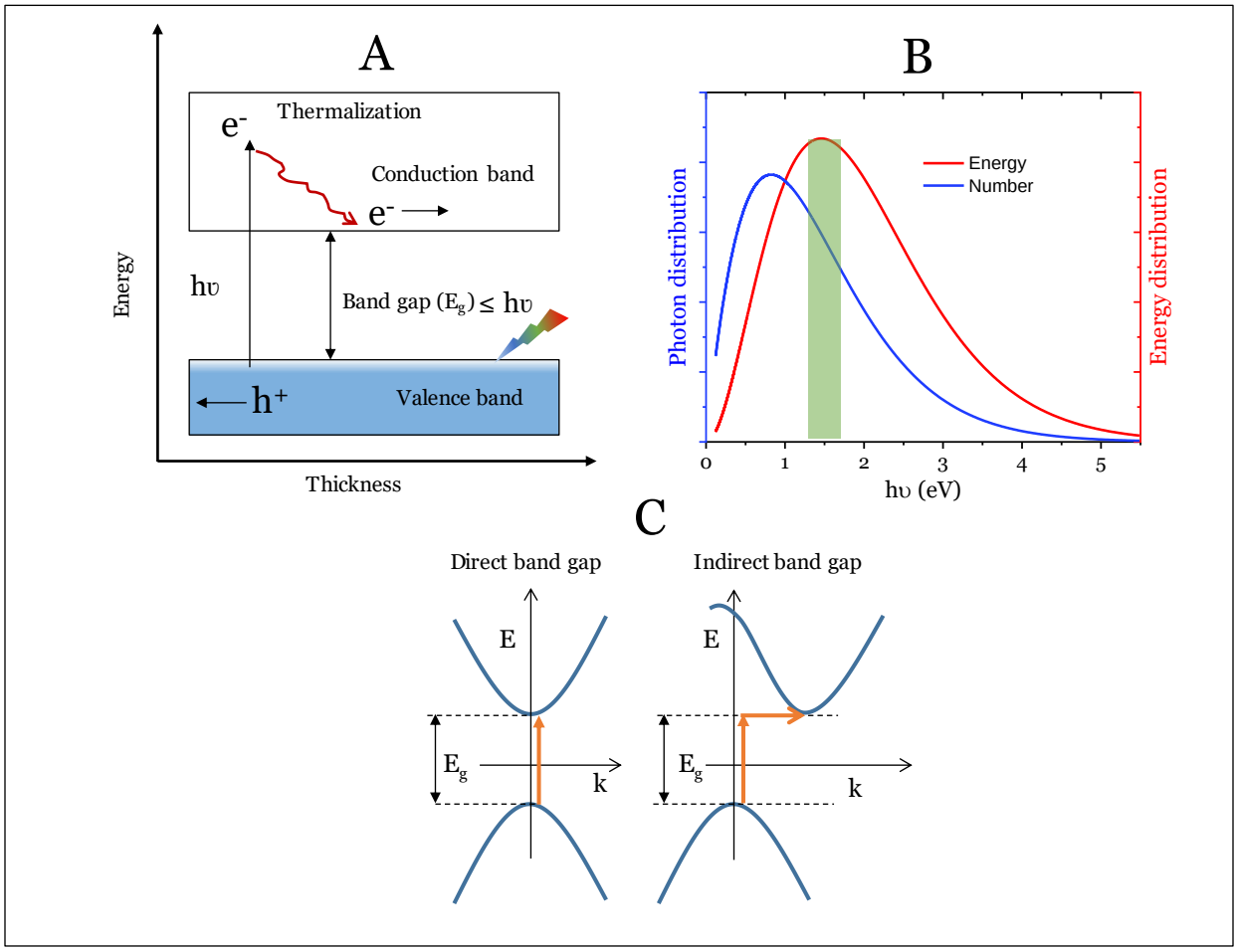

Figure 1-1: (A) simplified energy band configuration in a semiconductor. (B) Solar irradiance plot obtained from Planck's equation at 6000 K. (C) Energy vs. momentum plot showing the direct vs indirect nature of the band gap.

The optimum band gap energy of semiconductors, which maximizes energy efficiency by minimizing energy loss, depends on the solar energy distribution on the earth's surface. Solar irradiance closely resembles black body radiation at 6000 k.[4] Figure 1-1B illustrates photon number and energy distribution in the solar radiation. A semiconductor with band gap of ~1 eV

will absorb the maximum number of photons. However, the energy greater than 1eV will be wasted by the thermalization process. From optimization calculations, the optimum band gap is considered to be within 1.4 to 1.8 eV.[5] The nature of the band gap determines the probability of light absorption and the required film thickness for light absorption. Figure 1-1C shows the relationship between energy and momentum for charge carriers in a lattice. For an indirect band gap semiconductor, the excitation requires interactions between electrons, photons, and phonons which dramatically reduces the probability of absorption for a given thickness of the film.[4] The band gap energy, nature of band gap, material availability, economy, and environmental impacts drive the research focus and selection of solar absorbing material.

1.3 Evolution of solar absorbing materials: from Silicon to CZTS (Cu_2ZnSnS_4)

The photovoltaic effect has been known for nearly two centuries while the popular semiconductor- silicon (Si) was first discovered to show the effect in 1954.[6,7] Numerous revolutionary developments made Si based solar cells very efficient. Today, the efficiency of the single junction solar cells have reached 24.7% where the theoretical limit (Shockley-Queisser) is ~30%.[6,8] Though the efficiency has nearly reached the limit, the search for new materials continues as the manufacturing cost of Si based solar cell remains high. Silicon is abundant on earth but purification and processing still present significant cost hurdles. The cost of 250–300 μm-thick wafers is a major contribution to the high manufacturing cost of Si solar cells.[6] Such a thick wafer is required as Si has an indirect band gap and as a consequent the absorption coefficient is low.[4] For optimum absorption of sunlight, only a few micrometer thin film is sufficient when the semiconductor has a direct band gap energy. Thus, thin film technology emerges with new absorbing materials like CIGS, CIS or CdTe which are compounds of Cu, In, Ga, Se, Cd and Te.

The CIGS and CdTe thin film solar cell were made with record power conversion efficiency (PCE) of 20.3% and 16%, respectively.[9,10] However, In and Te prices grew higher as these elements were competitively used in other technologies and the elements are very rare on earth. Also, Cd is very poisonous and harmful for the environment. This led to a scientific push toward discovery of new materials for photovoltaic applications. CZTS (Cu_2ZnSnS_4) thin film solar cell emerged, which is composed of Cu, Zn, Sn and S. Figure 1-2 shows the content in the earth and pricing of some the common elements used in thin film solar cell.[11] The elements in CZTS are inexpensive, earth abundant and non-toxic.[4]

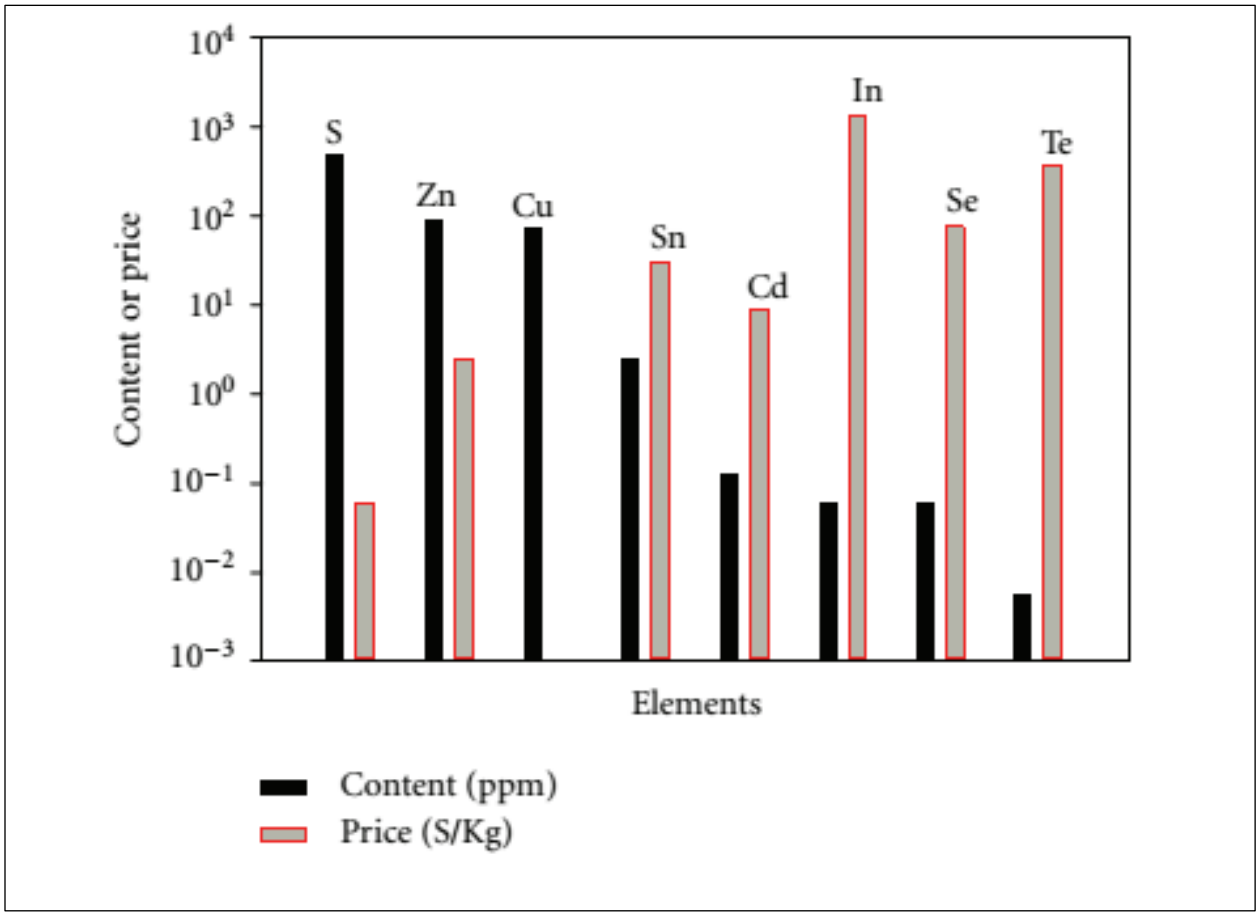

Figure 1-2: The content in earth and pricing of some the common elements used in thin film solar cell

1.4 CZTS (Cu_2ZnSnS_4) crystal structures, properties and challenges

CZTS has been reported to exhibit tetragonal (kesterite or stannite) and hexagonal crystal structure (wurtzite).[12–16] The first principle calculation predicts the tetragonal kesterite phase is thermodynamically the most favorable structure for CZTS. This is consistent with the majority of experimental work reported with kesterite CZTS.[4,16] The kesterite CZTS structure is highly similar to chalcopyrite CIGS [$Cu(In,Ga)Se_2$] where anions and cations are bonded in a tetrahedral environment similar to ZnO or ZnS.[17] The difference between kesterite and stannite structures are shown in Figure 1-3 where the order of cation ions layer are different.[16] In kesterite CZTS, cation layer order follows CuSn CuZn CuSn CuZn CuSn while in stannite layers the order follows ZnSn CuCu ZnSn CuCu ZnSn.

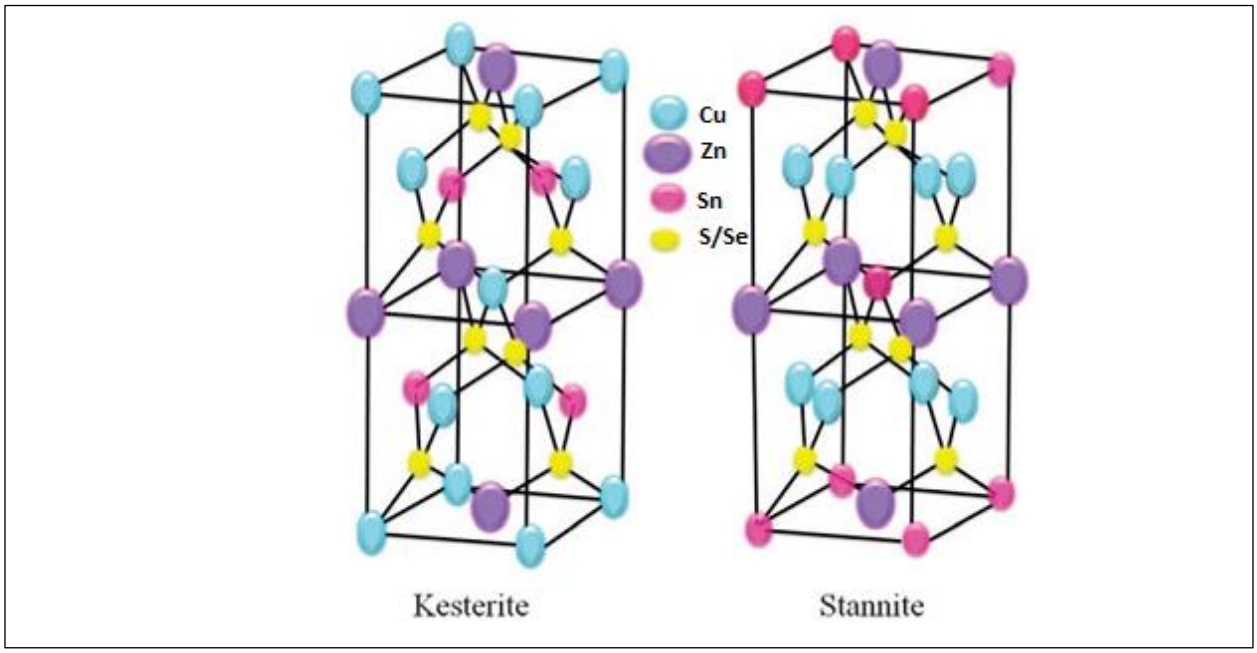

Figure 1-3: Showing crystal structure of kesterite vs stannite phases of CZTS. The tetragonal lattice constant: 0.5435 nm, 1.0843 nm and 1.0843 nm.

The theoretical band gap energy of stoichiometric CZTS (~1.5 eV) falls within the optimum range of 1.4 to 1.8 eV.[4,5,11] The band gap corresponds to an absorption onset of ~825 nm, which encompasses nearly all of ultraviolet and visible solar radiation. The direct nature of band gap offers impressively high absorption coefficient (~10^4 cm^{-1}) which enables nearly complete absorption of solar radiation within a few micrometers thin film.[4] CZTS shows p-type conductivity where the majority charge carriers are positively charged holes (h^+). The p-type conductivity generates due to the presence of the intrinsic defect in crystal lattice.[11] In Cu rich/Zn poor film, the p-type conductivity results from the presence of Cu_{Zn} antisite where Cu takes the Zn site. However, the Cu_{Zn} antisite creates deep acceptor states into which traps charge carriers and induces electron-hole recombination.[12,18] As a consequence, Cu rich/Zn poor film of CZTS lowers the overall efficiency of the device.[11] In Cu deficient film, copper vacancies V_{Cu} and some self-compensated defect pairs such as [V_{Cu} + Zn_{Cu}], [Cu_{Zn} + Zn_{Cu}], are easily formed. These electrically neutral defect sites can reduce the recombination in photovoltaic devices by passivating the deep energy levels within the band gap region. Thus, Cu poor/ Zn rich films are widely preferred for higher performance.[4]

According to first principle calculations, the chemical potential for forming stoichiometric CZTS exists only within a narrow window.[12] As a result, achieving the stoichiometry is very challenging in a quaternary compound like CZTS. The volatile nature of some of the elements such as Zn, Sn and S makes it even more difficult. In Figure 1-4, the phase equilibrium diagram illustrates that the single-phase CZTS is pushed nearly to a point.[19] The binary and ternary impurity phases such as Cu_xS, SnS_x, ZnS, and Cu_2SnS_3 are highly favored outside of this window. These impure phases compete with CZTS growth and the grain boundaries induces trap states for charge

carriers through dangling bonds.[4] Many research groups have linked the poor performance of CZTS to these parasitic phases.[18]

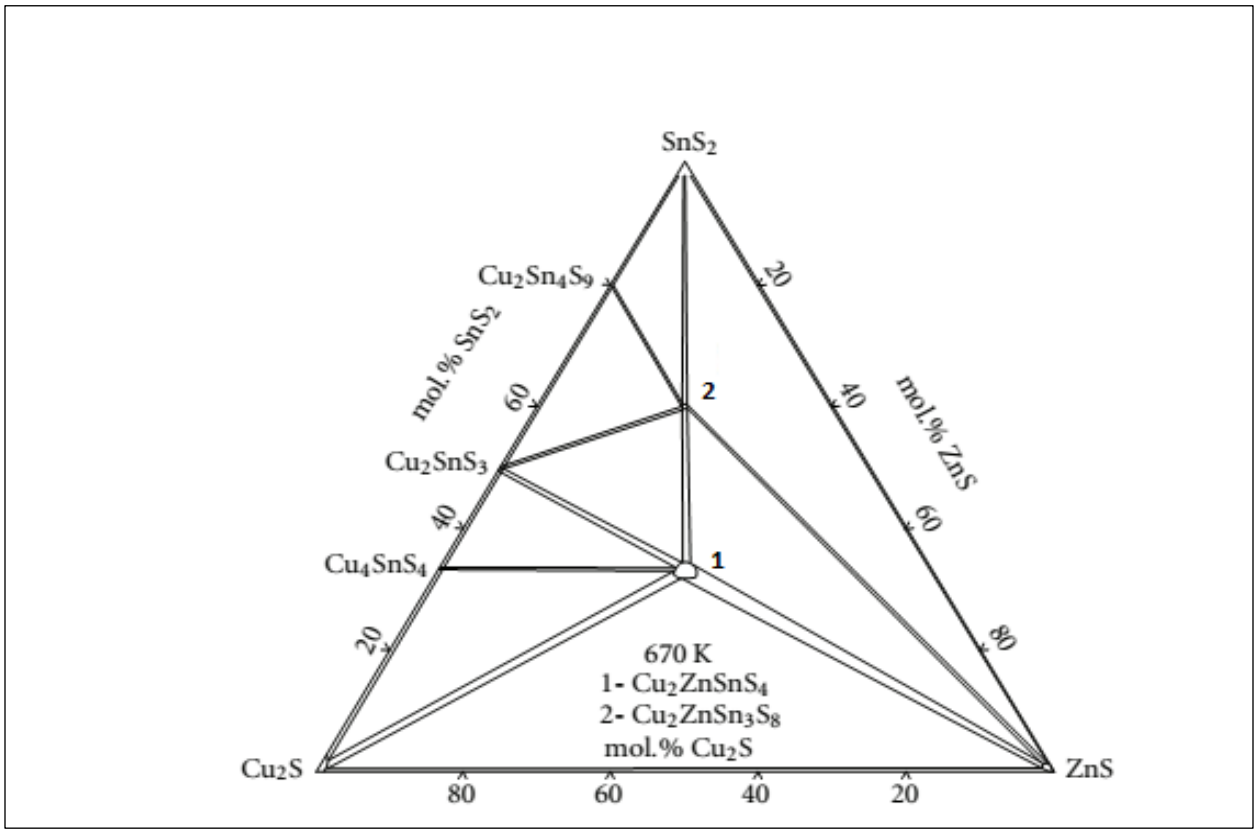

Figure 1-4: Showing phase equilibrium diagram of SnS_2-Cu_2S-ZnS

1.5 CZTS deposition techniques

The CZTS deposition techniques can be classified into two main categories- vacuum & non-vacuum techniques. The vacuum deposition techniques have the advantage of having good control on film thickness and composition and an excellent reproducibility. The techniques include film deposition by evaporation and sputtering in a vacuum chamber.

Plasma sputtering is a robust deposition techniques which can be applied to a wide variety of materials. The very first attempt on CZTS thin film solar cell was made through sputtering

techniques in 1988.[20] Several plasma techniques such as DC sputtering, magnetron sputtering, RF, hybrid (combination of sputtering and evaporation), and ion beam sputtering have been employed for the deposition of CZTS.[21] Katagiri et al. reported the maximum photo conversion efficiency (PCE; 6.77%) on sputtered CZTS solar cell in 2008.[22] Several evaporative approaches such as electrical resistance heating, electron beam evaporation, pulsed laser deposition, co-deposition have been exploited in the preparation of CZTS thin films. Friedlmeier et al. reported the first attempt to synthesize CZTS thin films by thermal evaporation in 1997.[23] The elements were deposited onto a substrate in high vacuum from binary chalcogenide compounds. The film composition and grain size were largely dependent on the substrate temperature., The highest efficiency for evaporated CZTS solar cell was 8.4%.[24]

The vacuum deposition techniques are expensive. Achieving high vacuum imposes significant operating costs in the production. Researchers have shifted their focus toward non-vacuum deposition techniques such as, chemical bath deposition, electrochemical deposition, spin coating, dip coating, and spray pyrolysis. Asokan et al.[25] reported a very respectable CZTS thin film solar cell using simple chemical bath deposition (CBD) techniques (PCE 1.34%). The precursor solution was prepared using $Cu(NO_3)_2$, $Zn(NO_3)_2$, $SnCl_2$, and thiourea in methanol. Monoethanol amine (MEA) was added to the solution as a chelating agent to prevent precipitation. The solution was stirred at room temperature for 1 hour until the solution became clear. After that, a glass substrate coated with indium doped tin oxide (ITO) was inserted into the solution. The temperature of solution was kept at slightly higher temperature to increase the deposition rate. The deposition stopped when precipitation caused agglomeration of particles. The possible mechanism was explained as the dissociation of MEA-complexes and the subsequent reaction between Cu^{2+}, Zn^{2+}, Sn^{2+}, and S^{2-} to produce Cu_2ZnSnS_4. The root-mean-square roughness of the film was

reported as 3.2 nm. The as prepared thin film was annealed in air at 623 ^{o}K for 1 hour. The final configuration of the cell was: Al/CdS/CZTS/ITO-Glass. Electrochemical deposition is another cost-effective deposition route for CZTS. Ennaoui et al. reported the most efficient (~3.4%) solar cell prepared using this method.[26] CZTS was electrodeposited on 10×10 cm^2 Mo coated SLG using conventional three-electrode assembly. The electrochemical cell contained Ag/AgCl as reference, an inert anode, Mo (0.5 μm) on glass (3 mm) as working electrode, and metal salts of Cu(II), Zn(II), Sn(IV) ions together with complexing agents and additives as the electrolyte solution. On average an area density of 500 μg/cm^2 was achieved within 20 min depending on temperature, bath flow, and pH value. The film containing all metals was then subject to high temperature sulfurization to form the kesterite CZTS phase. The champion PCE of CZTS (12.6%) was reported from a hydrazine-based precursor solution where the precursor solution having Cu-poor and Zn-rich stoichiometry was spin-coated onto Mo-coated glass and annealed at 500 °C in Se atmosphere.[27] Resulting CZTSSe (about 5 μm) film was followed by 25 nm CdS (chemical bath deposition) and 10 nm ZnO (sputtered)/50 nm ITO. Higher ratio of the Zn was maintained in the precursor solution, as some the film loses Zn by evaporation during annealing at high temperature. Also, higher Zn/Cu ratio was reported to reduce the probability of excess Cu, which forms undesired binary phase (Cu_2S).

The precursor solution techniques provide excellent cost benefit and flexibility in the deposition process. However, the techniques have some drawbacks as well. For example, in spin coated techniques material efficiency is very low, almost 99% of the material is wasted. The technique requires heat treatment between each steps of coatings which complicates the fabrication process. Spray pyrolysis is a convenient technique for instantaneous film deposition. In this method, a precursor solution containing sources of the elements such Cu, Zn, Sn, and S is sprayed

onto a heated substrate. The as sprayed film is then annealed at high temperature under SnS and S condition to achieve CZTS. Depending on the substrate, pH value, and composition of the solution, the film crystallinity and the morphology varies.[11]

While optimal cost metrics are favorable when solution-processing technologies are employed, CZTS thin film prepared from precursor solution suffers from a drastic increase in impurity phases without a thermal annealing step. The energy intensive processing step can be avoided by synthesizing CZTS nanocrystal (NC) prior to film deposition. In fact, CZTS nanocrystal offers several advantages over bulk deposited film.[28] Firstly, the band gap energy of the NC semiconductor largely depends on the particle size. This facilitates tuning of physicochemical characteristics through quantum confinement effects by altering the physical dimensions of the NCs, which can be used to maximize the driving force for carrier transfer to an acceptor species. Secondly, NC may undergo multi-excitation, which means the NC will generate multiple electron-hole pairs from single photon absorption when photon energy is greater than $2E_g$.[29] This phenomenon offers an opportunity to overcome the theoretical SQ limit (30%). Researchers have postulated that NC based solar cells can reach nearly 50% efficiency.[29] The NC can be attached to form a thin film by direct adsorption (physisorption) or with the help of a linker. In a physisorbed film NC-NC interaction hampers the efficiency which can be overcome with linker assisted attachment. However, until 2010, the maximum PCE for CZTS NC was only 2%.[30–32] Such a poor performance was attributed to the poor attachment of NC on the surface and the poor electron transfer ability of linker.[33] A champion nanocrystalline film was reported by Guo et al., 2010.[34] In this solar cell, CZTS nanocrystal (NC) prepared using hot injection method was dispersed in hexane thiol which was directly applied onto molybdenum (~1 μm) coated soda lime glass substrates by knife coating to form a densely packed nanocrystal. Two separate coatings with

intermediate heat treatment (air dry, 300 °C, 1 min) resulted in a total film thickness of approximately 1 µm. The resulting CZTS film was composed of large densely packed grains. The final configuration of the cell was: Ni-Al (Top contact, thermal evaporation)/ITO (RF sputtering, 200 nm) /ZnO (RF sputtering, 50 nm)/CdS (50 nm, CBD) /CZTS/Mo. The cell had a total area of 0.47 cm^2 with PCE of 7%.

1.6 CZTS devices: photovoltaic cell vs photoelectrochemical cell

Traditional CZTS based devices are focused on solid-solid junctions (photovoltaic cell) of different layers of semiconductors sandwiched together. Figure 1-5A shows a typical configuration of CZTS based photovoltaic cell: Ag/ZnO/CdS/CZTS/Mo. The device utilizes the relative position of valence and conduction bands of different layers for separating the photogenerated charge carriers, as shown in Figure 1-5B.[34] The solar radiation is absorbed in the active layers of CZTS and CdS. The photogenerated free electrons (e^-) flow downward to reduce its free energy while holes (h^+) move upward. Eventually, the electrons and holes are separated to the opposite metal conducting end. The charge carriers flow through external load to generate electricity.

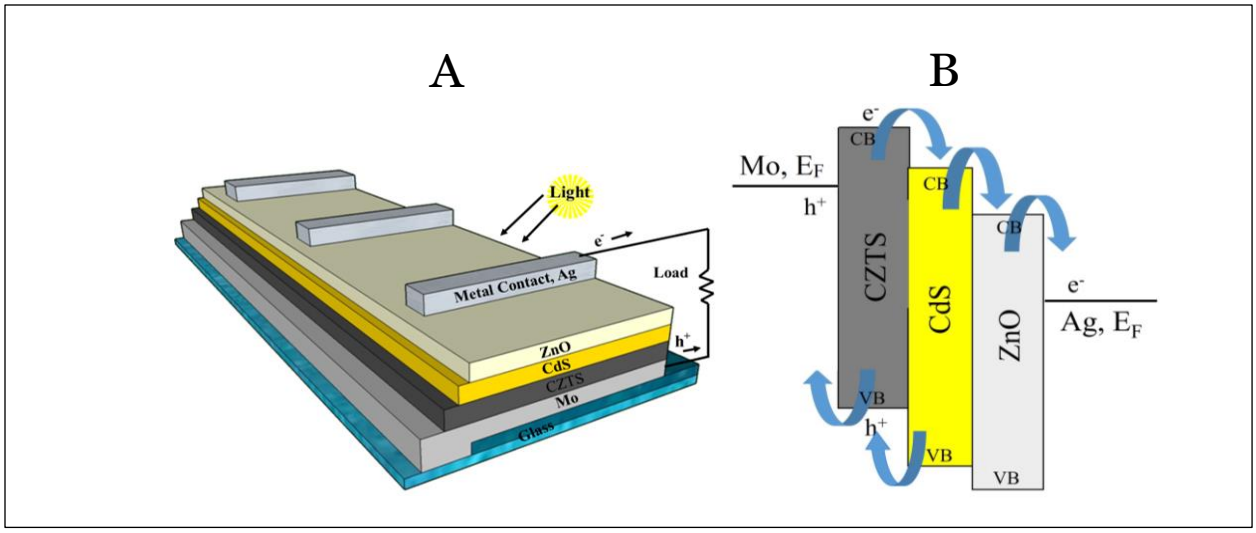

Figure 1-5: (A) The configuration of the photovoltaic cell. (B) The energy band diagram.

Many of the processing steps of the traditional solid-solid junctions can be simplified or eliminated using a solid-liquid junction in a photoelectrochemical cell (PEC) where energy conversion is achieved by immersing a semiconducting photoelectrode in suitable redox couples as shown in Figure 1-6A.[35] The solar radiation is absorbed by the CZTS electrode which generate photoexcited electron-hole pair. The electrons are transferred into the electrolyte solution while holes leave the photocathode and reach the counter electrode through external circuit. At the counter electrode, holes oxidize back the electrolyte into to the original states. The electrolytes remain unchanged. The end result is that the photon energy is converted into electrical energy. Figure 1-6B demonstrates the charge separation mechanism. Upon immersion, the electrochemical potentials of electrode (also called fermi level[36] (E_F) which is the energy level at which the probability of finding the electron is 50%) and electrolyte solution (redox potential) equilibrates through charge exchange. Since the charge density in the solid is much lower than liquid, the equilibration creates a depletion layer near the solid-liquid interface. The charge depletion results in bending the energy bands which poses a barrier (Schottky barrier) to charge transfer across the

interface. The photo-electrochemical cell (PEC) utilizes the Schottky barrier and/or diffusion mechanism for separating the photogenerated charge carriers. Any electron/hole pair generated (or travelled by diffusion) in this region is separated instantaneously which contributes to the photocurrent. A downward bending encourages e^- injection to the electrolyte while upward bending acts against e^- injection.[37] The direction of band bending or the height of barrier depends on the pre-equilibrium fermi levels of electrode and redox couples.[35,38]

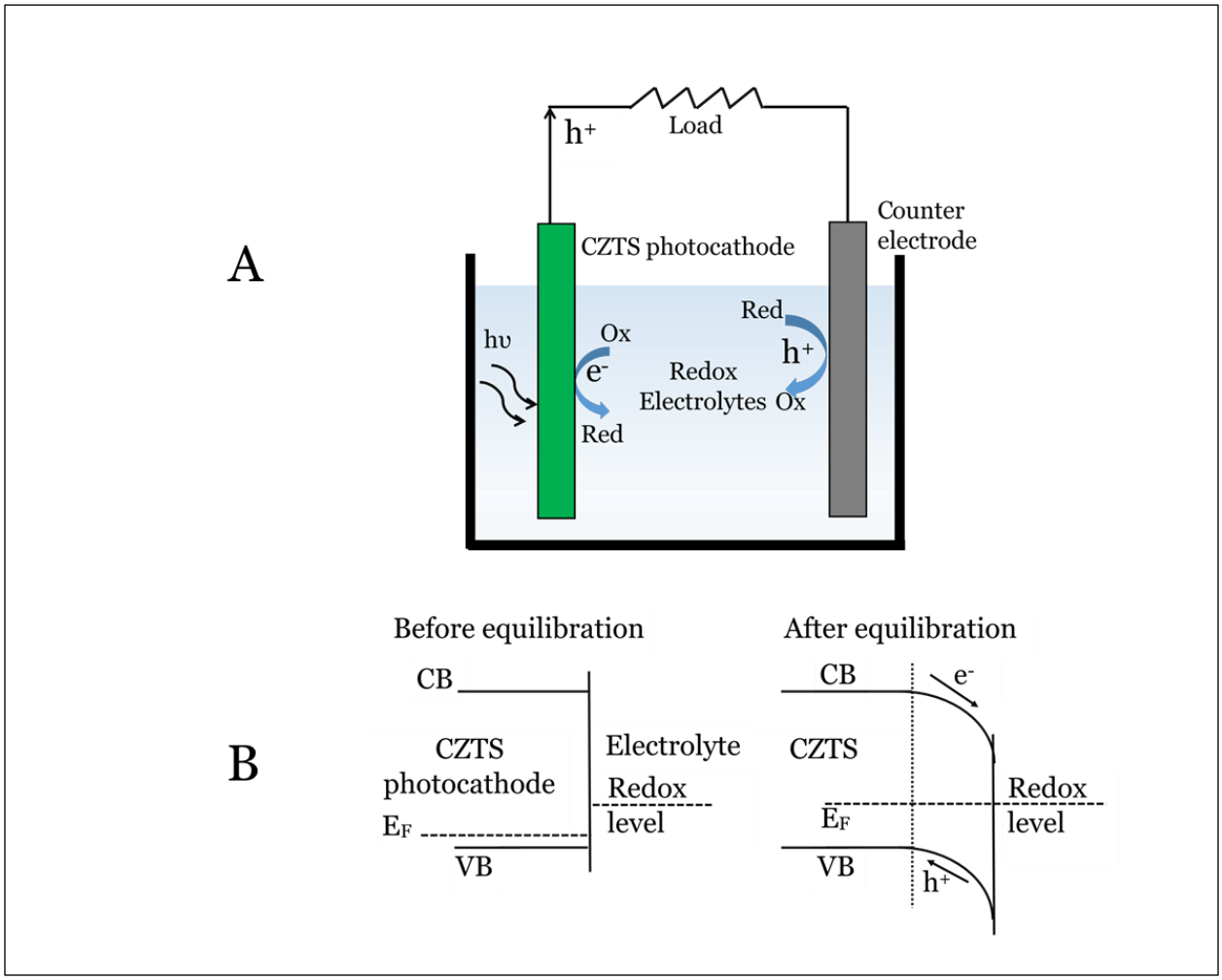

Figure 1-6: (A) CZTS semiconductor-liquid junction photovoltaic cell. (B) Charge separation mechanism

The comparative advantages of solid-liquid junction over solid-solid junction are as follows. The doping step of traditional p-n junctions is not needed in solid-liquid junctions since the charge separation is achieved by the Schottky barrier.[38] In the electrochemical cell, the electrolyte redox potential (determined by the Nernst equation) can be used to tune the amount of band bending and half of the solid-solid junction is replaced by inexpensive redox solution and counter electrode. This simplification leads to the reduced cost in materials synthesis and device fabrications. The procedures for adding redox solution, counter electrode, insulation of the electrodes and air tight seal for the completed cell are well established in battery technology.[35] In liquid-junction cells, random crystal orientation can be used as the liquid will form spontaneous contact with electrode upon immersion. This spontaneous contact offers opportunity to exploit special architecture to improve charge extraction efficiency.[39]

Despite numerous advantages, the CZTS thin films have been rarely explored in a photoelectrochemical cell configuration. Dai et al. applied porous CZTS photocathode in a dye sensitized solar cell (DSSC) to improve the short circuit current and power conversion efficiency.[39] Additionally, the adoption of a photocathode in a rechargeable battery provides an opportunity of combining solar energy conversion and storage in a single and simultaneous step. Such intensification of the processes often leads to cost reduction.[40] Researchers have attempted combining semiconductor photoanode into various rechargeable battery systems.[40–45] Recently, redox flow batteries (RFB) have captured a great attention which is demonstrated by the exponential number of publications in the field.[40] RFBs have many advantages such as low-temperature operations, large cycle-life, design flexibility, scalability, simplicity, low maintenance costs, and reversible redox reactions.[40–45] However, to achieve the target cost of $150 per kWh set by the DOE Office of Electricity Delivery and Energy Reliability, the chemicals are needed to be

almost free.[46] The polysulfide based RFB system could be an excellent candidate because sulfur which is an industrial waste from crude oil production.[47]

1.7 Motivation and objectives

The abundant solar energy is considered as the most viable solution to the energy crisis and global warming. The semiconductor materials used to capture the solar radiation must possess the optimum thermodynamic and economic quality. The copper, zinc, tin, and sulfur-based semiconductor, CZTS holds a great attention in the research community. The p-type semiconductor consists of inexpensive, nontoxic, and earth abundant elements, has a very high absorption coefficient and optimum energy band gap. However, the preparation of phase pure CZTS is quite challenging. The quaternary compound often coexists with other binary and ternary impure phases. In the past two decades, the research in CZTS have been proved very fruitful. However, lots of attention is needed to improve the power conversion efficiency to meet the grid parity. The lacking in performance is often linked to the formation of impure phases and intrinsic defects in CZTS. Many different deposition techniques have been exploited to fabricate high quality CZTS thin film. The early research techniques involved expensive vacuum techniques. To facilitate large scale, cost effective production, recent studies are focused on solution processing of CZTS. The CZTS thin film can be applied in solid state photovoltaic devices. However, the solid-liquid junction in a photoelectrochemical cell offers easy fabrication and significant cost reduction compared to the solid-state devices. Also, incorporating a photocathode in a battery can be used for simultaneous solar energy conversion and storage in a process intensified environment. The studies presented here represent a bottom up approach for developing high quality

photocathode of CZTS for potential application in solar energy conversion (nanocrystal sensitized solar cell) and/or energy storage technology (solar rechargeable battery).

Chapter 2

2 Stable and Flexible Precursor Solution for Reproducible Spray Deposited Cu_2ZnSnS_4 Photoelectrodes

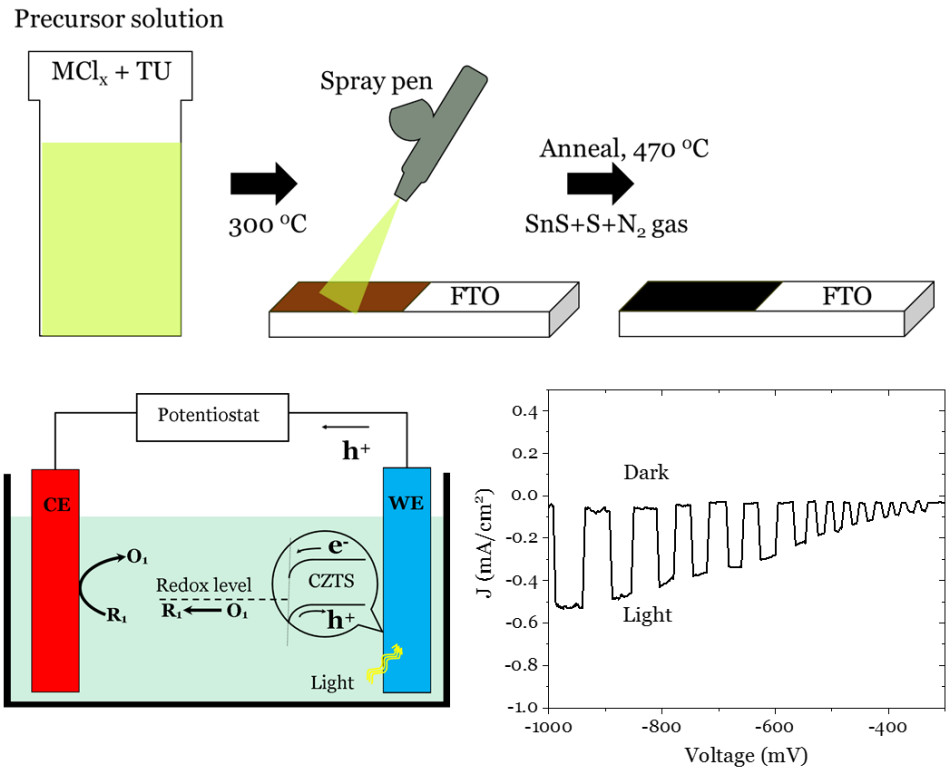

2.1 Introduction

The sun provides 120,000 TW of radiant power to Earth's surface.[1] Capturing and converting solar energy is the most attractive option to meet the increasing energy demand in a sustainable fashion. Several variables must be optimized to facilitate a smooth transition from fossil fuels to solar energy, primarily cost, longevity, and efficiency. Recently, semiconducting thin films of Cu_2ZnSnS_4 (CZTS) have captured the attention of researchers since the material exhibits many related desirable properties. CZTS contains Earth abundant elements, low toxicity, moderate cost of Cu, Zn, Sn, and S, and optimal band gap (~1.5 eV), which drives much of its current study.[35,48,49] CZTS exhibits strong photon absorption properties with an absorption coefficient on the order of $\sim 10^4$ cm^{-1}. This high absorptivity enables a marginal film thickness of 1 μm to absorb ~95% energy of the incoming sunlight.[50] However, quaternary semiconductors, such as CZTS, present significant challenges in obtaining phase purity as a result of the strict thermodynamic conditions for their stability. Impurity phases are often binary or ternary chalcogenides, which are thermodynamically favored except within a small window of CZTS phase.[51] Optimal cost metrics are obtained using solution-phase processing technologies, yet CZTS thin films fabricated in this fashion suffer from a higher than average density of impurity phases, particularly without a thermal annealing step.

Synthesizing CZTS thin films directly from precursor solutions has been attractive because of low cost, scalability, and exquisite potential to exert control over film thickness and quality.[52,53] Solution-based fabrication of CZTS thin films is often carried out by spin coating a precursor solution, in some cases multiple times, under proper shear and drying rates to yield the desired film thickness and quality. The highest efficiency reported from CZTS thin film employed spin coated Hydrazine based precursor solution.[27] Although spin techniques are facile, the film can

sometimes require heat treatment between coatings and other additional processing steps, which complicates the thin film fabrication. The high toxicity and hazard levels associated with hydrazine have driven researchers to focus on developing nonhazardous solvents such as mixtures of alcohol and/or water.[54–57] Some have precipitated binary particles by mixing precursors with sulfide in water solvent, spray-deposited the resulting precipitates onto a conductive substrate, and annealed it to produce high-quality CZTS thin film photoelectrodes.[58]

One major issue encountered in fabricating CZTS thin films from soluble precursor solutions is the lack of stability and flexibility of the solution itself. The solution should minimally meet two important criteria: 1) exhibit stability for the time period required for deposition and 2) sufficient flexibility to tune the composition of the resulting film to meet the desired stoichiometry or grain density. The previously reported non-hazardous precursor solution recipes primarily involve halide or oxide salts of Cu^{2+}, Zn^{2+}, Sn^{2+}, and a sulfur source such as thioacetamide (TAA) which also acts like a complexing agent.[59–62] The mechanism of CZTS formation has been explained by the following chemical reactions[60]

Reaction 1 (Solution): $2Cu^{2+} + Sn^{2+} \longrightarrow 2Cu^{+} + Sn^{4+}$

Reaction 2 (Annealing): $2Cu^{+} + Zn^{2+} + Sn^{4+} + 4S^{2-} \rightleftharpoons Cu_2ZnSnS_4 (CZTS)$

Reaction 1 lessens the flexibility of the recipe as the deviation of Cu^{2+} and Sn^{2+} salts from stoichiometry results in unreacted Sn^{2+} in the solution, which encourages SnS binary phase formation. However, nonstoichiometric films with Cu poor and Zn rich composition are now widely accepted to show better performance than those fabricated stoichiometrically.[27,63,64]

Furthermore, TAA is forms only a weak complex with cations that breaks easily, typically within 30 min at room temperature.

Here we report on the development of a flexible and stable precursor solution for solution fabrication of CZTS thin films. The TAA complexing agent was replaced by thiourea (TU) since it forms a stronger complex with the precursor metal ions, which was stable for days at room temperature. The TU (pH~2) reduces Cu^{2+} to Cu^{+} ions[65,66] and accommodates TU-Cu^{+} complex solubility. The UV-Vis absorption profile of a thin film sprayed from a TU-$CuCl_2$ mixture exhibits characteristic absorption features of Cu_2S, which supports previous reports reduction of Cu^{2+} to Cu^{+} through the formation of the TU-Cu^{+} charge-transfer complex.[67,68]

The elimination of Reaction 1 permits the use of Sn^{4+} directly in the precursor solution with Cu^{2+}. This enables one to tune the stoichiometry of the resulting thin film quite easily. We utilized this strategy to vary the composition of CZTS photoelectrodes while monitoring the evolution of impurity phases and their impact on the photosensitivity of the electrodes. Use of Cu^{+} directly was restricted by the poor solubility and tendency for disproportionation in ethanol/methanol solvent. The precursor was spray-deposited in a controlled fashion onto preheated FTO to achieve the desired film thickness, and the films were annealed under different conditions. The thin films were then employed as photocathodes in a photoelectrochemical cell to probe their photosensitivity under AM1.5 simulated sunlight.

2.2 Experimental

2.2.1 Chemicals

The chemicals for preparing CZTS photocathode were used as received from the suppliers. The chemicals purity and vendors are listed below- copper (II) chloride dehydrate (CuCl2.2H2O),

ACS, 99+% (Alfa Aesar); zinc chloride anhydrous (ZnCl2), 99.95% (Alfa Aesar); tin (IV) chloride pentahydrate (SnCl4.5H2O), 98% (Strem Chemicals); thioacetamide, ACS, 99% (Alfa Aesar); thiourea, 99% (Alfa Aesar); methanol, 99.9+% (EMD Millipore Corporation); ethyl alcohol 190 Proof, 95% (Pharmco-Aaper);

2.2.2 Methods

2.2.2.1 Precursor solution preparation

The overall scheme of the photocathode fabrication is shown in Figure 2-1. In a typical synthesis, 1.87 mmol $CuCl_2$, 1.3 mmol $ZnCl_2$, 0.95 mmol $SnCl_4$, and 12 mmol thiourea were dissolved one by one in 20 mL methanol-water mixture (80-20 wt.%). Methanol was found to provide better solubility and stability for the solution compared to ethanol. A white slurry was produced upon addition of thiourea that remained dissolved in excess thiourea. The resulting solution was stable in air for a long period of time although excess thiourea might precipitate after a few days.

2.2.2.2 Photocathode preparation using spray pyrolysis

The transparent precursor solution was sprayed onto a preheated FTO substrate (~300 ^oC) using a spray pen to form the thin film (Figure 2). The sprayed film was then annealed with $SnS_{(g)}$ and $S_{(g)}$ atmosphere at 470 ^oC for 1 hour with a low flow of N_2 gas. The sulfurization at higher temperature (especially close to 500 ^oC) sometimes causes growth of sulfur crystals on the FTO substrate reducing conductivity of the substrate. To avoid this from occurring, the FTO can be wrapped well with aluminum foil to reduce contact with sulfur vapor.

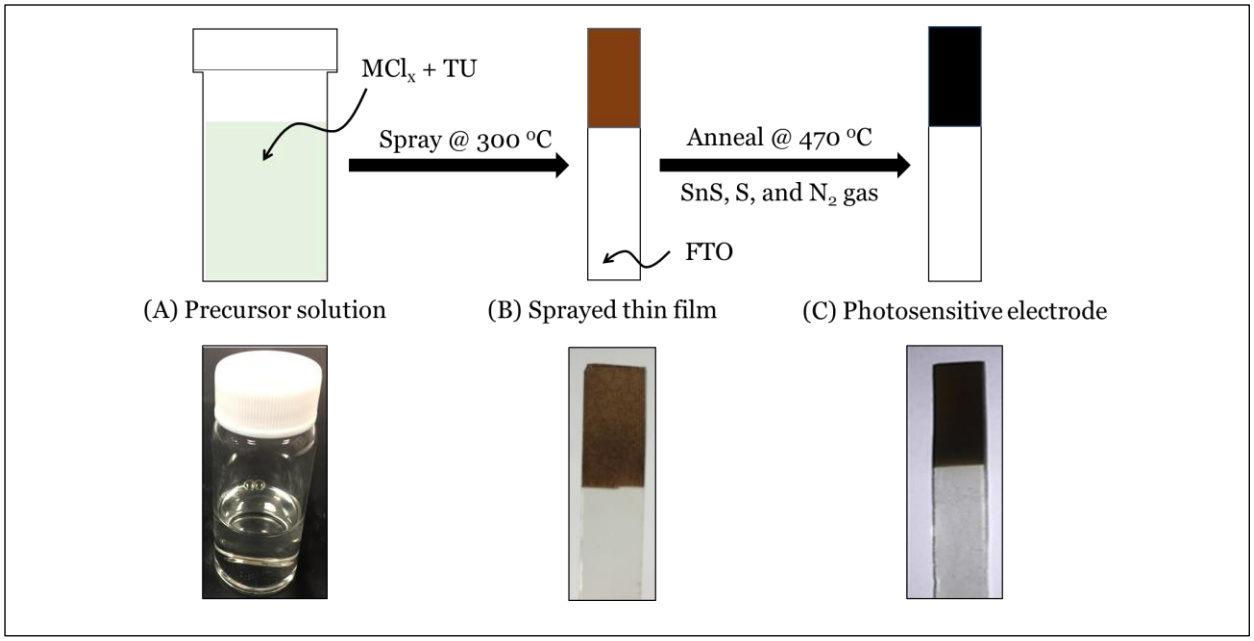

Figure 2-1: (A) Transparent clear solution of metal chlorides and thiourea, (B) Dark brown film from sprayed solution onto preheated (300 °C) FTO substrate, and (C) Dark black film after annealing at 470 °C under SnS, S, and N_2 gas atmosphere.

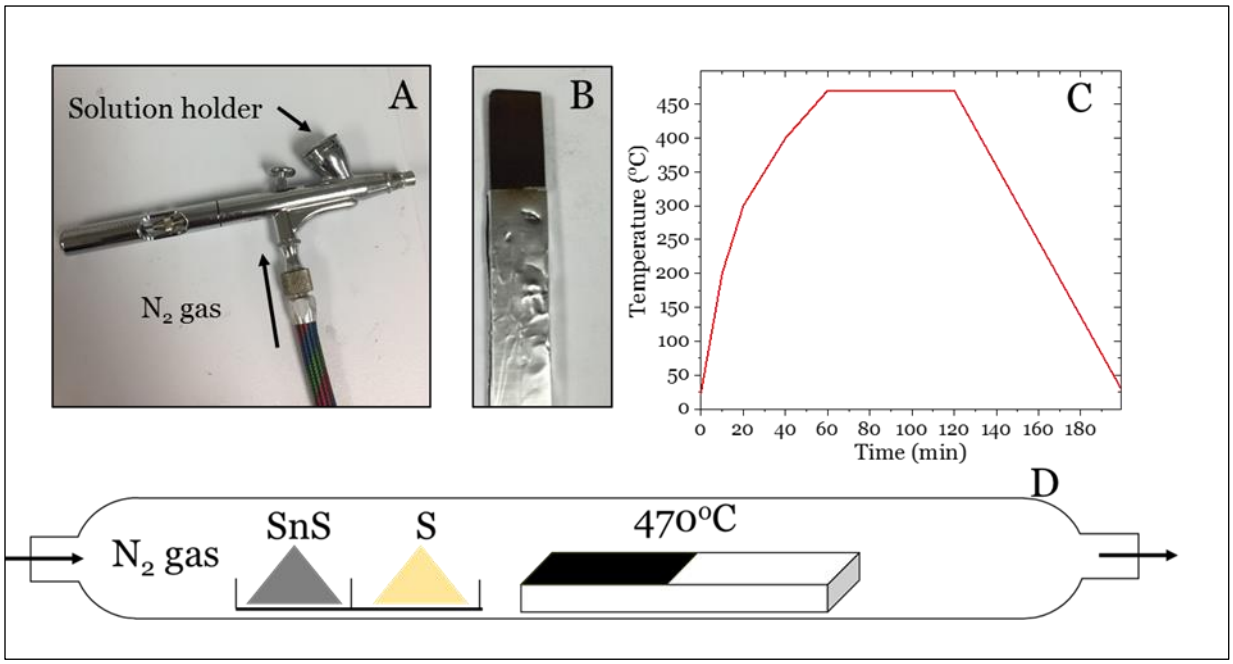

Figure 2-2: (A) Spray pen. (B) Photograph of aluminum wrapped annealed film of CZTS. (C) Temperature profile for film annealing. (D) Furnace tube schematics showing direction of N_2 gas flow, ampules SnS, S powders and the annealed films.

2.3 Results and Discussions

2.3.1 Comparison of traditional vs modified recipe

A comparison between the standard precursor solution and that with our modifications is provided in Figure 2-3. Route 1 shows the traditional precursor recipe which started with $CuCl_2$ and $ZnCl_2$ in ethanol. After addition of $SnCl_2$, a white slurry of CuCl produced which dissolved in excess thioacetamide. The transparent yellow precursor solution started to break down within 40 min of preparation at room temperature. In about 80 min, the solution completely lost the homogeneity required for the deposition process. Route 2 shows a more stable and flexible synthesis recipe where $CuCl_2$ and $ZnCl_2$ were added in methanol-water (80-20%) mixture. In this approach, $SnCl_4$ dissolved in the mixture without reducing Cu^{2+} which was evident from the absence of Cu^{+} precipitates. The Cu^{2+} salt was reduced to Cu^{+} precipitation when thiourea was added to the mixture. The Cu^{+} precipitates dissolved quickly in excess thiourea and the complexes remained dissolved in the solution for several days at room temperature, demonstrating the improved stability.

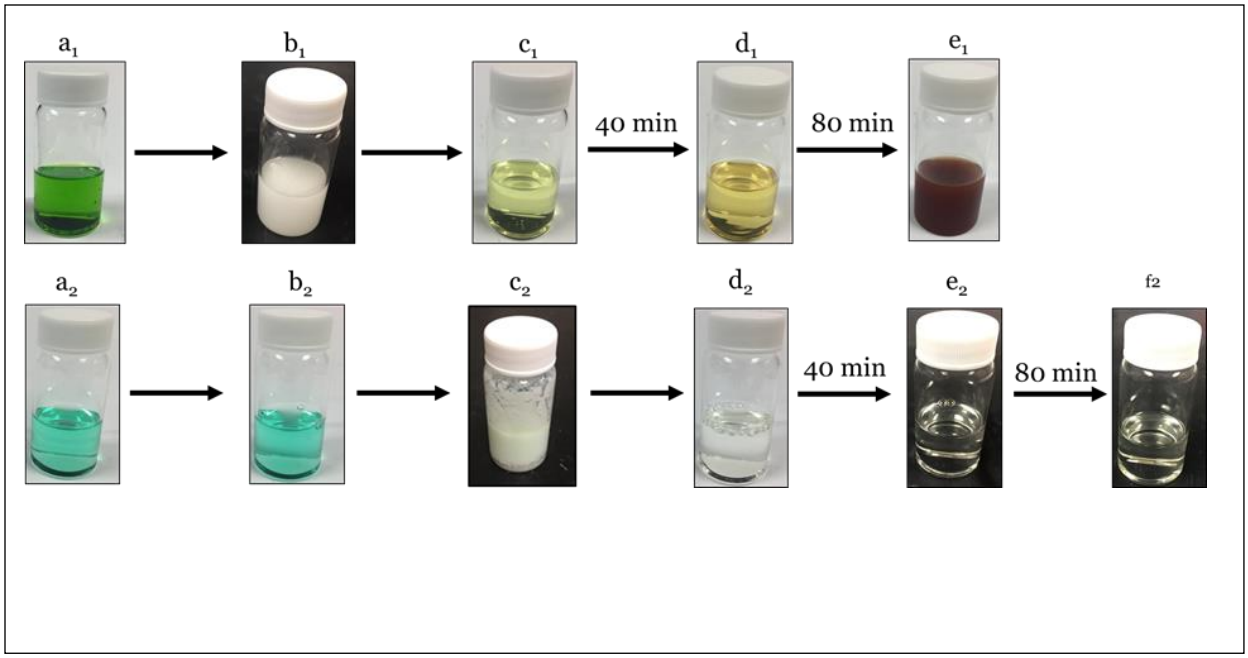

Figure 2-3: (a_1) $CuCl_2$ and $ZnCl_2$ in Ethanol, (b_1) $SnCl_2$ added, (c_1) precursor solution with thioacetamide, (d_1) solution decomposing after 40 minutes, (e_1) inhomogeneous solution after 80 minutes, (a_2) $CuCl_2$ and $ZnCl_2$ in Methanol and water, (b_2) $SnCl_4$ added, (c_2) precursor solution with thiourea, (f_2) homogeneous solution after shaking (e_2) stable solutions after 40 minutes, and (f_2) stable solution after 80 minutes.

2.3.1.1 X-ray diffractogram and raman spectroscopy

The annealed CZTS films prepared from the stable precursor solution were characterized using X-ray diffractogram (XRD) and Raman spectroscopy. In Figure 2-4A, the kesterite structure of CZTS was identified using XRD.[52,69–71]However, XRD does not suffice to identify CZTS because of similar unit cell dimensions of CZTS, ZnS, and CTS (Cu_2SnS_3). To distinguish the impure phases (ZnS and CTS) from CZTS, Raman spectroscopy was performed on the films. The CZTS has been predicted to have 27 Raman active modes among which only 3 modes (related to A_1 symmetry) are most commonly reported for green light excitation (514 nm) - a strong Raman shift at 333-339 cm^{-1} and two weak shifts at 285-292 cm^{-1}, and 371-373 cm^{-1} which can be used as fingerprint for CZTS.[72–75] Until today, 18 modes have been detected using different excitation wavelengths.[76] In Figure 2-4B, we observed and identified 8 Raman active modes using 514 nm

excitation with a wide range of Cu/Zn ratios. The shoulder of the strongest peak at ~337 cm^{-1} was examined very carefully. The absence of the shoulder peaks at 316 cm^{-1} or 352 cm^{-1} eliminated possible formation of ternary CTS or binary ZnS phases, respectively. Additionally, we found that the Raman peaks displayed a red shift with increasing Cu composition. This effect was most obvious for the strongest peak as illustrated in Figure 2-4C. The red shift can be attributed to the higher degree of disorder in the cation sublattice of CZTS. The random distribution of cations on the Cu-Zn plane causes the crystal structure to be altered from a kesterite phase to a stannite like structure.[77,78] The CZTS growth temperatures were probed using Raman spectroscopy as seen in Figure 2-4D. A CZTS characteristics Raman shift appeared at ~329 cm^{-1} at a low temperature (350 ^{o}C). Interestingly, the peak continued developing while blue-shifting with increasing temperature. At 470 ^{o}C, we have identified maximum number of Raman shifts for CZTS with minimal presence of impure phases, which established the minimum annealing temperature for the sprayed film.

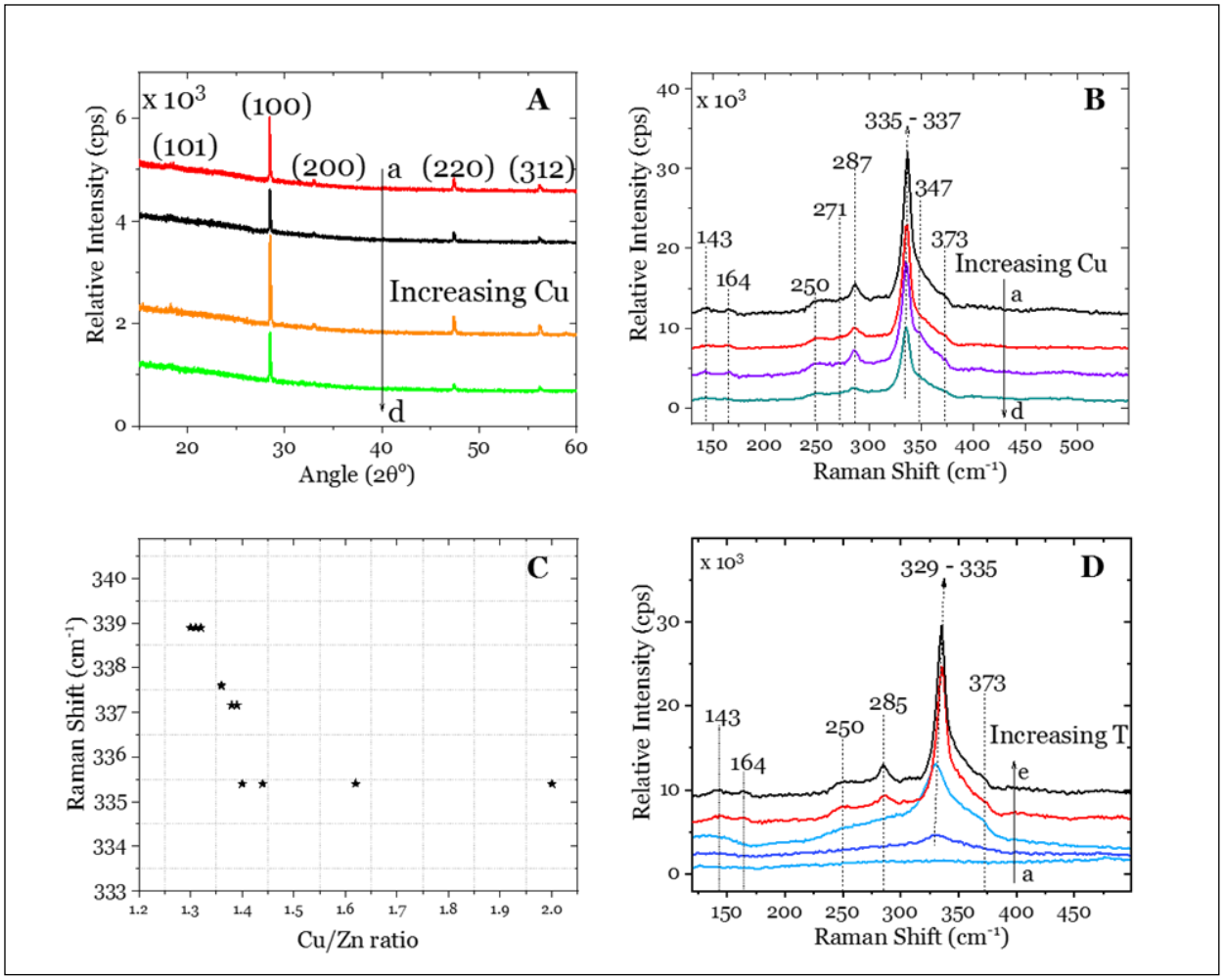

Figure 2-4: (A) X-ray diffractogram (XRD), and (B) Raman spectroscopy of CZTS annealed films where Cu/Zn ratio in precursor varies from (a) 1.36, (b) 1.38, (c) 1.40, (d) 1.44, (C) Raman peak shifting with Cu/Zn ratio in the precursor, and (D) Raman spectroscopy for different annealing temperature (a) 250 °C, (b) 350 °C, (c) 450 °C, (d) 470 °C, (e) 490 °C for CZTS with Cu/Zn ratio 1.44. Raman spectrometer scan settings: 532 nm excitation wavelength, 5% laser power, 10s, 20 accumulations. Si reference peak at 508 cm^{-1}.

2.3.1.2 X-ray photoelectron spectroscopy

The valence states of the elements in the film were investigated using X-ray photoelectron spectroscopy (XPS) as shown in Figure 2-5. Two narrow doublet peaks in the Cu ^2P spectrum appearing at 931.9 eV ($^2P_{3/2}$) and 951.7 eV ($^2P_{1/2}$), separated by 19.8 eV, indicate the existence of Cu (I).[79–81]The Zn ^2P binding energies at 1021.8 eV ($^2P_{3/2}$) and 1044.9 ($^2P_{1/2}$) eV, with a splitting energy of 23.1 eV, correspond to Zn (II) oxidation state. The Sn (IV) state is confirmed by Sn ^3D

peaks at 486.5 ($^3D_{5/2}$) and 494.9 eV ($^3D_{3/2}$) with its characteristic peak separation of 8.4 eV. The S^2P spectrum shows peaks at 161.7 ($^2P_{3/2}$) and 162.8 eV ($^2P_{1/2}$) with a split of 1.1 eV which indicate S(II) oxidation states. As expected, a small presence of O ^1S exists in the film, which was a result from high-temperature annealing.

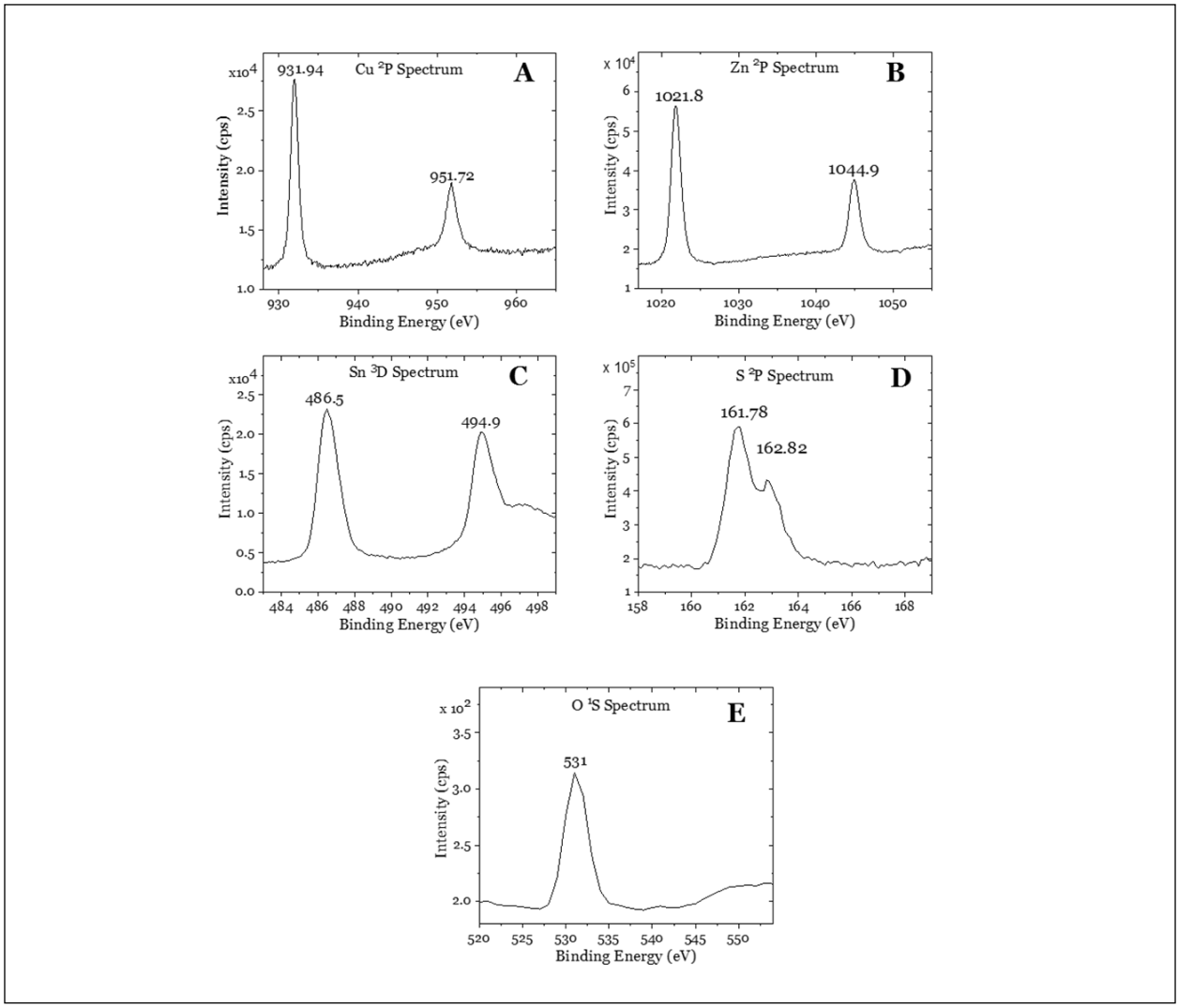

Figure 2-5: X-ray photoelectron spectroscopy (XPS) showing binding energy for (A) Cu ^2P, (B) Zn ^2P, (C) Sn ^3D, (D) S ^2P scan, and (E) O ^1S scan of CZTS annealed film.

2.3.1.3 SEM and EDS analysis

The film morphology and composition were examined using SEM-EDS analysis. As suspected, the spray deposited film displayed an amorphous structure (Figure 2-6A). Upon high-temperature annealing, the film grew into a compact and dense film with a large grain size (<1μm) as shown in Figure 2-6B. The spray parameters were refined over many trials to establish parameters that yielded finer control over film thickness. A cross-sectional SEM image (Figure 2-6C) of a film with thickness of 630 nm displayed optimum performance in photocurrent generation. The EDS analysis (Figure 2-7) showed a slightly Cu poor and Zn rich composition, which is intended for good performance.[4]

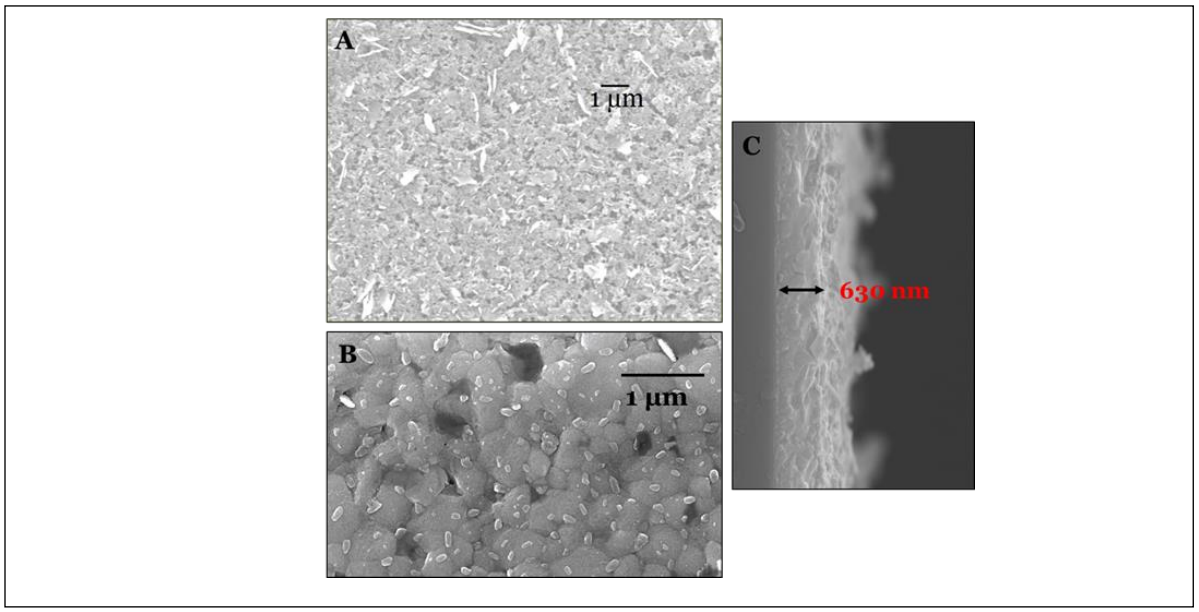

Figure 2-6: SEM image (A) Sprayed film morphology before annealing, (B) Annealed film morphology, and (C) Cross sectional SEM image.

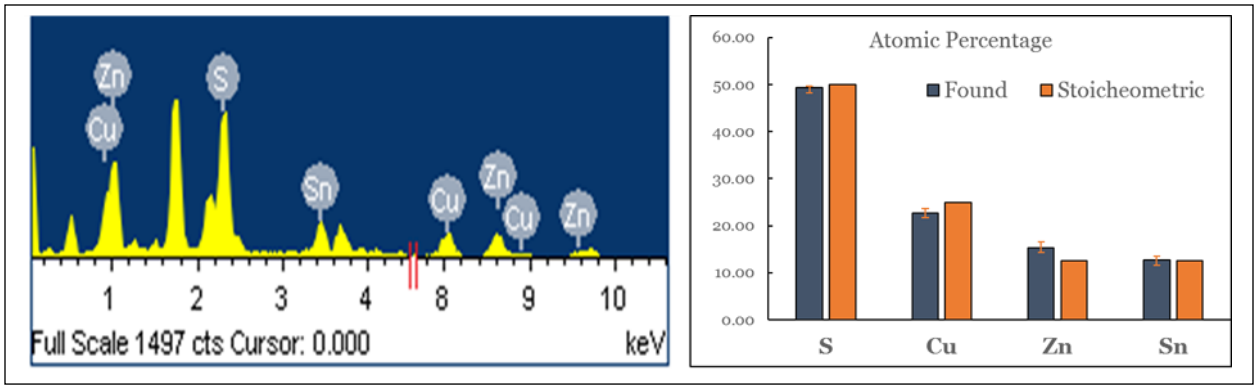

Figure 2-7: (A) EDS elemental spectrum. (B) EDS compositional analysis shows the film is slightly Cu-poor and Zn-rich in composition.

2.3.1.4 Study of phase evolution using uv-vis absorption spectroscopy

The photoelectrical property of the film was investigated using UV-Vis absorption Spectroscopy. In Figure 5A, the film shows a sharp absorption edge at 900 nm (1.37 eV) representing the band edge transition. The electronic transition was modeled[56,69] for a direct band gap semiconductor in the Tauc plot, which confirmed the semiconductor band gap of 1.4 eV (Figure 2-8B).

The flexibility of the synthesis recipe allowed us to vary the Cu and Sn composition in the precursor solution with homogenous oxidation states while keeping the counter elements constant. This permits investigation of the evolution of different phases by probing UV-vis absorption spectroscopy on the annealed films (Figure 2-8C). According to the previous reports[19], CZTS only forms within a very narrow composition window. At lower Sn composition, it is safe to assume that only binary and ternary phases such as ZnS, SnS_x, Cu_xS, and CTS (Cu_2SnS_3) exist in the film. Among these phases, Cu_xS and SnS_x are easily distinguishable from CZTS under UV-Vis spectroscopy. In the trace *a-c*, Cu_xS phase dominates, evident from its characteristic valley at ~700 nm.[67] To confirm the Cu_xS phase, we present UV-Vis spectrum for pure Cu_xS in Figures S3A.

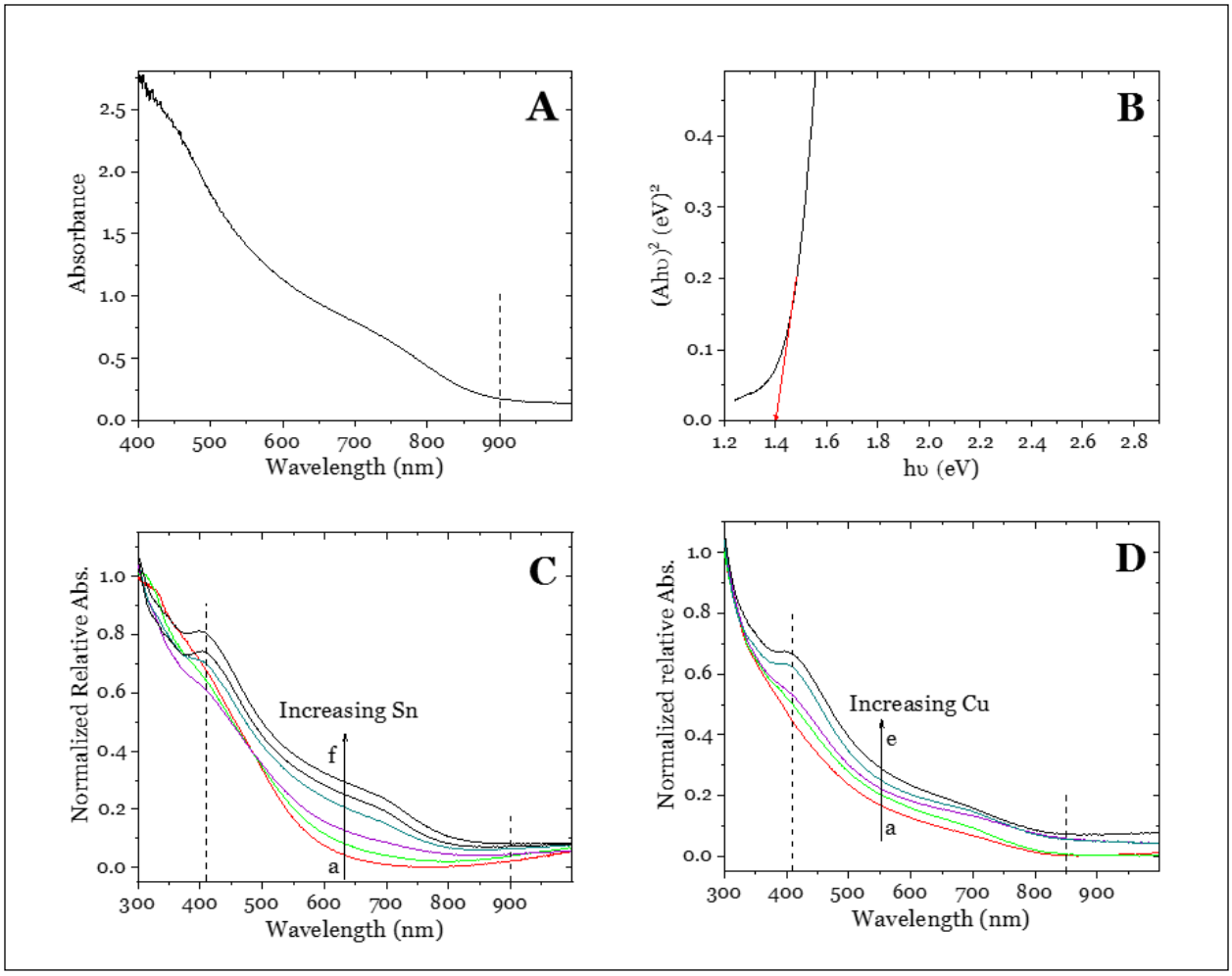

Figure 2-8: (A) UV-vis absorption spectrum of CZTS annealed film. (B) Tauc plot showing band gap energy. (C) UV-vis spectra of annealed films with varying Sn composition in the precursor solution where $\frac{Sn}{Cu+Zn}$ = (a) 0, (b) 0.06, (c) 0.12, (d) 0.18, (e) 0.24, and (f) 0.30. (D) UV-vis spectra of annealed films with varying Cu composition in the precursor solution where $\frac{Cu}{Zn+Sn}$ = (a) 0, (b) 0.21, (c) 0.42, (d) 0.64, and (e) 0.86.

The Cu_xS phase diminishes as the Sn composition increases, which can be explained by a new dominating phase (CTS) within the film. However, before reaching the stoichiometric Sn composition (trace *c-f*), the films start to develop a peak near 420 nm which is, according to the literature[82], attributed to SnS_x (x = 1 to 2) phase. The UV-Vis spectrum of SnS_x film, grown via successive ionic layer adsorption and reaction, shows an absorption peak at ~420 nm (Figure S3B, Supporting Information). Similarly, Figure 2-8D shows the effect of Cu variation on the annealed films. At the lower Cu composition, we suspect ternary CTS (band edge at 850 nm) dominates the film for the same reason discussed above. As

the Cu composition approaches the stoichiometry, the SnS phase becomes evident (trace *d-e*). Binary Cu_xS is a low band gap n-type semiconductor which creates a short circuit within the film, therefore, dramatically reduces carrier density.[51] Binary SnS_x is a wide band gap (indirect) semiconductor which reduces energy efficiency. Moreover, the grain boundaries between CZTS and binary phases act like recombination sites for the charge carrier. Our study suggests that to minimize the SnS_x phase in the film, a Cu poor and Sn poor composition must be attained. The findings agree with the "Cu poor and Zn rich" notion for improved performance which has been observed previously[83–86] via vapor deposition techniques.

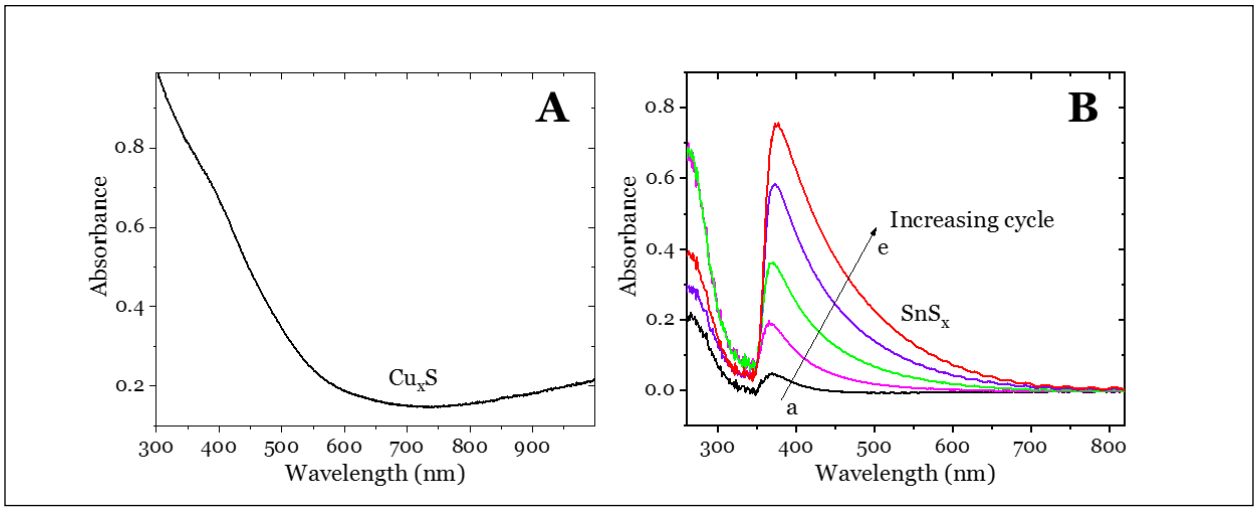

Figure 2-9: (A) UV-vis absorption profile of CuxS sprayed film prepared by mixing 1.87 mmol CuCl2 and 6 mmol thiourea in a 20 mL methanol-water mixture (80-20 wt.%). The resulting light green solution was sprayed onto a preheated FTO substrate (~300 ^oC) using a spray pen. (B) UV-vis absorption profile of SnSx film grown onto TiO2 (baseline) via successive ionic layer adsorption and reaction (SILAR) a-e represents film after 1-5 cycles. The SnSx SILAR film was grown onto mesoporous TiO2 film with a 0.02 M SnCl2 solution (pH 1.3 adjusted with HCl) as the cationic precursor and a 0.02 M Na_2S solution as the anionic precursor solution.

2.3.1.5 Photoelectrochemical Response of CZTS thin film.

To study the photoresponse, the annealed film was employed as the working electrode in a three-electrode photoelectrochemical cell (PEC) with Ag/Ag^+ as reference, Pt as counter electrode, and Eu^{2+}/Eu^{3+} aqueous redox couple (0.2 M) as the electrolyte solution. This characterization technique provides a quick performance testing for the absorber layer without requiring to build a multilayer photovoltaic device.[87]

The Eu^{2+}/Eu^{3+} redox couple has been shown to stabilize the CZTS-electrolyte interface while the standard redox fermi level falls within the band gap energy level of CZTS[88] (Figure 2-10). Figure 2-11A shows the three-electrode configuration of the PEC. The film was illuminated by 100 mW/cm^2 simulated sunlight using a 300W Xe lamp that was first passed through an AM 1.5 filter. In Figure 2-11B, the linear sweep voltammetry (LSV) shows that the photocurrent (difference between light and dark current) increases steadily from -320 mV to -1V *vs.* Ag/AgCl. The negative photocurrent indicates electron injection into the electrolyte at interface of working electrode. This electrochemical behavior is expected for a p-type photoelectrode.[88] As illustrated in Figure 2-11C, in addition to the diffusive separation mechanism, the band bending at the bulk film-liquid interface promotes separation for the photogenerated charge carriers.[38,89] The stability of the photocurrent is shown in the J-t curve as a function of time (Figure 2-11D) under -500 mV applied bias *vs.* Ag/AgCl. The current response with an intermittent cycle of dark and illuminated conditions shows that the resulting photocurrent is stable for a long period of time, which is a drastic improvement from previously reported values.[88,90–92] This improvement can be attributed to the lesser degree of binary phases obtained from careful choice of cations in the precursor solution.

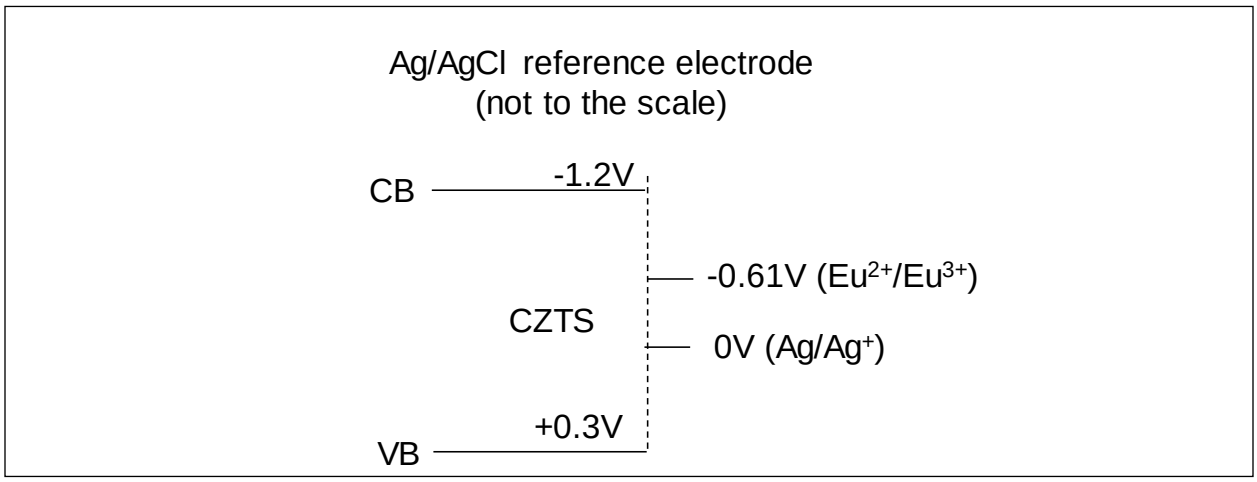

Figure 2-10: Relative band positions of CZTS and Eu^{2+}/Eu^{3+} redox fermi level with respect to Ag/AgCl reference electrode.

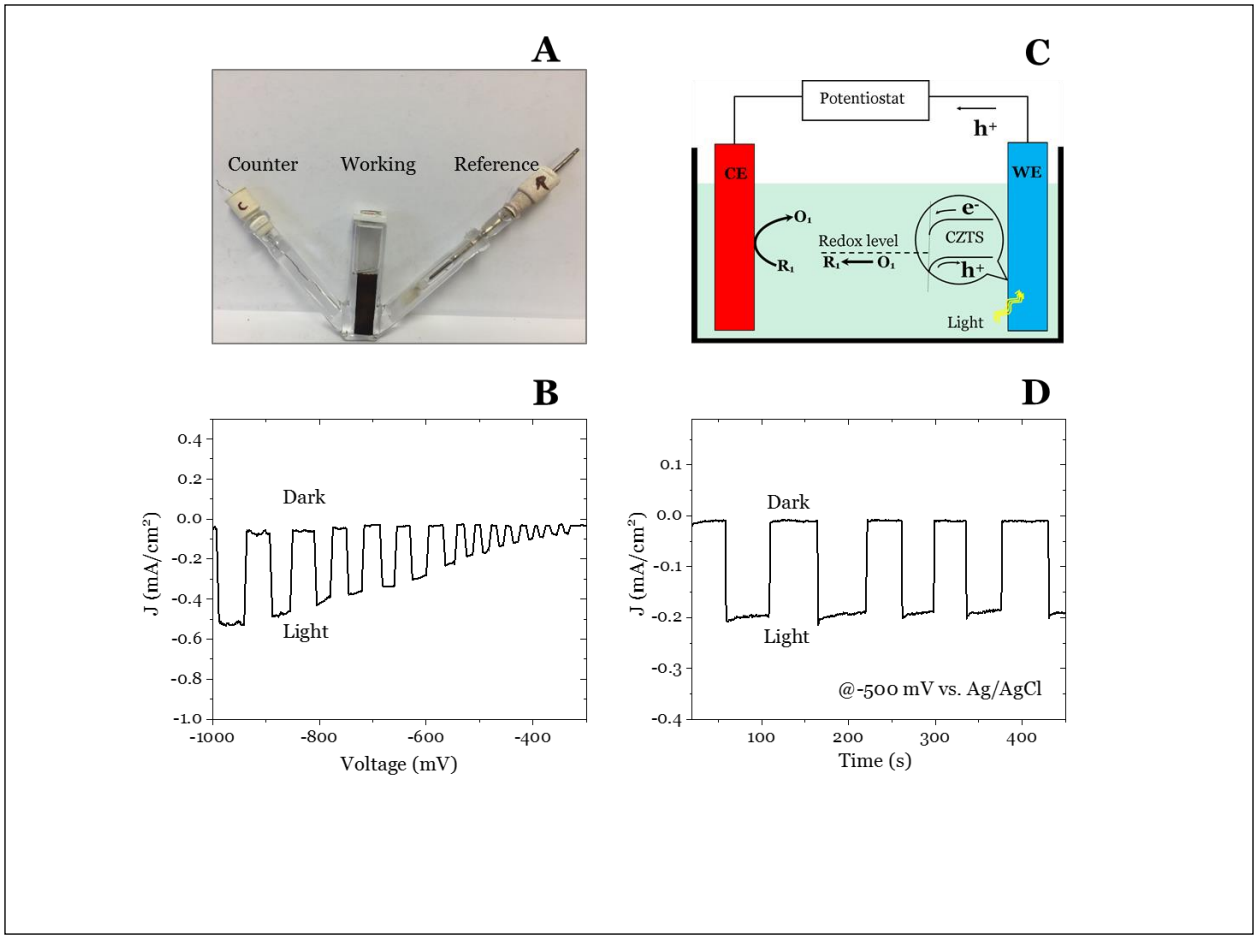

Figure 2-11: (A) Three electrode photoelectrochemical cell image, (B) Charge separation mechanism at the solid liquid interface, (C) Linear sweep voltammetry of CZTS film under dark and illumination depicts p-type semiconductor response under AM 1.5 simulated solar flux at 100 mW/cm^2, and (D) Current density vs. time plot at -500mV for shows stable electrode performance with reference Ag/AgCl, Pt as counter and 0.2 M $EuCl_3$ in water as electrolyte solution.

2.4 Summary

The precursor solution approach has been proven to generate the best quality film for solar energy absorption. However, the air stability of the solution has been a prolonged issue that needs to be addressed. In this report, a systematic approach was acquired to develop a stable and flexible precursor solution by selecting the oxidation states of metal ions corresponding to CZTS. The precursor solution was spray deposited onto preheated FTO and annealed at 470 ^oC under SnS and S atmosphere. Results from Raman studies have indicated 8 Raman active modes in the annealed samples using only green light (514 nm)

excitation. The flexibility of the solution was utilized to show binary phase evolution for the first time, to our best knowledge, by probing the UV-Vis absorption spectra. By varying the Cu and Sn composition variation, we found that impure SnS_x phase develops under Cu rich and Sn rich condition. To maximize the film performance, a Cu and Sn deficient film was suggested. The easily reproducible photocathodes were employed in a three-electrode photoelectrochemical cell to test the performance as solar absorbing layer. The photocurrent increases with applied negative bias vs Ag/AgCl reference electrode. The photocurrent at a fixed bias was found stable over an extended period of time.

Chapter 3

3 Carrier Lifetime and Charge Separation in K^+-Doped CZTS Nanocrystals

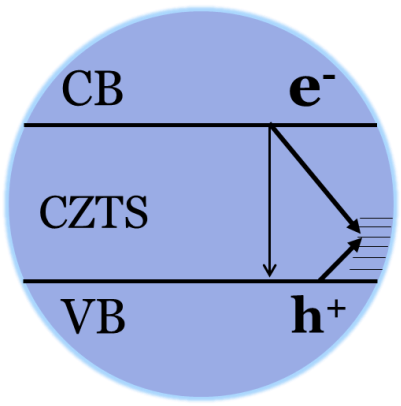

Fast Recombination

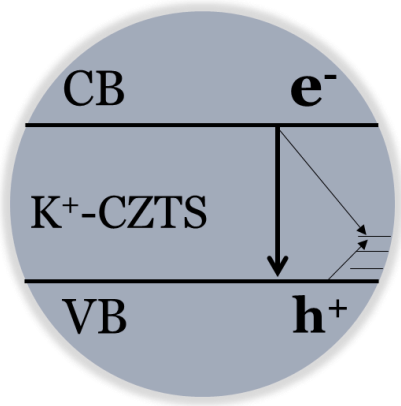

Slow Recombination

3.1 Introduction

Kesterite quaternary semiconductor Cu_2ZnSnS_4 (CZTS) holds promise as an earth abundant, inexpensive material for next generation solar energy conversion strategies.[93,94] The p-type semiconductor has a direct band gap energy of ~1.5 eV which falls within the optimum range for the absorption of solar radiation on earth's surface.[35,48,95,96] The relatively high absorption coefficient (~10^4 cm^{-1}) enables nearly complete light absorption within only a few micrometers of thin film constructs.[96] However, CZTS primarily suffers from balancing light absorption with minority carrier transport. While nearly all photons of sufficient energy are absorbed within 1-2 μm, the upper-bound electron diffusion length has been estimated from fluorescence lifetime measurements to be ~200 nm in vacuum deposited thin films of high quality.[94] Grain boundaries and intrinsic point defects in Cu poor/Zn rich CZTS film such as sulfur vacancy -V_S, Sn on Cu anti-site - Sn_{Cu}, and Cu on Zn antisite - Cu_{Zn} within the thin film are thought responsible for the low carrier lifetime and, by extension, carrier diffusion length.[97,98]

Doping CZTS with alkali metal ions such as Na^+ increases the carrier lifetime and charge density by passivating defect sites and increasing free carrier concentration.[99–104] Accordingly, Na^+ has been shown to suppress formation of binary compound ZnS, which induces recombination by trapping carriers at ZnS-CZTS interfaces. The highest-performing CZTS photovoltaics are fabricated using soda lime glass (SLG), which facilitates diffusion of Na^+ impurity during high-temperature annealing. Recently, doping CZTS thin films with K^+ has been shown to be more effective in improving grain boundary defects than Na^+.[105] The highest recorded efficiency of CIGSe based solar cell, which is considered the analogue to CZTS, was achieved using K^+-doped thin film.[106] Significant improvements in thin film photoresponse were reported with proposed mechanisms similar to those observed with Na^+-doping.[102] Despite such promising results, little is

known regarding the fundamental nature of the role of K^+ in improving the photoresponse of CZTS, particularly in nanocrystalline form.

Nanocrystal (NC) synthesis methods have been developed to produce monodisperse CZTS particles that act as building blocks for CZTS thin films.[107–110] The NCs can be synthesized in a variety of ways that allow strict control over the resulting material and thin film properties.[94,111,112] NCs typically undergo ligand exchange to reduce carbon content and are annealed at high temperature to produce the CZTS thin films, which are employed as photoactive layer in photovoltaic cells.[104–109,113–115]

Our objective in this study was to elucidate the role of potassium doping in improving the CZTS photoresponse. We first developed a reproducible and flexible synthesis to produce undoped and K^+-doped CZTS NCs. The NCs were then subjected to ligand-exchange, dispersed in water, and spray-deposited onto preheated transparent oxide conductor to produce nanocrystalline thin films. We did not anneal the thin films, which induces grain growth and better CZTS phase purity. Instead, we focused on the fundamental photoresponse of NC thin films so we could eliminate the well-established role alkali metal dopants play during annealing. Surface-enhanced Raman spectroscopy, XPS, transmission electron microscopy (TEM), energy-dispersive x-ray spectroscopy (EDS), x-ray fluorescence (XRF), and transient absorption spectroscopy (TAS) were used to characterize doped and undoped CZTS NCs. We employed the doped and undoped CZTS NC photocathodes in a photoelectrochemical cell to probe the photoresponse. The results show K^+ doping of CZTS NCs reduces impurity phases and slightly changes the surface chemistry to a more K^+ rich environment. These factors give way to a significant increase in the excited state lifetime, which enables a higher degree of charge separation and therefore photocurrent. Figure 3-1 depicts the overall NC synthesis and photocathode preparation steps. NCs were synthesized in a 3-neck

flask via heat up and hot injection methods. After washing, chloroform dispersed NC were subjected to ligand exchange reaction using formamide (FA)-Na2S solution. After ligand exchange, NCs were dispersed in water for spraying onto FTO. Methanol was added (not shown) for spraying to improve drying processes and allow for lower temperature spray deposition process.

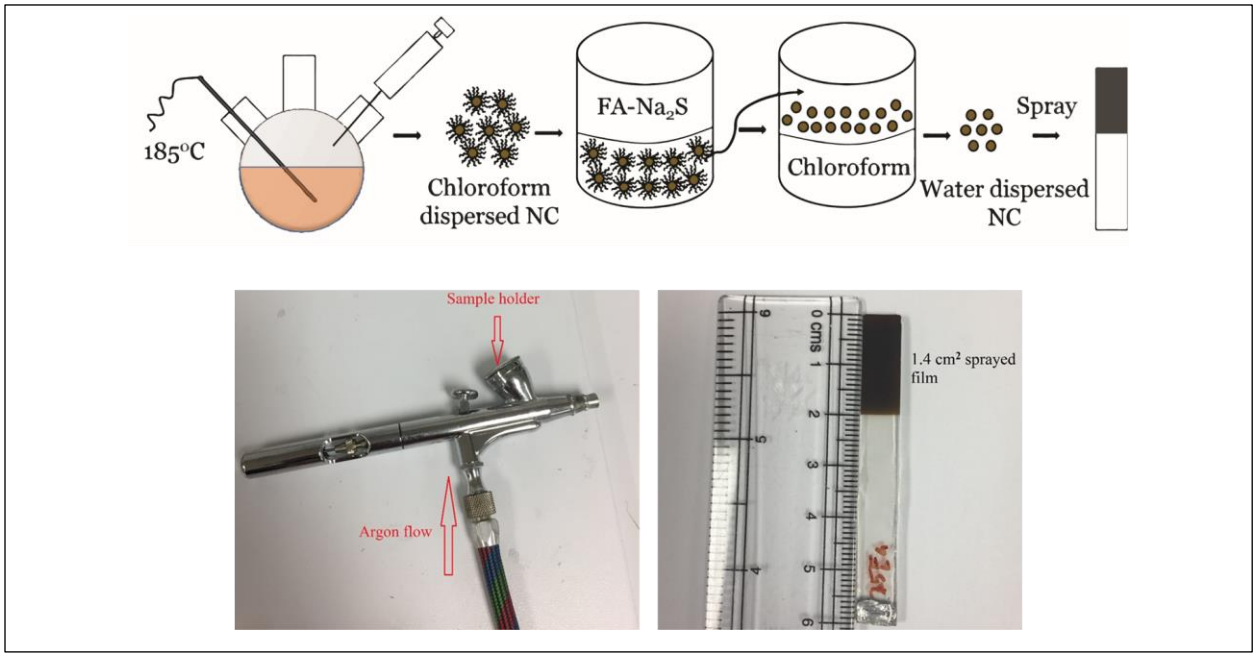

Figure 3-1: Cartoon illustration showing the route for CZTS photocathode preparation.

3.2 Experimental

3.2.1 Chemicals

The following materials were used: copper (II) acetylacetonate, 98+% (Strem Chemicals); zinc acetate, anhydrous, 99.98% (Alfa Aesar); tin (IV) chloride pentahydrate, 98% (Strem Chemicals); sulfur powder, -325 mesh, 99.5% (Alfa Aesar); potassium acetate, anhydrous (VWR); disodium sulfide (Anachemia); oleylamine, >50.0% (Tokyo Chemical Industry); formamide,

ACS, 99.5+% (Alfa Aesar); chloroform, 99.8+% (EMD Millipore Corporation); ethyl alcohol 190 Proof, 95% (Pharmco-Aaper).

3.2.2 Methods

3.2.2.1 Nanocrystal Synthesis

The nanocrystal synthesis via hot injection (HI) method was modified from Steinhagen et al.[116] In a typical synthesis, 0.935 mmol copper acetylacetonate, 0.7 mmol zinc acetate, and 0.475 mmol tin (IV) chloride were mixed with 15 mL oleylamine (OLA) in a three-neck flask. Here, Sn^{4+} salt was used to achieve the appropriate oxidation state with respect to CZTS, and the OLA was found to reduce the Cu^{2+} to Cu^{+} as apparent by color change from blue to light green.[113] The flask was degassed and placed under N_2 blanket while the temperature was raised to 185 ^{o}C. Once the solution turned transparent-orange, 5 mL of degassed OLA-S (4 mmol S dissolved in 5 mL OLA) solution was injected. The solution turned black immediately due to burst nucleation, and nanocrystal growth continues as the temperature rose to 270 ^{o}C. The temperature was held for 1.5 hours to complete the growth process. To carry out synthesis of potassium-doped CZTS, K^{+} was introduced at the beginning with other metal sources to serve as dopant to CZTS NC *via* potassium acetate. The NCs were washed twice (three washes rendered the resulting dispersion kinetically unstable for the duration required to prepare the photocathodes) and dispersed in chloroform for further processing into photocathodes.

3.2.2.2 Surface modification through ligand exchange reaction

The NCs were further processed through ligand exchange reaction before fabricating photocathodes. Ligand exchange reactions were carried out with Na_2S-formamide solutions.[95]

Typically, 0.453 g of Na_2S. $7H_2O$ was dissolved in 5 mL formamide for 44 mg of CZTS NC dispersed in chloroform. The ligand exchange reaction was carried out in a vial with rapid stirring for up to 6 hours. At the end of the reaction the NCs became dispersed in formamide, which left transparent chloroform remaining at the bottom of the vial. The NCs were separated by adding 5 mL water and 30 mL ethanol followed by centrifugation at 5000 RPM for 5 minutes. The NCs were redispersed in 3 mL water by ultra-sonication and precipitated again by centrifugation after adding 40 mL ethanol. The NC were redispersed in water and centrifuged at 5000 RPM to remove coarse particles. The dispersion was bubbled with N_2 gas before storing in the dark and found to be stable for months if properly stored.

3.2.2.3 Photocathode Preparation

The photocathode was prepared by spraying the NC dispersion onto cleaned FTO glass substrate preheated to 270-300 ^oC. NCs were dispersed in a mixture of 80 vol% methanol and 20 vol% water to produce photoactive films *via* lower drying stresses in films. Drying stresses lead to cracking, delamination, and other macroscale defects that were eliminated by using the solvent mixture. Methanol further improved the spray deposition process by enabling a lower substrate temperature. Typically, a 1 mg/mL NC dispersion was used for spraying to achieve a homogenous film employing a spray pen.

3.3 Results and Discussions

3.3.1 Synthesis and Characterization of CZTS NCs.

We first monitored the evolution of CZTS nanocrystals as a function of temperature utilizing a direct-heating method. Precursors were introduced to the flask simultaneously

(including sulfur, which is typically injected), and the temperature was raised from 150 °C to 270 °C at 5 °C/min. UV-Visible absorption spectra (UV-Vis) were collected at different temperatures to track growth of the NCs following nucleation, which we observed *via* color change at ~190 °C. The rationale for this approach was twofold. First, CZTS is quaternary and often contains impurity phases such as ZnS, Cu_xS, SnS_x, and CTS (Cu_2SnS_3). Among these impurity phases, Cu_xS and SnS_x are observable in the UV-vis spectrum. Second, we aimed to establish an injection temperature where these binary phases were minimized. Figure 3-2A shows the evolution of the CZTS phase as a function of temperature from 190 °C to 270 °C. As can be seen in the figure, trace *a* contains the characteristic valley of Cu_2S at ~800 nm, which is no longer present and instead CZTS absorption spectrum is obtained as the temperature increases above 200 °C. The evolution of the absorption spectra as a function of increasing temperature suggests Cu_xS nuclei initiate the synthesis, after which, according to previous reports, slower-reacting Zn/Sn begin to drive the nanocrystal growth toward CTS and eventually CZTS phase.[81] The TEM image (Figure 3-2B) of the final NCs (270 °C) shows a high degree of polydispersity in particle size.

Figure 3-2C compares the UV-Vis of the undoped and K^+-doped NC products in the HI synthesis method and shows the nanocrystal absorption characteristics are nearly identical. The TEM image in Figure 3-2D suggests much lower polydispersity can be obtained from HI synthesis compared to the direct heating method (Figure 3-2B). The stark contrast between the polydispersity of the NCs implies a burst nucleation process following HI of sulfur-oleylamine solution at 185 °C. After burst nucleation, the subsequent growth period (until the temperature reaches 270 °C) is consistent for all nuclei, which results in good control over the nanocrystal size.[117] However, HI synthesis yields NCs of slightly larger average size (~30-40 nm). Previous reports suggest this is within the optimal size regime for CZTS thin films prepared from NCs.[110]

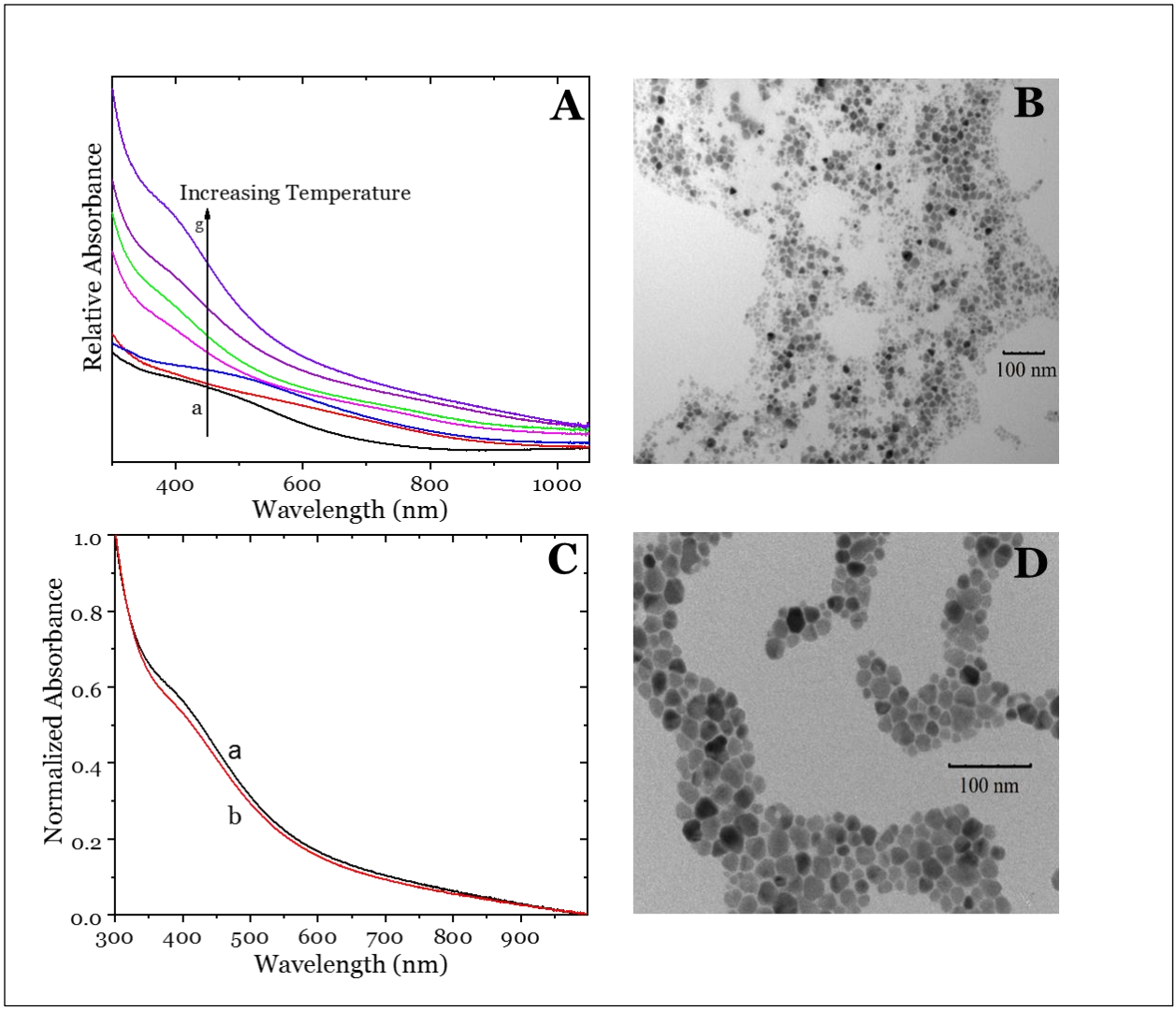

Figure 3-2: (A) UV-vis absorption spectra of NCs synthesized (via heat up method) at (a) 190 ºC (b) 200 ºC (c) 210 ºC (d) 220 ºC (e) 230 ºC (f) 250 ºC (g) 270 ºC. The low-temperature spectra suggest CuxS phase initiates the growth of CZTS NCs, as the absorbance increase from ~800 nm to 1000 nm is characteristic of Cu_xS phases, (B) TEM imaging of NCs synthesized by heat up method show high degree of polydispersity and random shapes, (C) UV-vis absorption spectroscopy of hot injection CZTS in (a) undoped (b) 1.4% K^+-doped NCs, (D) TEM imaging of NCs synthesized by hot injection method demonstrates higher degree of size and shape control over the NCs, albeit with overall larger average NC size. The percentage of K^+ doping was calculated based on Cu mole.

The slight depression of the peak at 420 nm in the K^+-doped NCs is thought to be a reduction of SnS phase as previously mentioned.[82] To confirm this, we carried out additional experiments employing sequential bath deposition of SnS.[118] The UV-Vis absorption profile in Figure 3-3A shows the evolution of the primary absorption peak for SnS at ~400 nm, which

undergoes quantized red-shifts as the crystallite size increases with subsequent immersion cycles and the band gap approaches the bulk value. The effect of K^+-doping on CZTS phase purity and lattice structure were further investigated using x-ray diffraction (XRD) and Raman spectroscopy. We first probed the CZTS NCs using XRD in the event that K^+-doping would result in a shift of one or more peaks as a result of its inclusion within the crystal structure through replacement of Cu^+ rather than as an intercalant (atomic radii: Cu = 1.28 Å; K = 2.8 Å). The XRD diffractogram for the undoped and K^+-doped CZTS NCs are provided in Figure 3-3B, and no significant differences in the diffractograms are noted. Overlap in the diffraction peaks of undoped and K^+-doped CZTS implies K^+ does not significantly alter the d-spacing of low dimensional planes. However, we did observe minor peak broadening in the K^+ doped sample (FWHM data are reported in Table 1). Impurity phases were not immediately evident from XRD, but only select impurities can be resolved since a significant number of the peaks corresponding to the CZTS kesterite phase overlap with the binary ZnS and tertiary CTS phases.[119]

Table 3-1 FWHM data of the major XRD peaks for undoped & 15% K^+ doped (maximum doping load) CZTS NC aggregated powders.

Planes	FWHM (deg)	
	0%	15%
1 (112)	1.07	1.08
2 (200)	0.28	0.36
3 (220)	0.84	0.91
4 (312)	0.98	1.11
5 (008)	0.01	0.02
6 (332)	0.18	0.30

In order to circumvent this and better resolve phase impurities, Raman spectroscopy was employed to probe the kesterite CZTS phase as done in previous studies.[120–122] CZTS shows a Raman strong-shift between 330-339 cm^{-1} and two additional weak-shifts at 285-295 cm^{-1} and 371-373 cm^{-1}.[123] We first employed standard Raman spectroscopy on CZTS NC powder samples obtained by varying the amount of K^+ introduced to the precursor solution. The Raman spectra presented in Figure 3-3C demonstrate a continual shift of the strong-shift peak to higher wavenumber corresponding to increasing initial K^+ concentration, which mirrors previous findings in solution-processed K^+-doped CZTS thin films.[102,124,125] However, traditional Raman spectroscopy generates very broad spectra for CZTS NCs and convolutes the observable peaks corresponding to binary/ternary phases. We employed Surface Enhanced Raman Spectroscopy (SERS) to better resolve the phase purity of the as-prepared NCs. SERS spectra provided in Figure 3-3D show a slight reduction of ZnS and CTS phases for K^+-doped sample. We also continue to observe slight increase in wavenumber from 332 cm^{-1} to 336 cm^{-1} in the strong-shift of the SERS spectra for the K^+ doped sample.

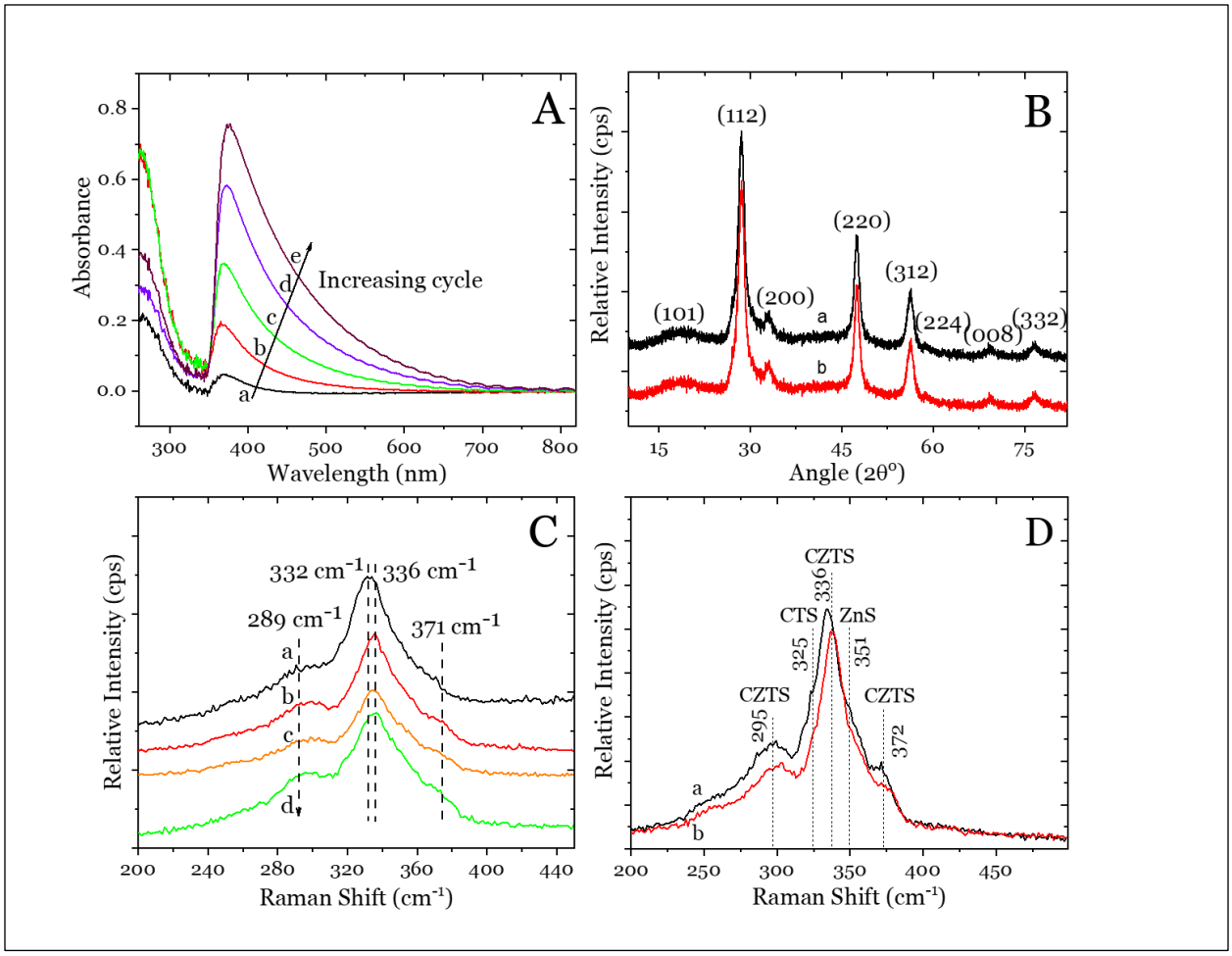

Figure 3-3: (A) UV-vis of a SnS_x-sensitized TiO_2 mesoscopic thin film depicting the evolution of primary absorption peak near 400 nm, which is similar to the observed peak at ~420 nm in the UV-vis for as-synthesized CZTS NCs. (B) X-ray diffractogram for (a) CZTS (b) 15% K^+-doped CZTS (at 15% dopant addition to the initial flask conditions, we anticipate the highest level of K^+ incorporation into the CZTS NCs, which would impact diffractograms to the highest degree if any impacts are observable). (C) Raman spectroscopy of (a) undoped (b) 1.4% K^+-doped (c) 5% K^+-doped (d) 15% K^+-doped CZTS NC aggregated powders. (D) Surface Enhanced Raman Spectroscopy (SERS) of (a) undoped (b) 1.4% K^+-doped CZTS NC. Approximately 2 nm Au islands were formed *via* sputtering Au onto CZTS NC film. Raman spectrometer scan settings for all measurements: 532 nm excitation wavelength, Si peak at 508 cm^{-1}, 5 % laser power, 10s, 20 accumulations. Initial K/Cu molar ratio of 0.014 at the initiation of the synthesis is referred as 1.4% doping.

3.3.2 Fabrication and Characterization of CZTS Photocathodes.

CZTS thin films were fabricated *via* spray-deposition as discussed in the experimental details. The films were first characterized using UV-vis, SEM/EDS, x-ray fluorescence (XRF), and XPS before carrying out photoelectrochemical testing. UV-vis was used to investigate the absorption characteristics of the CZTS thin film photocathodes and was used to estimate the film thickness (Figure 3-4A). The absorption features of the best performing films demonstrate a smoothing of the peak at 420 nm after spraying at elevated temperature. This is not unexpected since elevated temperatures during annealing processes for producing high-quality CZTS thin films reduce grain boundaries and reform impurity phases into kesterite phase. Furthermore, the Tauc plot (inset) shows the band gap of the K^+-doped CZTS photocathode is 1.5 eV, which corresponds to the reported bulk band gap of kesterite CZTS. SEM imaging (Figure 3-4B) depicts a rough photocathode surface, which we posit is a result of the steep thermal gradients (and resulting rapid drying rates) at or near the FTO surface during deposition onto the heated substrate.

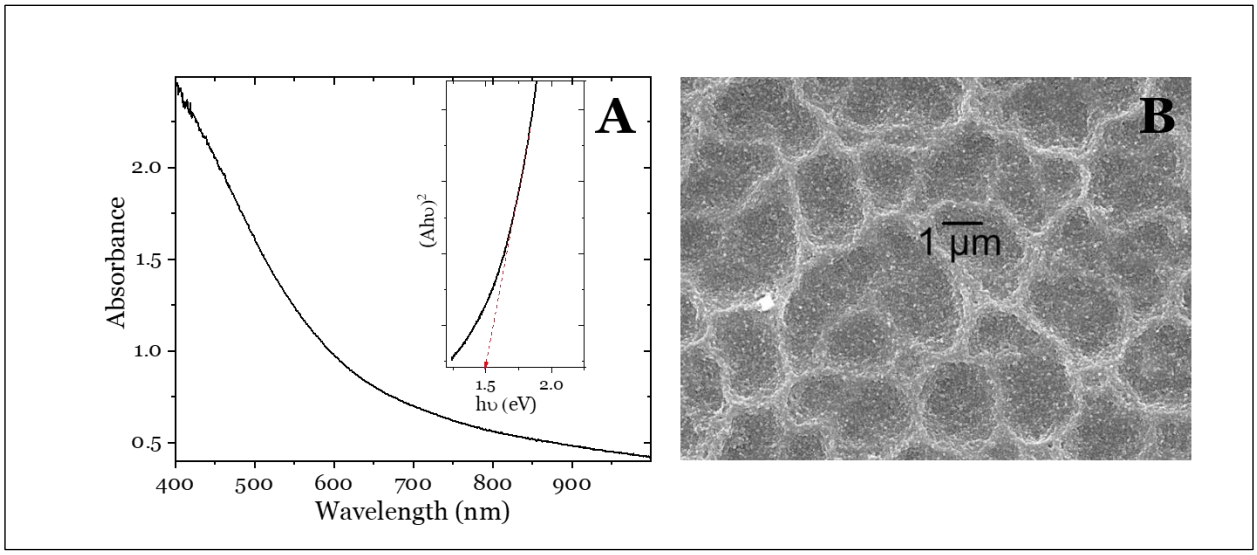

Figure 3-4: (A) UV Vis absorption spectroscopy of the NC film sprayed onto FTO glass substrate. Inset: Tauc plot to determine the band gap of the sprayed K^+-doped CZTS film. (B) SEM image depicting the surface topology of the sprayed film. Thermal gradients and rapid drying lead to crater development in the surface of the NC film.

EDS spectra and corresponding compositional analyses are presented in Figure 3-5. We performed confirmatory XRF analysis (Figure 3-5C) as EDS can sometimes exhibit a wide margin of error. However, the calculated composition of the samples obtained from both EDS and XRF match to within 1%.

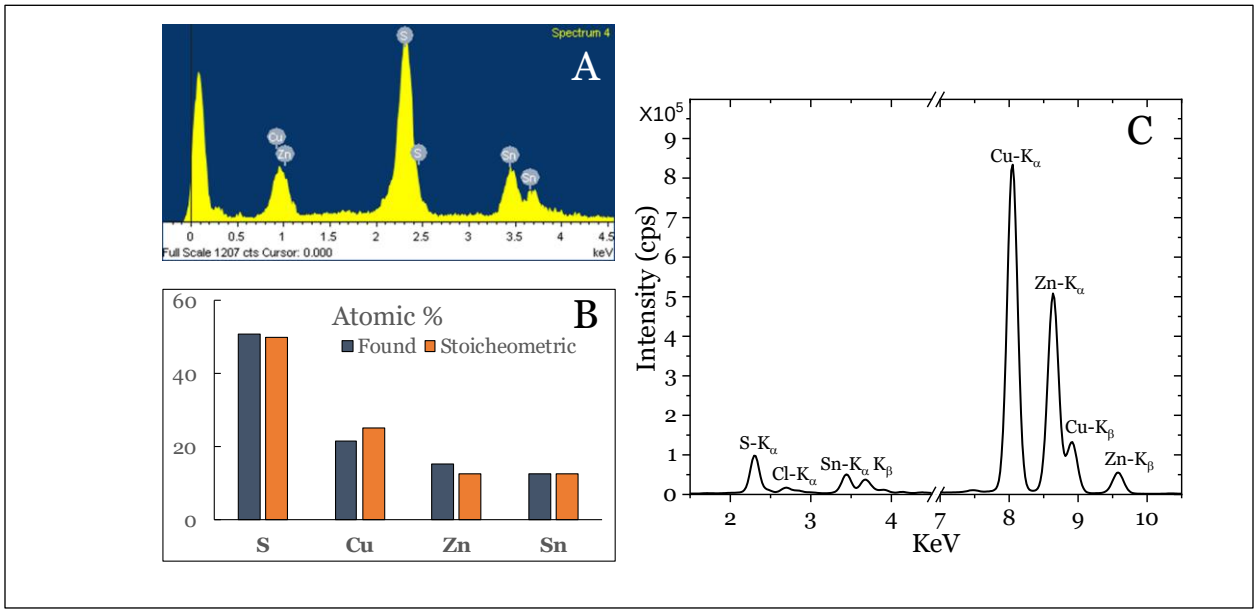

Figure 3-5: (A)-(B) EDS compositional analysis of undoped NC aggregated powder showed slightly Cu poor and Zinc rich composition. (C) X-ray fluorescence (XRF) spectra for undoped CZTS. The K_α and K_β as displayed are the prominent peaks observed under XRF. EDS Cu/Zn ratio calculated as ~1.53; XRF Cu/Zn ratio calculated as ~1.52.

XPS was employed to probe the surface composition of the as-prepared nanocrystalline CZTS thin films. Several important findings were uncovered. First, the relative intensity of the primary cations shown in Figure 3-6A-C (Cu, Zn, Sn) in undoped CZTS is higher than that within K^+-doped CZTS. Moreover, the relative intensity of the sulfur peaks in undoped and doped CZTS presented in Figure 3-6D is inverted with K^+-doped CZTS showing higher intensity of the sulfur peaks. This result suggests the K^+-doped CZTS leads to fewer sulfur vacancy surface defects and lower cation/sulfur ratio on the surface. The K^+-doped CZTS thin film also contains an additional

peak at 293 and 296 eV (Figure 3-6E), which corresponds to K ^{2}P transition and confirms the presence of K^+ dopant on the surface of the doped sample. K ^{2}P peaks were not evident in undoped sample. (Adventitious carbon peak at ~286 eV in Figure 3-6E was used to standardize XPS scans.) Characteristic sodium peak was observed at 1071 eV for both doped and undoped films, which originates from the ligand-exchange process. We note the K^+-doped film shows lower sodium peak intensity (Figure 3-6F), suggesting K^+ resides on the surface of the NCs and is fractionally-replaced with Na^+ during ligand exchange. Oxygen was observed in both thin films near the characteristic energy of O ^{1}S at 531 eV (Figure 3-6G). Further investigation of the surface of CZTS NCs is warranted to understand the interplay between the synthesis/processing conditions and surface features in the NCs.

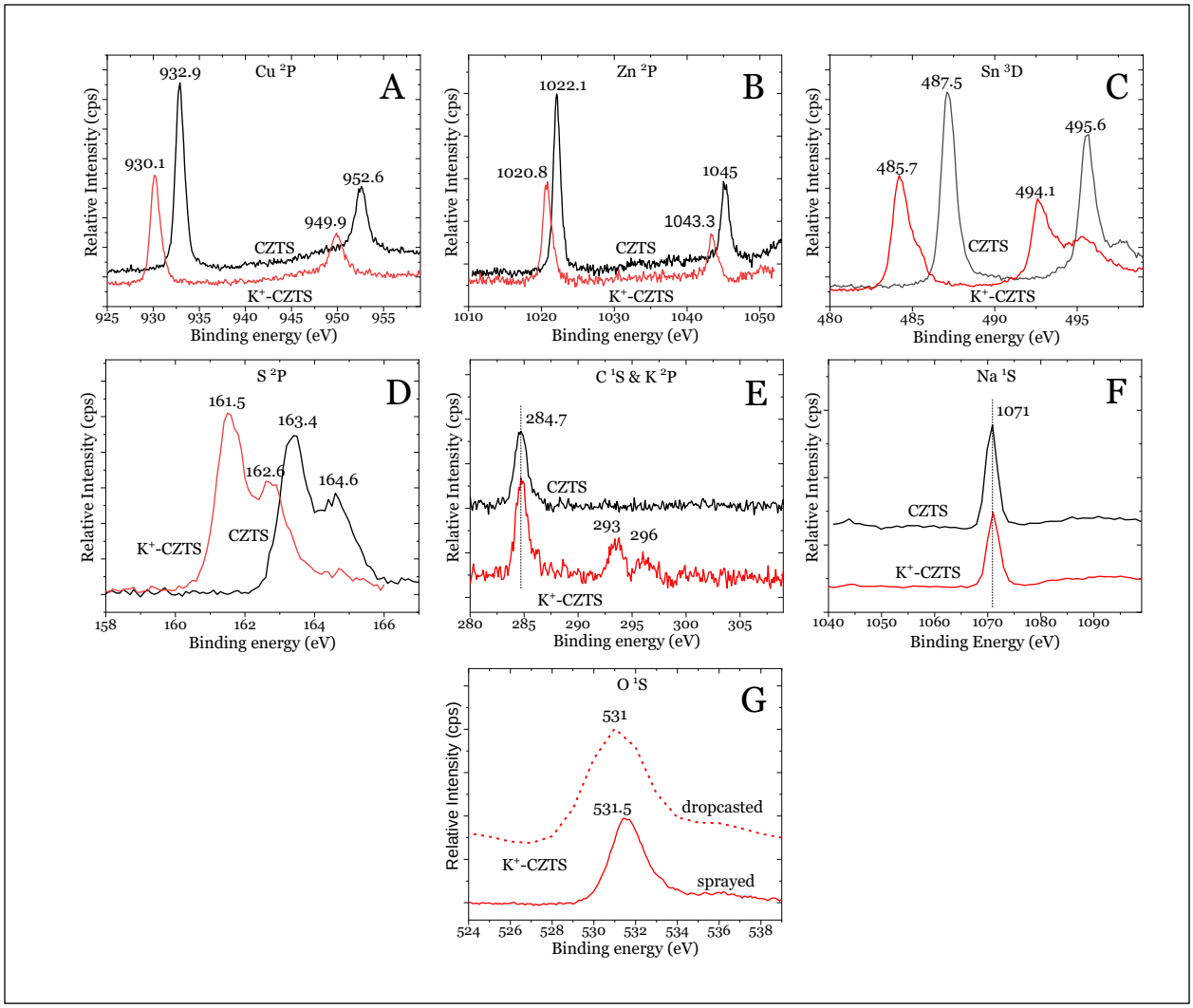

Figure 3-6: (A) – (D) XPS spectra for the primary elemental constituents of CZTS, which shows varying relative intensities of cation/anion ratio and peak-shifting in K+-doped CZTS associated with the local oxidation state and bonding environment. (E) XPS spectra showing K ^{2}P peaks present in K^{+}-doped CZTS sample and the alignment of adventitious carbon peak at ~285 eV. (F) XPS spectra of Na ^{1}S peak at 1071 eV demonstrating the success of the ligand exchange using Na_2S and the effect of the exchange on surface composition. (G) XPS spectra of prepared CZTS NC thin film photocathodes. We prepared the photocathodes using dropcast and spray methods to ascertain the influence of the heated substrate in spray-deposition of the NCs. No significant differences were observed, indicating oxidation of the NC surface results from prior synthesis and/or processing steps.

3.3.3 Probing the Excited State of CZTS Nanocrystals.

In order to better understand the impact of phase impurity remediation and passivation of K^+-CZTS NC surface on the photophysical behavior of CZTS NCs, we employed femtosecond transient absorption spectroscopy (TAS) to probe the lifetime of the photoexcited state. Generally, doping CZTS with alkali metal ions is thought to improve the excited state lifetime and charge separation efficiency through the passivation of defect sites.[126–129] TAS is a pump-probe method commonly employed to interrogate the excited state lifetime of semiconductor NCs.[130–133] We deposited CZTS and K^+-doped CZTS on mesoscopic insulating supports prepared from ZrO_2 nanoparticles and carried out pump-probe measurements on the fs-ns timescale. UV-vis absorption spectra of the physisorbed CZTS NC onto mesoscopic ZrO_2 is provided in Figure 3-7A.

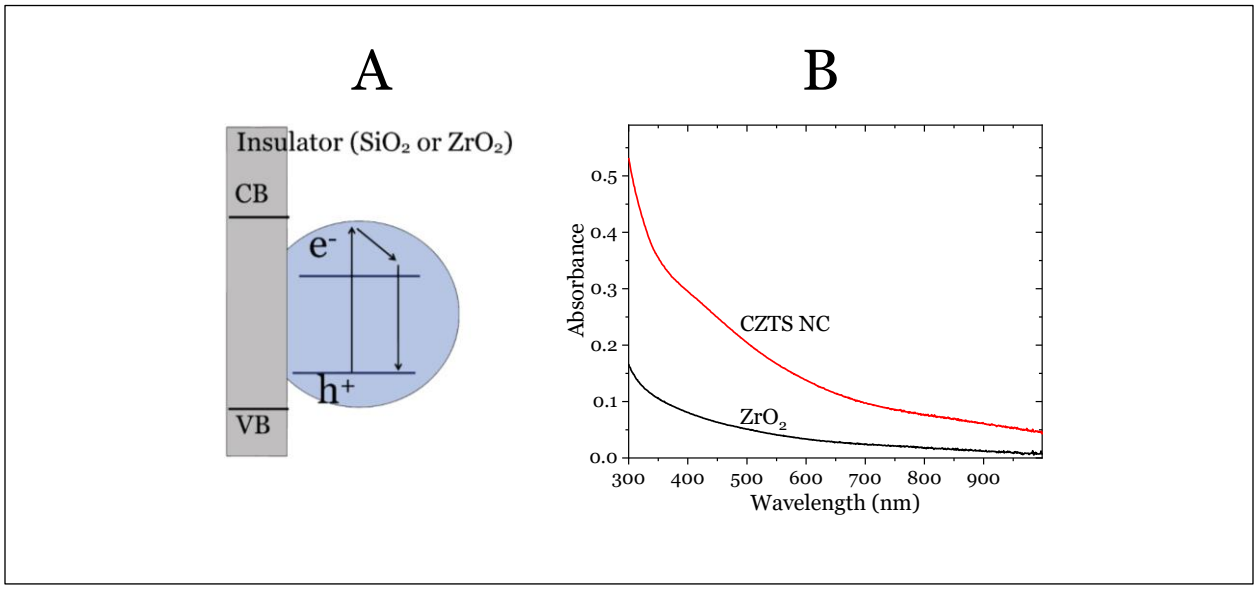

Figure 3-7: (A) Schematic for photoexcitation and predominant charge recombination pathway within the NCs during transient absorption spectroscopy experiments. (B) UV-vis absorption spectrum of ZrO_2 insulating support architecture and CZTS nanocrystal physisorbed onto porous ZrO2 film. Absorbance of films is controlled at ~0.3 at the wavelength of the excitation pulse (387 nm) for transient absorption measurements.

One can observe in Figure 3-8A a representative optical difference spectrum when CZTS is photoexcited by 387 nm pump of 130 fs temporal width. Two features are prominent in the spectrum: a transient bleach convoluted with the broad transient absorption is observed at ~520 nm at time delays beginning at 100 fs after photoexcitation, similar to that observed in prior fs spectroscopy work on CZTS NCs.[134] Pundsack and co-workers attribute the broad transient absorption to the presence of a 2nd conduction band within the CZTS electronic structure, following from prior findings in computational analyses.[17,135,136] Figure 3-8B shows the exponential decay of the difference spectra for each sample. A significant increase in the excited state lifetime for the K^+-doped CZTS (τ = 1864 ± 312 ps) NCs relative to the undoped CZTS (τ = 1169 ± 267 ps) is observed. The inset as well as the tabulated fitting parameters provided in Figure 3-8, indicate the shortest component of the lifetime is approximately the same (τ_{short} = 2.5 ps). However, this "fast" component in the undoped sample is weighted nearly 20 times more than K^+-doped CZTS in the calculation of the average lifetimes. This fast component is typically attributed to ultrafast charge trapping processes characteristic of defect-laden semiconductor NCs following photoexcitation. The TAS results reported here suggest the predominant role of K^+ in improving the photoresponse of CZTS is through the suppression of these trapping processes commonly observed in semiconductor NCs. Since we observe the rapid onset of transient absorption signal from trapped holes at surface-terminating sulfide ions, it's possible the K^+ serves as a stabilizing charge-balance during generation of sulfide radical species following photoexcitation.

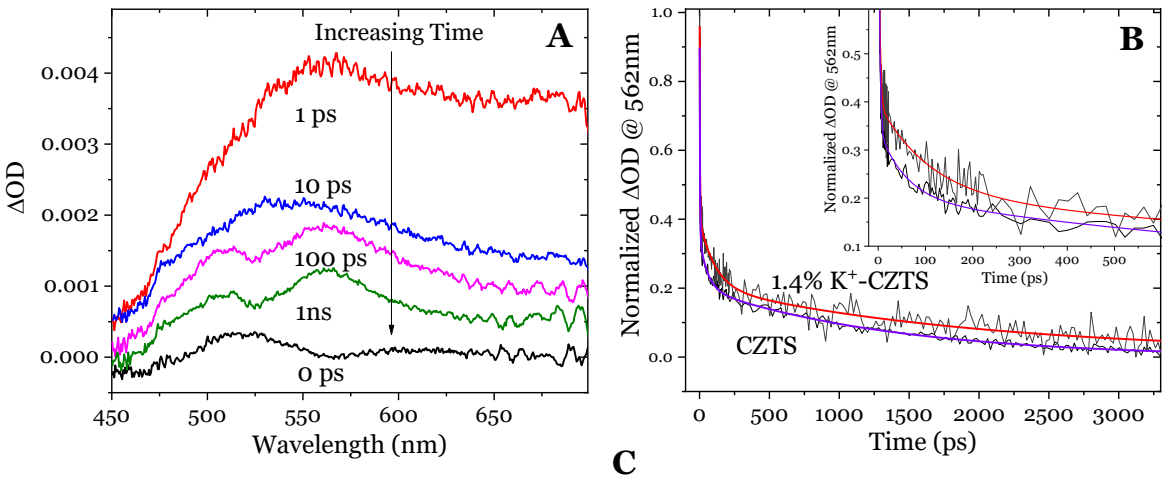

C

Parameters	Value	
	a. K^+-doped CZTS	b. CZTS
A1	0.8 ± 0.1	17.7 ± 3.7
t1 (ps)	2.5 ± 0.3	2.5 ± 0.1
A2	0.2 ± 0.03	0.8 ± 0.01
t2 (ps)	108.4 ± 7.1	56.9 ± 7.5
A3	0.2 ± 0.04	0.2 ± 0.01
t3 (ps)	1969.5 ± 305.5	1389.3 ± 274.0
Lifetime (ps)	1864.5 ± 312.9	1169.4 ± 267.4

Figure 3-8: (A) Representative transient absorption spectra of K^+-doped CZTS NC physisorbed onto ZrO_2 insulating, mesoscopic support at various delay times following excitation pulse. (B) Temporal decay of excited state transient absorption of (a) CZTS (b) K^+-doped CZTS (Inset: zoomed view of early time). Scan settings: 387 nm excitation wavelength, 0.12 mW.

We note here, however, that chalcogenides are particularly susceptible to excited state transient absorption features since the visible-absorbing chalcogen radicals ($S^{-\bullet}$, $Se^{-\bullet}$) are formed *via* hole trapping processes at surface sites.[137–139] Considering the p-type characteristics of CZTS and the resulting high density of states near the valence band,[135] we posit the observed transient absorption in our experiments corresponds to the sulfide radical species observed in other chalcogenide semiconductor nanocrystals. As a maiden attempt at unveiling the nature of the transient absorption signal in the photoexcited CZTS NCs, we introduced isopropanol as an electron donor to CZTS colloidal dispersion since the HOMO of isopropanol is above the valence

band energy of CZTS and the LUMO is far above the conduction band (Figure 3-9B). The results show faster decay when hole-scavenging isopropanol is present implying the transient absorption is related to trapped holes on the sulfur ions present on the CZTS NC surface (Figure 3-9A). While the focus of this work is not to analyze and partition the transient signals of the photoexcited CZTS NCs, we do wish to introduce this preliminary data to encourage further inquiry.

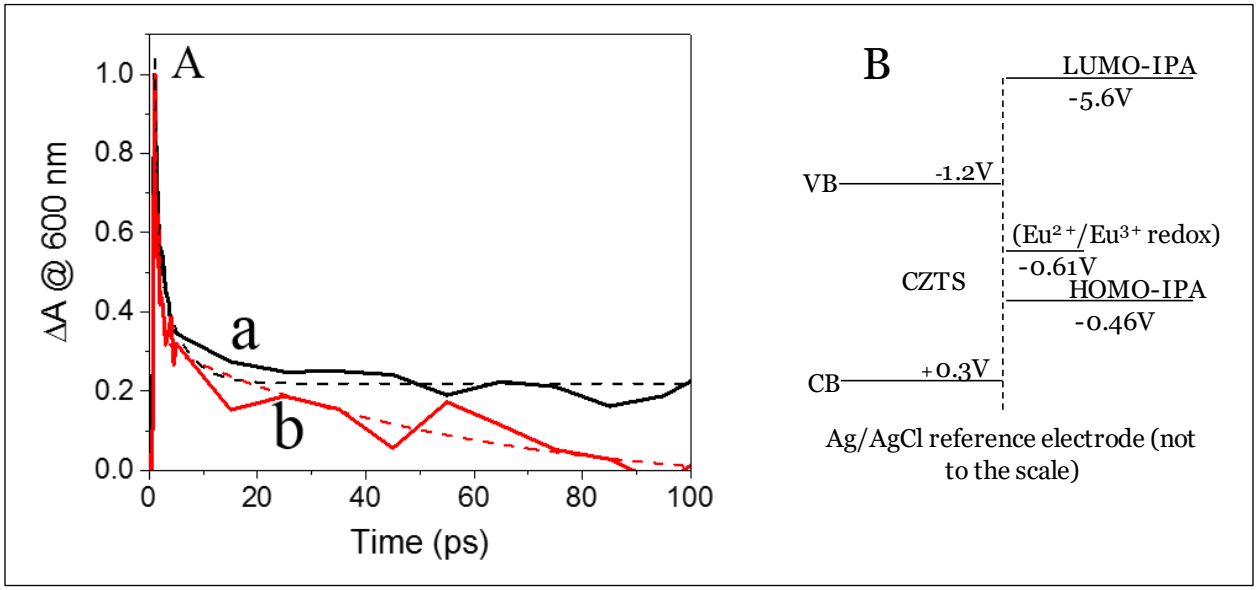

Figure 3-9: (A) Decay of transient absorption at 600 nm (a) in toluene and (b) in 2:1 toluene-isopropanol solvent. The faster decay in the transient absorption is related to the introduction of electron donor to scavenge photogenerated holes and establish the origin of the transient signal. The rate constant for hole transfer is on the order of 109 s-1, which would be expected for an upper bound transfer rate in a diffusion-controlled system. (B) Relative band position diagram with respect to Ag/AgCl reference electrode.

Our primary focus was to employ fs TAS to probe the difference in relaxation time for the excited state in CZTS and K^+-doped CZTS. It was anticipated that the remediation of defects via K^+ doping of CZTS NCs (as shown above) would yield a longer-lived excited state. We tracked the decay of the excited state at the peak wavelength of the transient absorption, 562 nm, in CZTS and K+-doped CZTS NCs to evaluate the differences. The excited state decay was modeled using

a linear combination of a minimum number of exponentials following prior works where transient spectroscopy is used to probe semiconductor NCs.[140–145]

3.3.4 Photoelectrochemical Response of K^+-doped CZTS NCs.

The spray process used to fabricate the CZTS thin films was refined over many trials to establish parameters that yielded optimum photocathodic response. Based on the absorbance of CZTS films at 600 nm and the reported absorption coefficient ($\alpha \sim 10^4$ cm^{-1}), we estimate the optimum film thickness to be ~1000 nm. The thickness of photocathodes was matched using their absorption profiles, which enabled us to control for light absorption in the films.

We introduced CZTS photocathodes to a 3-arm, custom photoelectrochemical cell to characterize the J-V characteristics (linear sweet voltammetry, LSV) and photocurrent stability (chronoamperometry). A 3-electrode configuration using Ag/Ag^+ reference, Pt counter electrode, and Eu^{2+}/Eu^{3+} redox couple was used for the photoelectrochemical tests as shown in the cartoon sketch in Figure 3-10A. The redox couple was chosen since the Eu^{2+}/Eu^{3+} Fermi level (-0.61 V vs. Ag/AgCl) falls within the band gap energy level of CZTS (Figure 3-9B).[146] Furthermore, the europium redox couple stabilizes the electrode/electrolyte interface and suppresses photocorrosion processes as reported previously.[147–152] We utilized the 3-electrode setup to isolate the photocathodic response without convolving the redox kinetic response at the counter electrode.

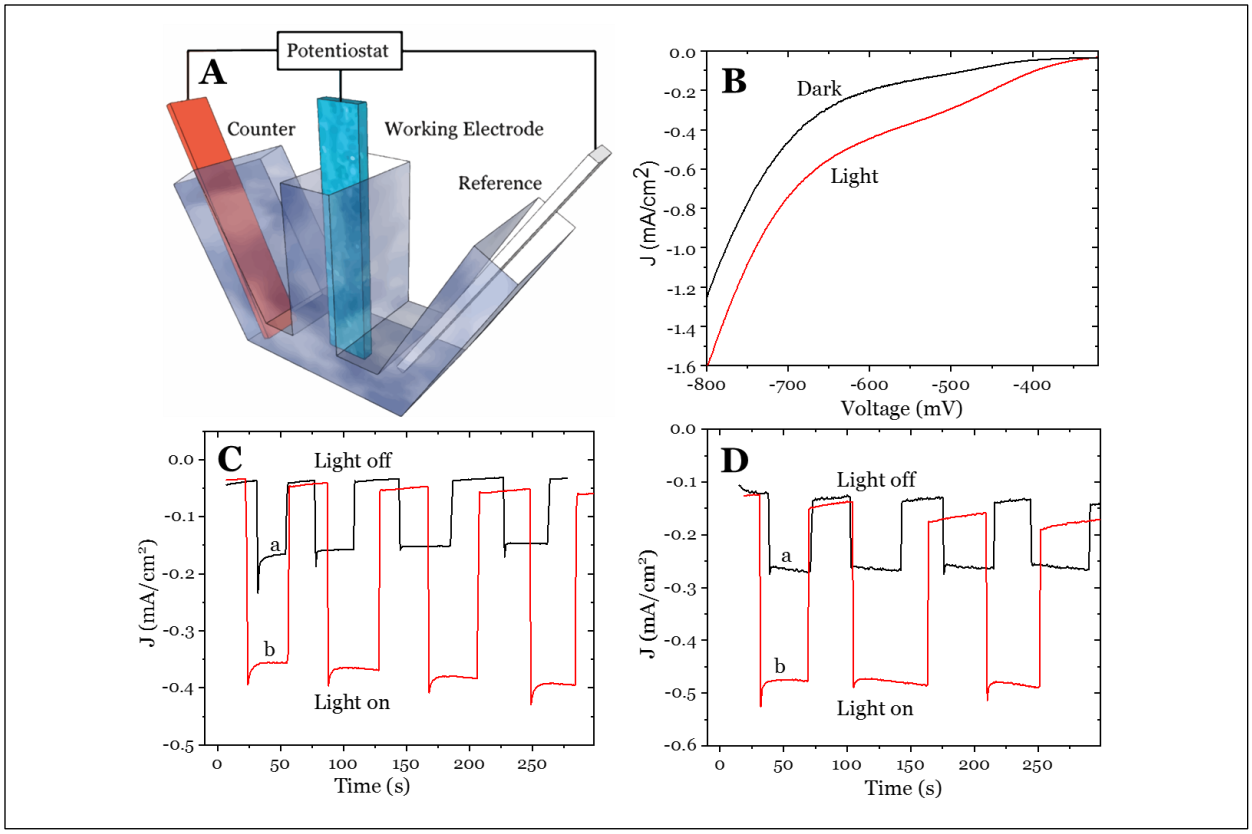

Figure 3-10: (A) Cartoon depiction of three electrode photoelectrochemical cell. (B) Linear sweep voltammetry of CZTS film under dark and illumination depicts expected photocathodic response under AM 1.5 simulated solar flux at 100 mW/cm^2. Current density *vs.* time plot at (C) -500 mV (D) -600 mV for (a) CZTS, (b) K^+-doped CZTS electrode in three electrode cell with reference Ag/AgCl, Pt as counter and 0.1 M $EuCl_3$ in water as redox active electron acceptor.

Figure 3-10B shows a representative LSV response in dark and illuminated conditions of K^+-doped CZTS photocathode. Photocathodic response was observed in both the undoped and K^+-doped CZTS thin films during illumination with AM 1.5 simulated solar flux at 100 mW/cm^2. Dark current in the nanocrystalline photocathode begins to gradually increase from -300 mV until c.a. -700 mV (*vs.* Ag/AgCl), after which a drastic increase in cathodic dark current is observed. We attribute leakage current evident in the dark current scan prior to -700 mV to the high density of defects present without a thermal annealing step. In practice, surface defects in particular populate a significant number of charge carriers at defect sites upon voltage perturbation by the

imposed electric field from the potentiostat. High-energy defect sites on semiconductor NCs can often be catalytic during applied electrochemical bias in dark conditions but is not conducive to efficient charge carrier extraction following photoexcitation.

The stability of the photoresponse for both CZTS and K^+-CZTS photocathodes was probed with chronoamperometry. This allowed us to observe the photocurrent response to intermittent cycling of dark and illuminated conditions as a function of time. The resulting J-t curves at a bias voltage of -500 mV and -600 mV are presented in Figure 3-10C-5D. The results show that both CZTS and K^+-CZTS exhibit stable photoresponse in the aqueous europium redox couple. Significant increases in photocurrent were produced by the K^+-doped CZTS photocathodes, which we attribute to the increase in the excited state lifetime of K^+-doped CZTS NCs that results from the lower degree of phase and surface defects. This increase in excited state lifetime improves the probability of charge extraction and collection at the photocathode contact.

3.4 Summary and Conclusions

The work reported in this work demonstrates, for the first time, the mechanisms involved in the improved performance of K^+-doped CZTS NCs. In summary, K^+-doping leads to a reduction in binary and ternary impurity phases and terminal-surface defects, which are known to reduce charge carrier diffusion length and increase undesirable recombination reactions between electrons and holes. Furthermore, the suppression of these defects leads to a longer-lived photoexcited state as probed by TAS. The improved lifetime of the excited state provides increased probability for charge extraction, leading to the higher photocurrent observed in the photoelectrochemical tests. K^+-doping of CZTS NCs can be achieved directly through the modified hot injection synthesis reported here for the first time. Further work on uncovering the inherent limiting factors in CZTS

NCs can facilitate their introduction to photoelectrochemical reactors for water splitting or in mesoscopic, nanostructured photocathodes for solar energy conversion.

Chapter 4

4 CZTS (Cu_2ZnZnS_4)\Cu_2S electrode for photocatalytic reduction of polysulfide and probing charge injection using transient absorption laser spectroscopy.

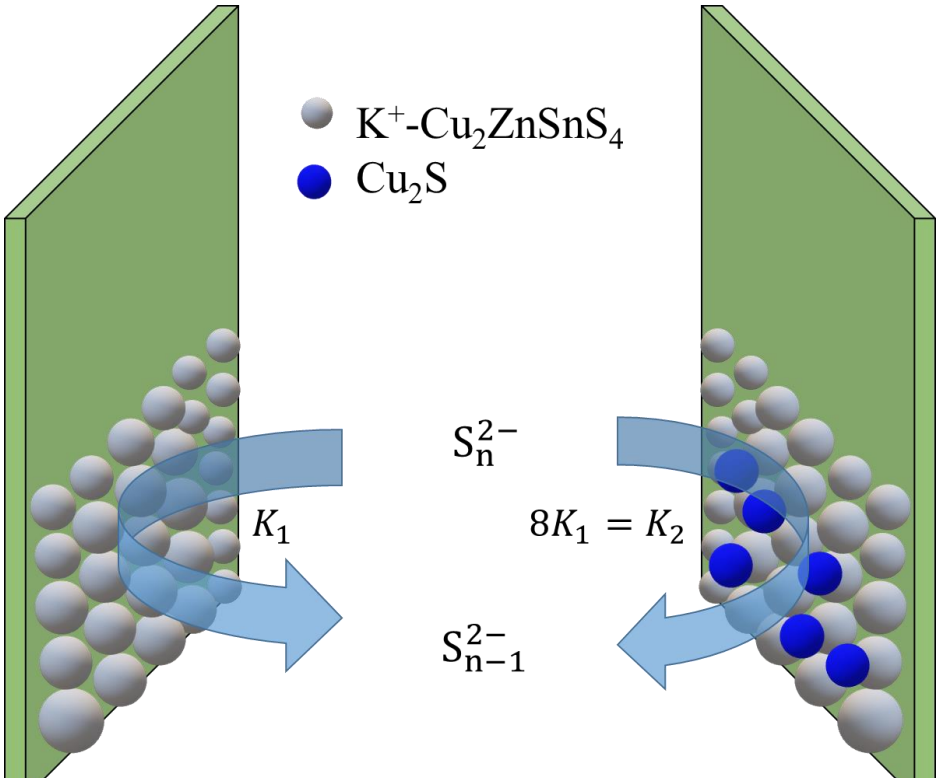

4.1 Introduction

The increased dependency on renewable energy (solar, wind, and hydro) requires large-scale energy storage systems as these source are often intermittent.[45,153] Recently, redox flow batteries (RFB) have captured a lot of attention as evidenced by the exponential number of publications in the field.[40] RFBs have proven to be a viable energy storage technology at an industrial scale in a cost-effective, safe, and efficient environment. Low-temperature operations, large cycle-life, design flexibility, scalability, simplicity, low maintenance costs, and reversible redox reactions are the main advantages of these batteries.[40–45] However, to achieve the target cost of $150 per kWh set by the DOE Office of Electricity Delivery and Energy Reliability, we need a redox couple which is almost free.[46] The polysulfide based RFB (PRFB) utilizes cheap, water soluble sulfur compound which is considered industrial waste from crude oil production. Sulfur can also achieve a very high charge carrier density.[47] A traditional PRFB utilizes an electrical energy source to reduce polysulfide which represents charging of the cell.[42–45] In this report, we investigate photo-assisted reduction of polysulfide utilizing a Cu_2ZnSnS_4 (CZTS) electrode to demonstrate simultaneous solar energy conversion and storage. CZTS is a nontoxic, p-type quaternary semiconductor which is both thermodynamically and economically suited for next generation solar energy conversion technologies. This semiconductor contains earth-abundant elements with a direct band gap energy of ~1.5 eV which is considered optimum for solar absorption.[35,48,93,95,154] There is an abundance of studies on the electrocatalysis of polysulfide for its application in dye-sensitized solar cells (DSSC).[155–160] However, to our knowledge, this is the first ever attempt to evaluate photo-assisted reduction of aqueous polysulfide using a photocathode which presents opportunities for in-situ simultaneous conversion and storage of solar energy, i.e. solar rechargeable batteries.

We developed a CZTS (Cu_2ZnZnS_4) photocathode by spraying CZTS nanocrystals onto preheated FTO and employed the electrode in a three-electrode photoelectrochemical cell with polysulfide as the electrolyte. The electrodes were illuminated with AM 1.5 simulated sunlight with a chopper to disrupt illumination when desired. The electrode performance was measured by the stable photocurrent generated from the polysulfide reduction under solar illumination. The performance of the electrode was significantly improved in multiple steps- by doping of CZTS nanocrystal with K^+ and by using Cu^+ as an electro-catalyst. Electrochemical impedance spectroscopy (EIS), cyclic voltammetry (CV) and Tafel analysis were used to study the charge transfer behavior at the cathode-electrolyte interface. The charge carrier lifetimes of the electrodes were probed using femtosecond transient absorption spectroscopy (TAS) to understand the electron-hole dynamics that fundamentally govern the electrochemical reaction kinetics and the photocurrent.

4.2 Experimental

4.2.1 Chemicals

The following materials were used: copper (II) acetylacetonate, 98+% (Strem Chemicals); zinc acetate anhydrous, 99.98% (Alfa Aesar); tin (IV) chloride pentahydrate, 98% (Strem Chemicals); sulfur powder, -325 mesh, 99.5% (Alfa Aesar); potassium acetate, anhydrous (VWR); disodium sulfide (Anachemia); oleylamine, >50.0% (Tokyo Chemical Industry); formamide, ACS, 99.5+% (Alfa Aesar); chloroform, 99.8+% (EMD Millipore Corporation); ethyl alcohol 190 Proof, 95% (Pharmco-Aaper); copper sulfate anhydrous, 99.98% (Alfa Aesar); sodium thiosulfate anhydrous, 98% (AMRESCO).

4.2.2 Methods

4.2.2.1 CZTS nanocrystal synthesis and electrode preparation

The details for the synthesis and characterization of pristine CZTS and 1.4% K^+ doped CZTS nanocrystals was reported in chapter 3.[68] We adopted a hot injection technique where the metal precursors were mixed with oleylamine (OLA) in a three-neck flask. The degassed S-OLA solution at room temperature was injected into the hot metal precursor solution. The reaction continued for an hour after which the nanocrystal mixture was quenched to room temperature. The nanocrystals were separated and washed multiple times before dispersing into chloroform for storage. The nanocrystals underwent ligand-exchanged reaction with Na_2S to remove long chain surface ligands. After ligand exchange, NCs were washed and dispersed in water. A water methanol dispersion of NC was sprayed onto FTO substrate to complete the electrode fabrication.

4.2.2.2 CZTS\Cu^+ electrode preparation

A single cycle of Cu_2S was incorporated onto CZTS electrode by successive ionic layer adsorption and reaction (SILAR) to avoid excessive corrosion during the electrochemical test. The Cu^+ cationic solution was prepared by adding 40 mg of $CuSO_4$ with 250 mg of $Na_2S_2O_3$ in 10 mL DI water.[145] For a complete cycle, the electrode was immersed in the cationic solution for 30 seconds, rinsed with DI water, immersed in a 0.1 M Na_2S solution for 30 seconds, and then rinsed with water.

4.2.2.3 Polysulfide solution preparation

Polysulfide electrolyte was prepared by sonicating the mixture of 0.7 M Na_2S and 0.07 M S in DI water.[137] The polysulfide solution was degassed by purging N_2 gas before storing in a sealed vial.

4.3 Results and Discussion

4.3.1 Film Characterization

Characterization techniques of the prepared photocathodes are discussed in chapter 3. Here, the UV-vis absorption spectroscopy and Tauc plot for the photocathode are provided in Figure 4-1 confirming a semiconductor band gap of 1.5 eV.

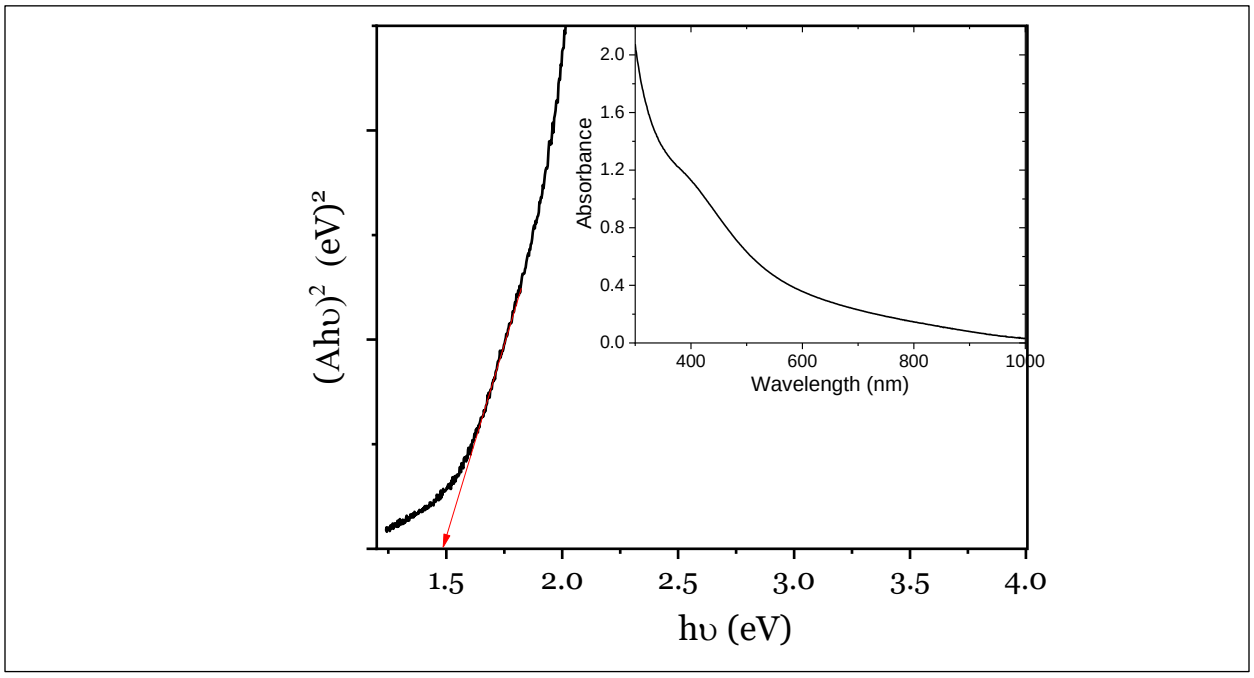

Figure 4-1: Tauc plot for a sprayed K^+-CZTS film showing band gap energy (1.5 eV) of the photocathode, inset UV-vis absorption spectroscopy of the electrode.

4.3.2 Photoelectrochemical performance testing

To investigate electrodes response in photo-assisted reduction of polysulfide, sprayed films were employed as the working electrode in a custom made three-electrode cell as shown in Figure 4-2A. Pt wires were used as the counter and pseudo-reference electrode. The polysulfide solution was continuously sparged with inert gas (N_2) while the data were recorded. The solar spectrum was simulated by using light from a 300 W Xe lamp that was first passed through AM 1.5 filter with 100 mW/cm^2 optical power density. Figure 4-2B depicts the simplified charge transfer mechanism at the electrode-electrolyte interface. The photoexcited electrons reduce polysulfide ($S_n^{2-} \rightarrow S_{n-1}^{2-}$) at the cathode while holes are transported to the counter electrode where they take part in the oxidation reaction ($S_{n-1}^{2-} \rightarrow S_n^{2-}$).

The current density-voltage (J-V) characteristics and stability of the photoresponse were recorded. Figure 4-2C shows a representative linear sweep voltammetry experiment under dark and with illumination. The gradual increase of dark leakage current from -300 mV to -680 mV can be attributed to the high density of defect sites which exist due to a lack of high temperature annealing.[68] These defect sites can accept or donate a significant number of charge carriers under applied electrical bias. A drastic increase beyond -680 mV is accompanied by the H_2 evolution reaction with visual confirmation of gas bubble formation. Under illumination the current density represents the solar energy converted into electrical power which is stored as chemical energy in the electrochemical cell. The direction of photocurrent is expected behavior for p-type semiconductor/polysulfide interfaces where electron injection to the electrolyte reduces polysulfide into shorter chain polysulfide while holes travel towards the counter electrode via an external circuit.

Figure 4-2D compares the photocurrent density of pristine and K^+-doped CZTS electrodes under -600 mV applied bias as a function of time. A stable photocurrent was observed for both electrodes, however, K^+ doping resulted in doubling the photocathodic response. We observed, the similar response for europium redox couple (Eu^{2+}/Eu^{3+}) has been reported in chapter 3 where we showed that K^+ increases the charge carrier lifetime of CZTS nanocrystals by passivating defect sites.[68] Alkali metals such as Na^+ and K^+ have been previously suggested to improve the charge carrier density and enhance carrier separation efficiency.[99–104] This phenomena would result in improved photocathodic response with K^+ doped CZTS electrodes over the pristine CZTS electrodes observed here.

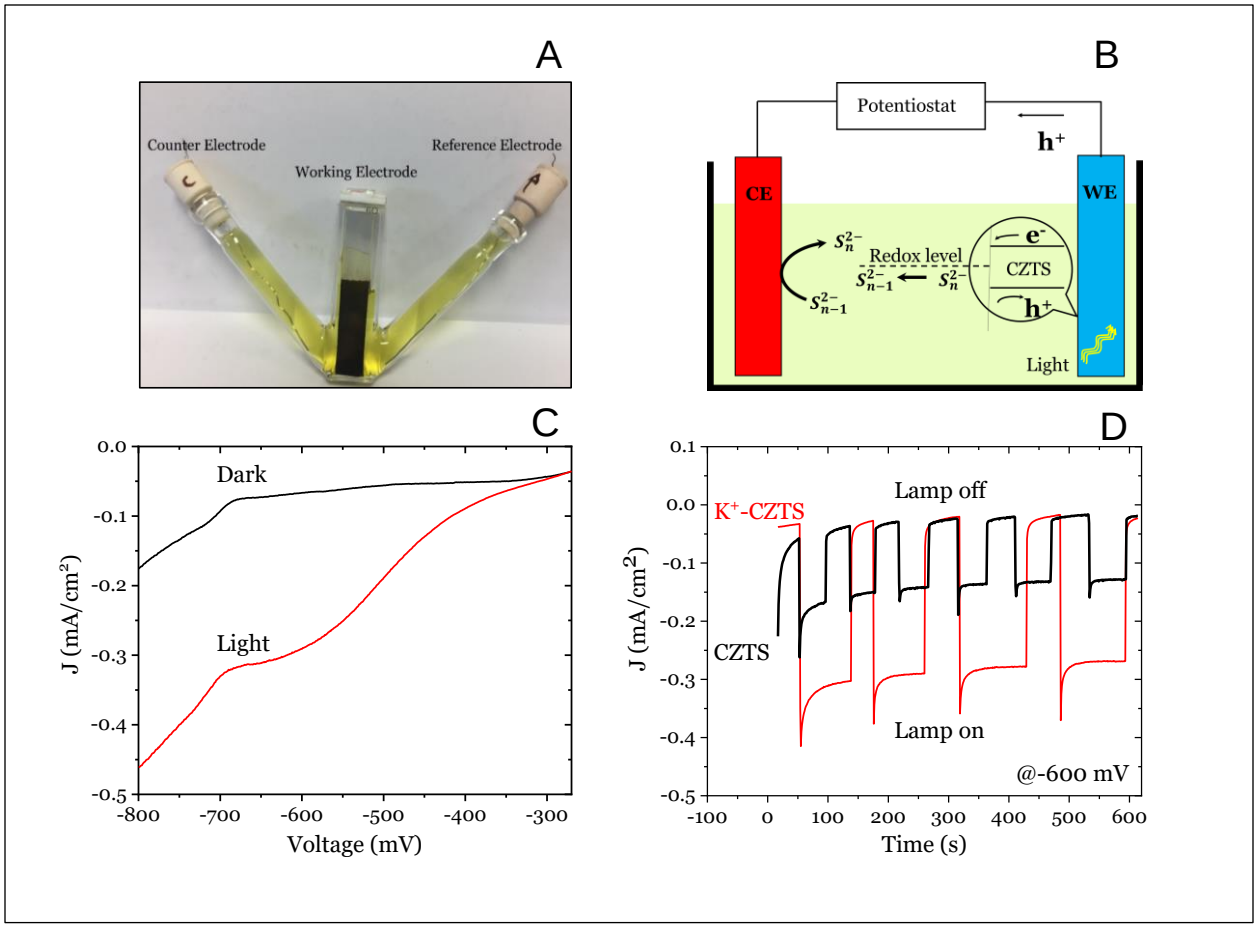

Figure 4-2: (A) Photograph of the custom made three electrode photoelectrochemical cell (PEC) arrangement with polysulfide solution as electrolyte, (B) Cartoon depicts the mechanism for photo-assisted reduction of polysulfide in PEC, (C) Linear sweep voltammetry of K^+-doped CZTS electrode under dark and illumination depicts expected photocathodic response, (D) Current density vs. time plot compares photo-response from (a) CZTS and (b) K^+-doped CZTS electrode at -600 mV applied bias vs reference electrode. The electrochemical response was recorded with AM 1.5 simulated solar flux at 100 mW/cm^2 with Pt serving as pseudo-reference and counter electrode, and aqueous polysulfide (0.7 M Na_2S and 0.07 M S) as redox active electron acceptor.

The effect of electrolyte concentration on the photocathodic response is shown in Figure 4-3. It was observed that the dark current density (trace *c*) and photocurrent density (trace *d*) generated in presence of polysulfide solution is much larger than that from the pure Na_2S solution (trace *a-b*). Addition of S above 0.075 M (Na_2S: S=10:1) results in the dark current to translate without significant contribution to the photocurrent. A similar trend was reported for CdSe/ polysulfide system by Lando et al.[161] It is worth mentioning here that high S concentration in the

polysulfide solution was visually observed to be corrosive towards CZTS film during the PEC experiments when the physical film etches off.

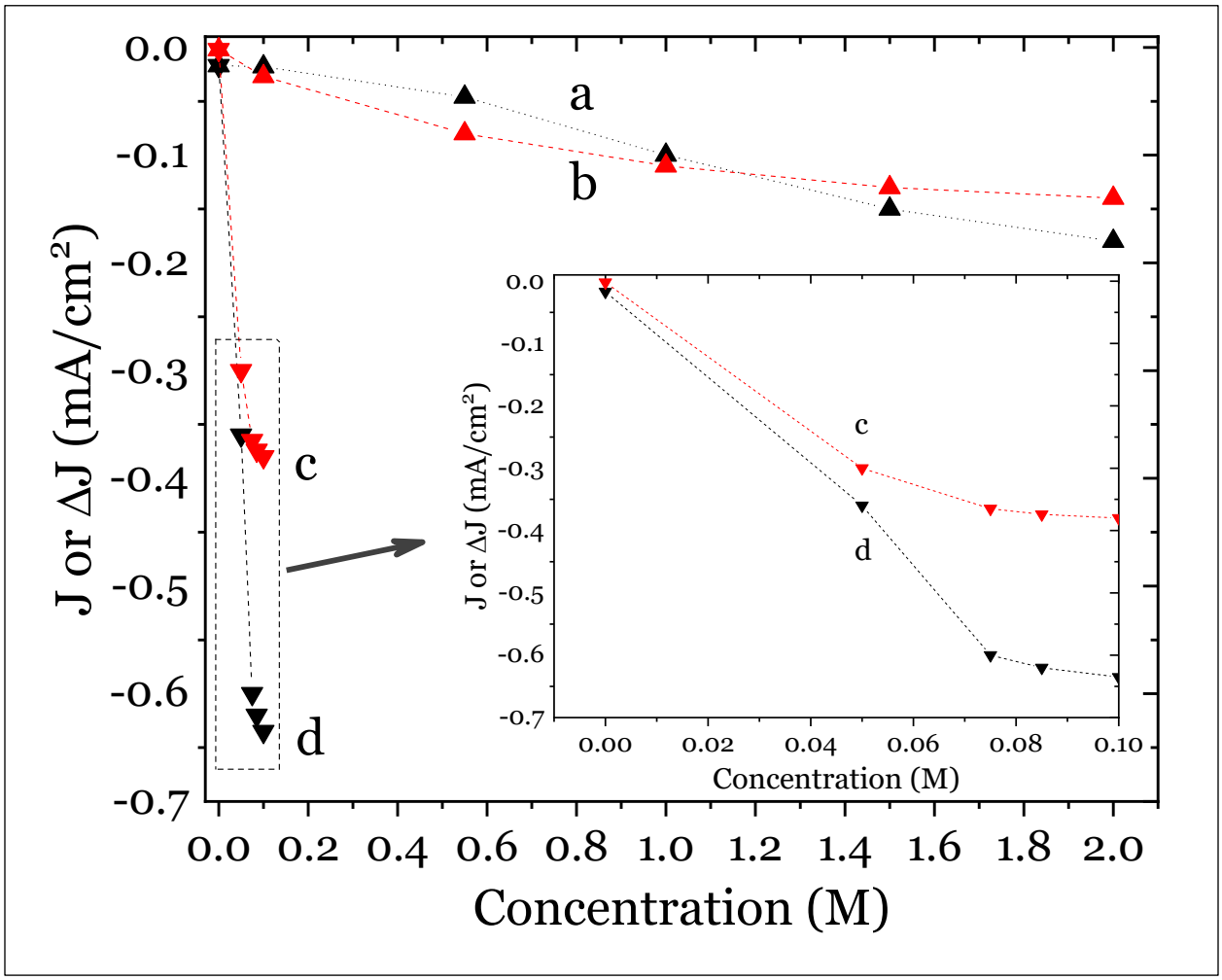

Figure 4-3: In chronoamperometry, (a) dark current density, (b) illumination current density vs. Na_2S concentration; (c) illumination current density, (d) dark current density vs. S concentration in polysulfide solution where S to Na_2S molar ratio was maintained as 1 to 10 ; Higher S concentration was found to be corrosive to CZTS film. The K^+-CZTS electrode was used to measure the current density at -600 mV applied bias against Pt wire pseudo-reference. The photocurrent density (ΔJ) is the difference between illumination and dark current density.

Next, we exploited the electrocatalytic effect of Cu^+ for improving the electrochemical performance of CZTS electrode.[145] We deposited Cu_2S on the K^+-CZTS electrode using SILAR techniques described in section 4.2.2.2. The normalized UV-vis absorption spectra of a thin film

before and after Cu_2S deposition are shown in Figure 4-4. The deviation of the absorbance profile in trace *b* from the trace *a* is due to the presence of Cu_2S on the film.

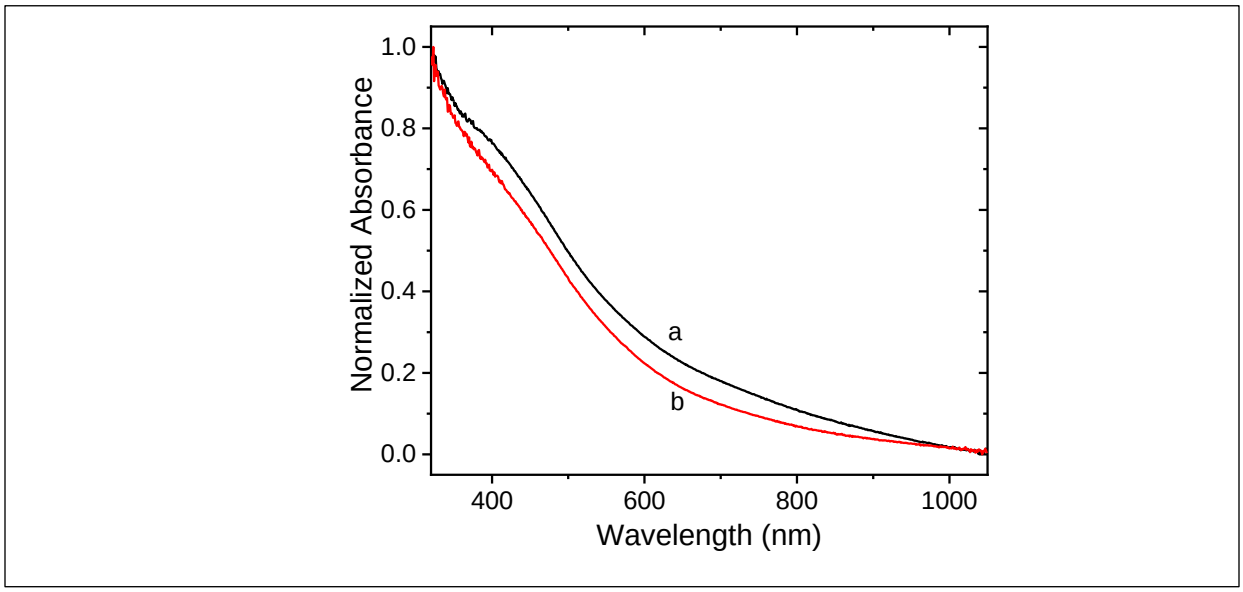

Figure 4-4: Normalized UV-vis absorption spectroscopy of (a) ZrO_2\$K^+$-CZTS and (b) ZrO_2\$K^+$-CZTS\$Cu_2S$ electrode with ZrO_2 baseline.

The photoelectrochemical performance is compared for the electrodes with and without Cu^+ in a PEC cell. Figure 4-5A shows the photocurrent generation under -400mV applied bias as a function of time. With Cu^+, the electrode performance exceeds the original response at a lower applied bias (-100 mV). Cyclic voltammograms (CV) were recorded for K^+-CZTS and K^+-CZTS\$Cu^+$ electrodes in 0.1 M polysulfide solution scanning from -800 mV to 120 mV at a scan rate of 10 mVs^{-1} while repeating the scan for 10 cycles for each electrode (Figure 4-5B). In the resulting voltammogram, the S_n^{2-}/S_{n-1}^{2-} reduction peak was observed near -200 mV vs Pt. pseudo reference. The redox species showed chemical stability and electrochemical reversibility as evidenced by the overlapping cycles and the species remained dissolved in the solution. The CV curve showed a significantly higher electrocatalytic activity with the CZTS\$Cu^+$ electrodes

compared to the CZTS electrodes. To better understand the electrochemical activity, Tafel analysis (Figure 4-5C, Table 4-1) and electrochemical impedance spectroscopy (EIS) measurements (Figure 4-5D) were performed on the electrodes. The improved electrode activity of Cu^+ electrode is confirmed by the Tafel analysis where a higher exchange current density (i_0) is found. The anodic and cathodic current slopes are also doubled in presence of Cu^+ and the transfer coefficient α, which is the weighted average of the slopes, shows that the anodic reaction is equally favorable over the cathodic reaction for both electrodes. The EIS (Figure 4-5D) was recorded in potentiostatic mode at open circuit voltage (V_{OC}) by the pulse of a sinusoidal voltage (10 mV amplitude) with scanning frequency from 1 MHz to 0.01 Hz. We observed Cu^+ causes a dramatic reduction in charge transfer resistance as represented by the arc diameter of the Nyquist plot. The reduced charge transfer resistance is indicative of reduced electrode overpotential for polysulfide redox reactions.[160]

Table 4-1: Tafel analysis data for CZTS vs CZTS\Cu+ electrode in dilute polysulfide solution (0.1 M Na_2S + 0.01 M S)

Electrodes	Exchange current density, (i_0) $(\frac{A}{cm^2})$	Anodic Slope	Cathodic Slope	Anodic transfer coefficient (α_A)	Cathodic transfer coefficient (α_C)
CZTS	2.69616E-08	0.0029	-0.0017	0.62	0.38
CZTS\Cu+	4.66875E-08	0.0059	-0.0034	0.63	0.37
Tafel equation: $logi_x = logi_0 \pm \frac{\alpha_x nF\eta}{2.303RT}$					

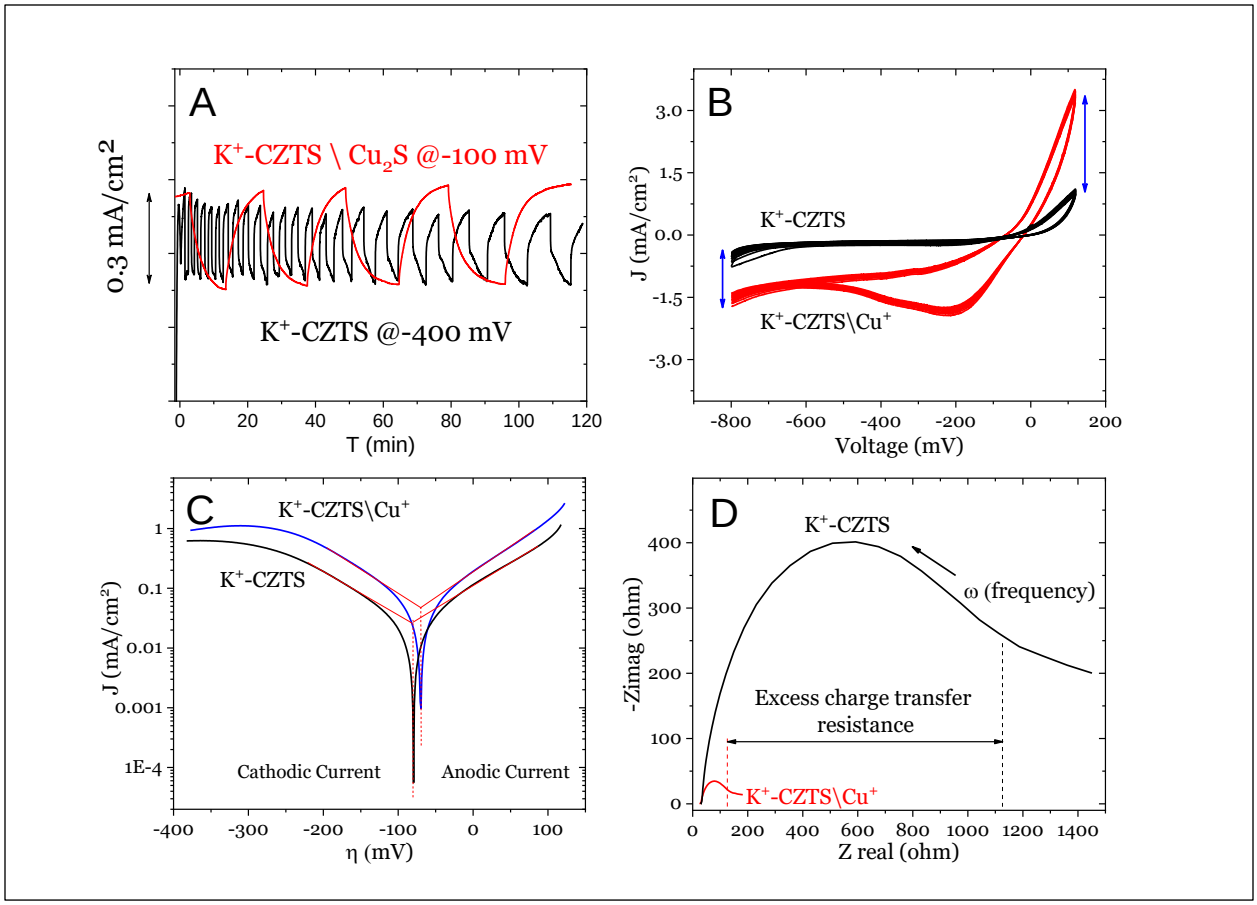

Figure 4-5: (A) Chronoamperometry with polysulfide solution (0.75 M Na_2S and 0.075 M S); (B) Cyclic voltammetry (CV) and (C) Tafel analysis with diluted polysulfide solution (0.1 M Na_2S and 0.01 M S); (D) Electrochemical impedance spectroscopy (EIS) with polysulfide (0.5 M Na_2S and 0.05 M S)

4.3.3 Probing the Excited State of Photocathode

To better understand the reason for improved photocurrent from K^+-CZTS\Cu^+ electrodes compared to K^+-CZTS electrodes, we utilized femtosecond transient absorption spectroscopy (TAS) to probe the photoexcited charge carrier lifetimes. We deposited ligand-exchanged nanocrystals on mesoscopic insulating supports (ZrO_2) via drop-casting to include inter-particle interactions. The films were dried at 130 ^oC in air to increase adhesiveness to the supports followed by Cu_2S deposition as previously discussed. The UV-vis spectra of drop-casted nanocrystal films with and without Cu^+ deposited onto mesoscopic ZrO_2 are provided in Figure 4-4. The films were placed in either $N_{2(g)}$ or 0.1 M polysulfide solution and photoexcited by a 387 nm pump of 130 fs

temporal width. The optical density difference for the probe pulse was recorded between the excited and ground states on the fs-ns timescale[162], $\nabla OD = A_{excited}(t, \lambda) - A_{ground}(\lambda)$. Figure 4-6A shows a typical transient absorption spectrum observed for a CZTS nanocrystal film. A transient bleach at ~500 nm convoluted with excited state absorption was observed which can be attributed to the presence of a 2nd conduction band within the CZTS electronic structure.[17,135,136]

Figure 4-6B (cartoon) shows the primary depopulation mechanisms for the photoexcited charge carriers- (1) charge transfer, (2) charge trapping, and (3) electron-hole recombination (trap mediated). The charge transfer and charge trapping processes are slower relaxation mechanisms compared to the recombination process.[131,163–167] The TAS exponential decay traces in N_2(g) and polysulfide are presented in Figure 4-6C and D respectively while the fitted parameters are compared in Table 4-2

In N_2(g), a significantly faster decay was observed for the K^+-CZTS electrode (τ_{avg} ~1360 ps) relative to the K^+-CZTS\$Cu_2S$ (τ_{avg} ~ 2993 ps). However, the slower components were comparable on both electrodes. The TAS results suggest the predominant role of Cu^+ in improving the carrier lifetime of the electrode is the suppression of the recombination process. By placing the electrodes in polysulfide, we introduce an additional transfer path for the electrons. The effect of electron injection process can be observed from the TAS traces in Figure 4-6D. Both electrodes showed a strong quenching in carrier lifetimes which implied carrier depopulation by charge injection. From the difference in average carrier lifetime ($K_i = \Delta \frac{1}{\tau_i}$), we found that the charge injection rate with a K^+-CZTS\$Cu_2S$ electrode is ~8 times faster than that of a K^+-CZTS electrode. We conclude that Cu_2S suppresses the recombination process which encourages higher electron injection in reducing polysulfide. The higher electron injection rate is reflected by the higher electrocatalytic activity of the electrodes.

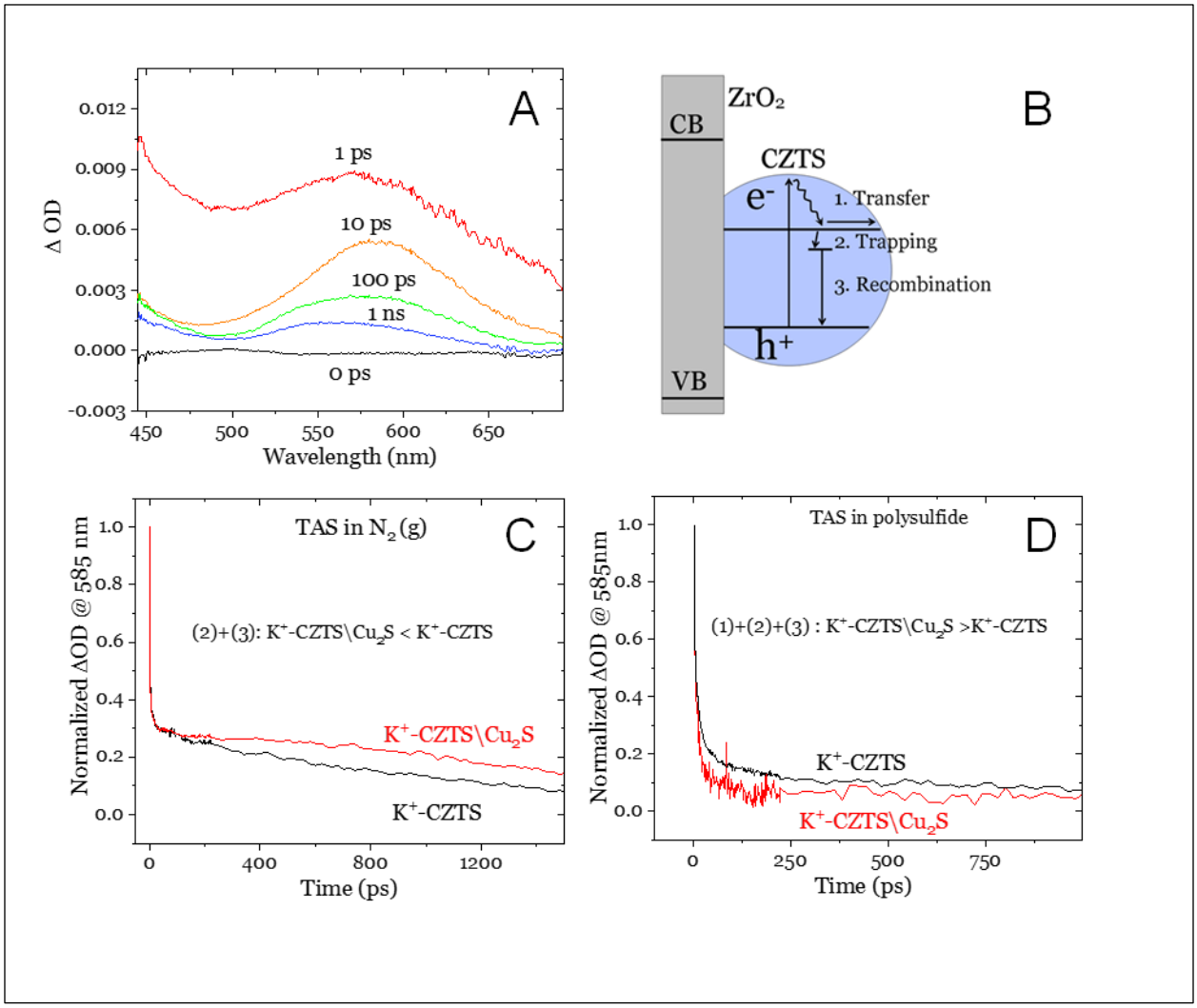

Figure 4-6: (A) Transient absorption spectra of K^+-doped CZTS NC drop-casted onto the mesoscopic ZrO_2 insulating support; (B) Photoexcited carrier relaxation mechanism; Temporal decay of excited state transient absorption in (C) N_2 gas and (D) polysulfide solution; scan settings: 387 nm excitation wavelength, 0.12 mW.

Table 4-2: Transient absorption spectroscopy parameters for CZTS vs CZTS\Cu$^+$ electrode in dilute polysulfide solution (0.1 M Na_2S + 0.01 M S)

Fit Parameters	In N_2		In polysulfide	
	K^+-CZTS	K^+-CZTS\Cu_2S	K^+-CZTS	K^+-CZTS\Cu_2S
A1	1.1 ± .01	1.2 ± .02	1.8 ± 0.17	1.83 ± 0.4
τ_1 (ps)	1.43 ± .04	1.28 ± .03	1.09 ± 0.06	0.84 ± 0.12
A2	0.1 ± .01	0.1 ± .01	0.66 ± .04	0.59 ± .03
τ_2 (ps)	17.5 ± 2.1	16 ± 1.9	15 ± 0.5	9.38 ± 0.86
A3	0.32 ± .003	0.55 ± 0.3	0.14 ± .01	0.1 ± .01
τ_3 (ps)	1371 ± 40	3000 ± 211	215 ± 16	99 ± 15
Lifetime, τ_{avg} (ps)	1360 ± 83	2993 ± 260	171 ± 20	24 ± 8
Injection rate, K_{e^-} (s^{-1})	--	--	5.1×10^9	4.1×10^{10}
$\Delta OD(t)_\lambda = \sum A_i e^{\frac{-t}{\tau_i}}$; $\tau_{avg} = \frac{\sum A_i \tau_i^2}{\sum A_i \tau_i}$				

4.4 Summary

To demonstrate possible application of polysulfide electrolytes in solar rechargeable batteries, we developed Cu_2ZnZnS_4 (CZTS) photocathodes by spray coating CZTS nanocrystals onto preheated FTO substrates and employed these electrodes in a three electrode photoelectrochemical (PEC) cell with polysulfide as the electrolyte. The performance of these electrodes was evaluated in terms of photocurrent generated under applied bias which showed significant improvement when the nanocrystals were doped with K^+. The catalytic effect of Cu_2S was exploited which drastically reduced electrode overpotential and increased photocurrent generation. Electrochemical impedance spectroscopy (EIS) showed the charge transfer resistance reduced dramatically when Cu^+ was utilized. The carrier lifetimes of the electrodes were measured

in polysulfide solutions and in N_2 gas using transient absorption spectroscopy which revealed that Cu^+ passivates surface defects sites and improved the electron injection rate. This surface passivation resulted in higher charge carrier lifetime and an eight times higher electron injection rate which ultimately increased photocurrent generation.

Chapter 5

5 Thioacetamide-enabled Se dissolution in oleylamine for synthesis of CZTSSe nanocrystals

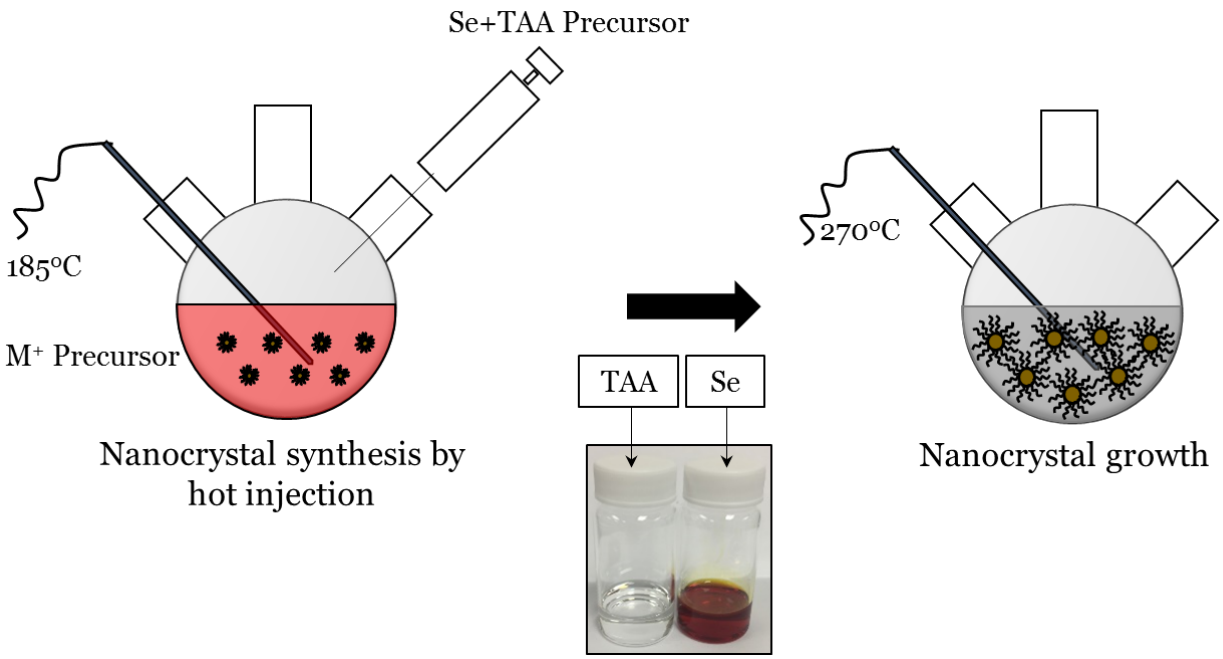

5.1 Introduction

Exploring novel and facile routes to synthesizing low band gap semiconductor nanocrystals has great potential for next-generation solar energy conversion technologies. Earth-abundant, nontoxic $Cu_2ZnSnS_xSe_{4-x}$ (CZTSSe) thin films hold widespread attention because of the optimum direct band gap energy (~1.5 eV) and high absorption coefficient (~10^4 cm^{-1}).[79,99,168] $CZTS_xSe_{4-x}$ ($0 \leq x \leq 4$) shows interesting band gap dependent photoelectrical properties that can be tuned by changing the S/Se ratio.[79,94,148,169–173] The earliest attempts to synthesize CZTSe were based on thermal co-evaporation with elemental metal and Se cracking sources.[174,175] These expensive films suffer from impure binary phases which reduce device performance. The best efficiencies reported with CZTSSe thin films used a selenization technique to tune the band gap energy.[58,176–178] The selenization was achieved by annealing a presynthesized CZTS film under Se vapor at high temperature (~500 ^oC). Such techniques are energy intensive, costly, and offer poor control on the extent of selenization. To achieve finer control Se must be added to the solution prior to CZTS synthesis. Hydrazine based recipes have been shown to produce good quality CZTSSe films with excellent photovoltaic performances.[27,53,168] However, hydrazine is extremely reactive and intensive care has to be taken to avoid any physical contact with its vapor or liquid. Several hydrazine-free synthesis routes have been developed though the options are very limited due to the low solubility of Se in high boiling point organic solvent. Researchers have shown that Se can be reduced by tri-n-octyl phosphine (TOP)/ tributyl phosphine (TBP) at room temperature in presence of OLA.[179,180] The resulting solution is highly reactive and can be used to generate numerous binary, ternary and quaternary NCs. TOP/TBP are hazardous, unstable, and their operations have to be handled in a glovebox, thus people have been searching for phosphine free synthesis routes. Long chain dodecane thiol (DT)/ hexadecane thiol (HT) can be another reducing

agent for Se.[181] Wei et al. showed Se can be reduced with $NaBH_4$ in presence of OLA which was then used for one-pot synthesis of binary metal selenide nanocrystal.[182] Shannon et al. followed the same recipe to produce CZTSSe NCs via hot injection.[148] $NaBH_4$ is a highly corrosive reducing agent and we suspect that CZTSSe nanocrystal prepared through this route will have uncontrolled doping of Na^+ in the crystal lattice.[68,99–102] Surprisingly, there exists a lack of synthesis routes for pristine CZTSSe NCs without using hazardous corrosive chemicals.

Here, we demonstrate a novel, reproducible route for the synthesis of pristine CZTSSe NCs. A homogenous solution of OLA-Se-thioacetamide (TAA) was used as the Se/S source to produce OLA capped NC via hot injection. The band gap of the synthesized CZTSSe NCs can be tuned by changing Se/S ratio in the solution. The NC surface was modified by a ligand exchange reaction with Na_2S-Formamide solution for surface passivation before the NCs were spray deposited onto a preheated FTO glass substrate. The thin films of CZTSSe NCs were employed as photocathode in a polysulfide-based photoelectrochemical cell to investigate the photosensitivity under AM 1.5 simulated sunlight.

5.2 Experimental details

5.2.1 Chemicals

The chemicals used in this experiment are used as received- copper (II) acetylacetonate, 98+% (Strem Chemicals); zinc acetate, anhydrous, 99.98% (Alfa Aesar); tin (IV) chloride pentahydrate, 98% (Strem Chemicals); selenium powder, 99.99% (Strem Chemicals); thioacetamide, ACS, 99% (Alfa Aesar); disodium sulphide (Anachemia); oleylamine, >50.0% (Tokyo Chemical Industry); formamide, ACS, 99.5+% (Alfa Aesar); chloroform, 99.8+% (EMD Millipore Corporation); methanol, 99.9+% (EMD Millipore Corporation); ethyl alcohol 190 Proof, 95% (Pharmco-Aaper).

5.2.2 Nanocrystal Synthesis

For CZTSSe NC synthesis via hot injection, typically copper acetylacetonate (0.935 mmol), zinc acetate (0.7 mmol), and $SnCl_4.5H_2O$ (0.475 mmol) were mixed with 15 mL oleylamine (OLA) in a three-neck flask. The chemical mixture was degassed three times at an elevated temperature (70 ^oC) by alternating vacuum and inert N_2 gas. After degassing the mixture temperature was further raised to 185 ^oC under N_2 gas. The solution looked transparent-orange due to the complete dissolution of all chemicals. At this stage, 5 mL of degassed OLA-thioacetamide (TAA)-Se (1 mmol TAA and 4 mmol Se) solution was injected. The solution turned black immediately due to burst nucleation. The nanocrystal growth continued as the temperature was raised to 270 ^oC and held for 1 hour. At the end of growth process, the heater was removed, and the reacted mixture was quenched to room temperature. For nanocrystals (NCs) separation, 25 mL ethanol was added to 20 mL NC mixture and centrifuged for 10 min at 5000 rpm. The supernatant was discarded, and the NC aggregation was redispersed in 3 mL chloroform by ultra-sonication. The separation process was repeated one more time. The NCs were finally dispersed in chloroform (can be dispersed in toluene as well).

5.2.3 Photocathode Preparation

The NCs went through a ligand exchange reaction before fabricating the photocathode. Ligand exchange reactions were carried with Na_2S-formamide solutions. Typically, 0.453 g of $Na_2S.7H_2O$ was dissolved in 5 mL formamide and mixed with a chloroform dispersion containing 44 mg of CZTSSe NCs. The ligand exchange reaction was carried out in a vial with violent stirring for 6 hours. At the end of the reaction the NCs became dispersed in formamide leaving transparent chloroform at the bottom of the vial. The NCs were separated by adding 5 mL water and 30 mL ethanol followed by centrifugation at 5000 rpm for 5 minutes. The suspended NCs were

redispersed in 3 mL water by ultra-sonication and suspended again by centrifugation after adding 40 mL ethanol. The suspended NCs were redispersed in water and centrifuged to remove the coarse particles. The dispersion was bubbled with N_2 gas before storing in the dark. The dispersion was found stable for months if properly stored. The photocathode was prepared by spraying the water dispersed NC onto FTO glass substrate preheated to 270-300 ^oC. Addition of methanol to the spray dispersion eases the drying process during the spray deposition at relatively lower temperature. Typically, a 1 mg/mL NC dispersion with 80/20 vol% of methanol/water was used for spraying to achieve a homogenous film using a spray pen.

5.2.4 Characterization

The CZTSSe NCs were characterized using X-ray diffraction (XRD; PROTO AXRD, Cu K_α radiation, λ= 1.541 Å, scan settings: 2.72 deg/min, 0.014 deg/step), surface enhanced raman spectroscopy (SERS; Renishaw inVia™ confocal Raman microscope, 532 nm excitation, approximately 2 nm gold islands were formed via sputtering onto CZTSSe film, scan setting: Si peak at 508 cm^{-1}, 5% laser power, 10 s, 20 accumulations), and transmission electron microscope (TEM; Zeiss EM 10). The CZTSSe photocathode was examined under SEM-EDS (Jeol JSM 7000F SEM) and UV-vis absorption spectroscopy (Cary 60 UV-Vis, Agilent). The J-V characteristics were measured in a custom made three-electrode cell at 100 mW/cm^2 using a solar simulator equipped with Xe 150 W light source, a manual chopper, and AM 1.5 filter.

5.3 Results and discussion

5.3.1 Solution chemistry

The oleylamine-thioacetamide-Se precursor solution is vital to the CZTSSe synthesis in this work. The exact chemistry of the precursor solution is difficult to characterize.[172,182] Using UV-vis, we observed that Se replaces S sites in TAA.[183] Figure 5-1 shows UV-vis absorption spectra where trace *a* demonstrates molecular electronic transition in TAA. The C=S bond length (1.60 A^o) is larger than C=Se bond length (1.71 A^o).[184] As a consequence, the corresponding electronic transition energy will be higher in thioacetamide than that in the selenoacetamide. We attribute the absorption edge at ~500 nm to the n-π^* electronic transition (HOMO to LUMO) for the C=S bond.[185,186] The transition energy was red shifted to ~650 nm for the C=Se bond in trace *b*. However, a homogenous solution with Se:TAA molar ratio of 4:1 was achieved which implies that the direct 1:1 substitution couldn't be the only mechanism of Se dissolution. Another possibility is that TAA reduces elemental Se which forms complexes with oleylamine (OLA-Se). A similar mechanism was proposed for reducing agents such as $NaBH_4$ and -thiol by various groups. [148,181]

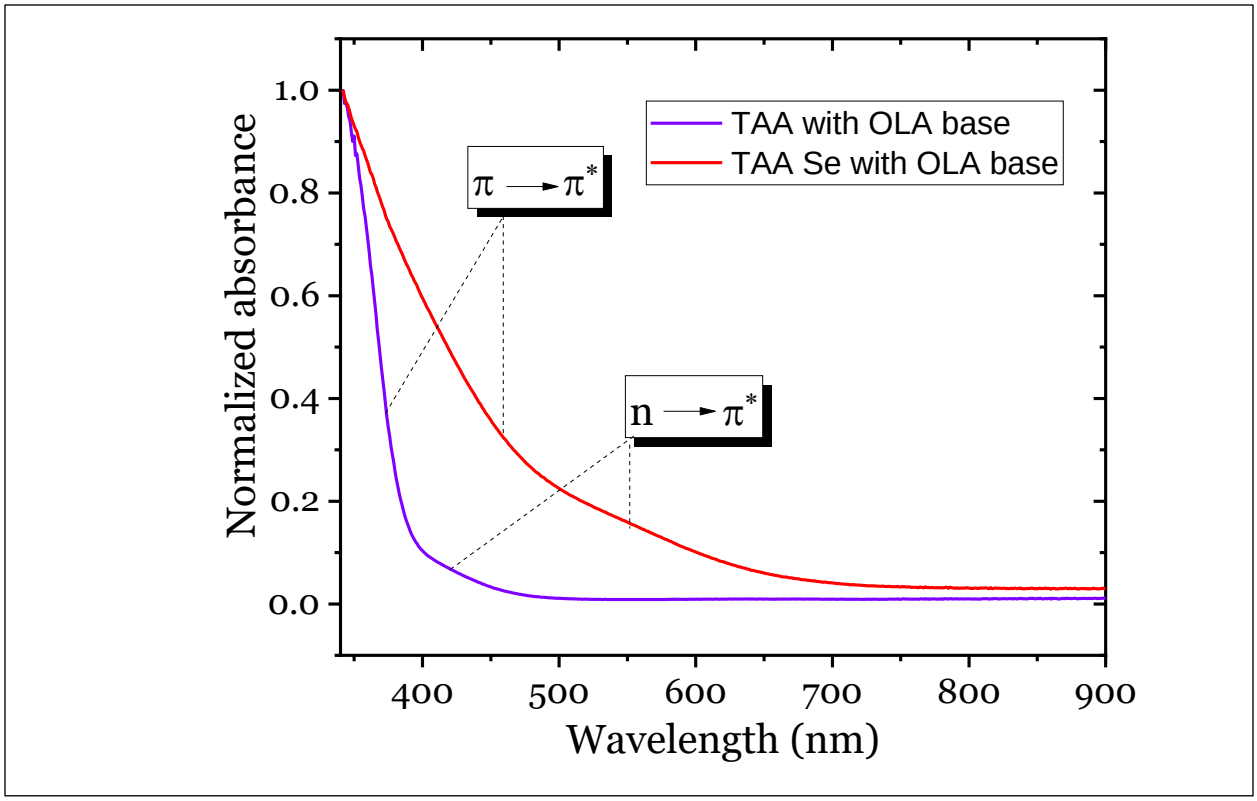

Figure 5-1: UV-vis absorption spectroscopy of TAA vs. TAA+Se homogenous solution in oleylamine.

5.3.2 CZTSSe nanocrystal characterization

The Se to S ratio was varied in the precursor solution and the resulting NC samples are listed on Table-1 and compared using X-ray diffractogram and surface-enhanced raman spectroscopy (SERS). In Figure 5-2A, trace *a* represent the diffractogram of pristine CZTS sample where only TAA was injected (molar Se:S= 0:2). The diffractogram peaks were identified as the kesterite structure of CZTS.[148] Trace *b* shows Se incorporation in the crystal lattice where a precursor with Se:S= 2:1 was injected. The diffractogram peaks shifted to the smaller diffraction angle indicating larger lattice parameters which resulted as the larger Se atoms replaced the smaller S sites (atomic radius, r_S=1.84 A°, r_{Se}=1.98 A°).[99,148] In trace *c*, the highest degree of selenization was achieved by utilizing maximum solubility of Se in TAA (Se:S ~ 4:1). Interestingly, the

diffractogram peaks showed only a slight shift to the lower angle where the higher order planes became more developed. From the FWHM data Table 5-2, it was observed that with increasing Se content the grain size was reduced at the beginning. However, with the highest degree of selenization, the CZTSSe grain size was slightly larger than the pristine CZTS sample. This is in well accordance with the previous observations.[31,32] The most striking distinction between the samples were observed in the SERS (Figure 5-2B). In trace *a*, the pristine CZTS structure can be identified by the strong raman shift at 337 cm^{-1} and two weak shifts at 290 and 372 cm^{-1}.[76] The strong raman peaks for sample b-c shifted to 192 cm^{-1} which is often reported as the raman peak for compositionally pure CZTSe.[99,172,181,189] This indicates faster reaction kinetics for Se in comparison to S as seemingly pure CZTSe resulted despite the presence of S in the reaction mixture. The elemental composition of the CZTSSe NCs was determined using EDS analysis (Figure 5-2B) which agreed with the findings from raman spectroscopy. A Cu poor and Zn rich composition was targeted for the NC samples as that has been suggested for better photoelectric performance.[27,63]

Table 5-1: Chalcogenide ratio in the precursor, EDS compositional analysis, and band gap energy of CZTSSe NCs.

Sample	Injected chalcogenide ratio (TAA:Se), mmol	Molecular Formula determined from EDS composition	Band gap energy (eV)
a	2:0	$Cu_{1.94}Zn_{1.1}Sn_{0.87}S_{4.01}$	1.49
b	1:2	$Cu_{1.79}Zn_{1.1}Sn_{0.9}S_{0.38}Se_{3.8}$	1.46
c	1:4	$Cu_{1.7}Zn_{1.1}Sn_{0.95}S_{0.27}Se_{3.98}$	1.45

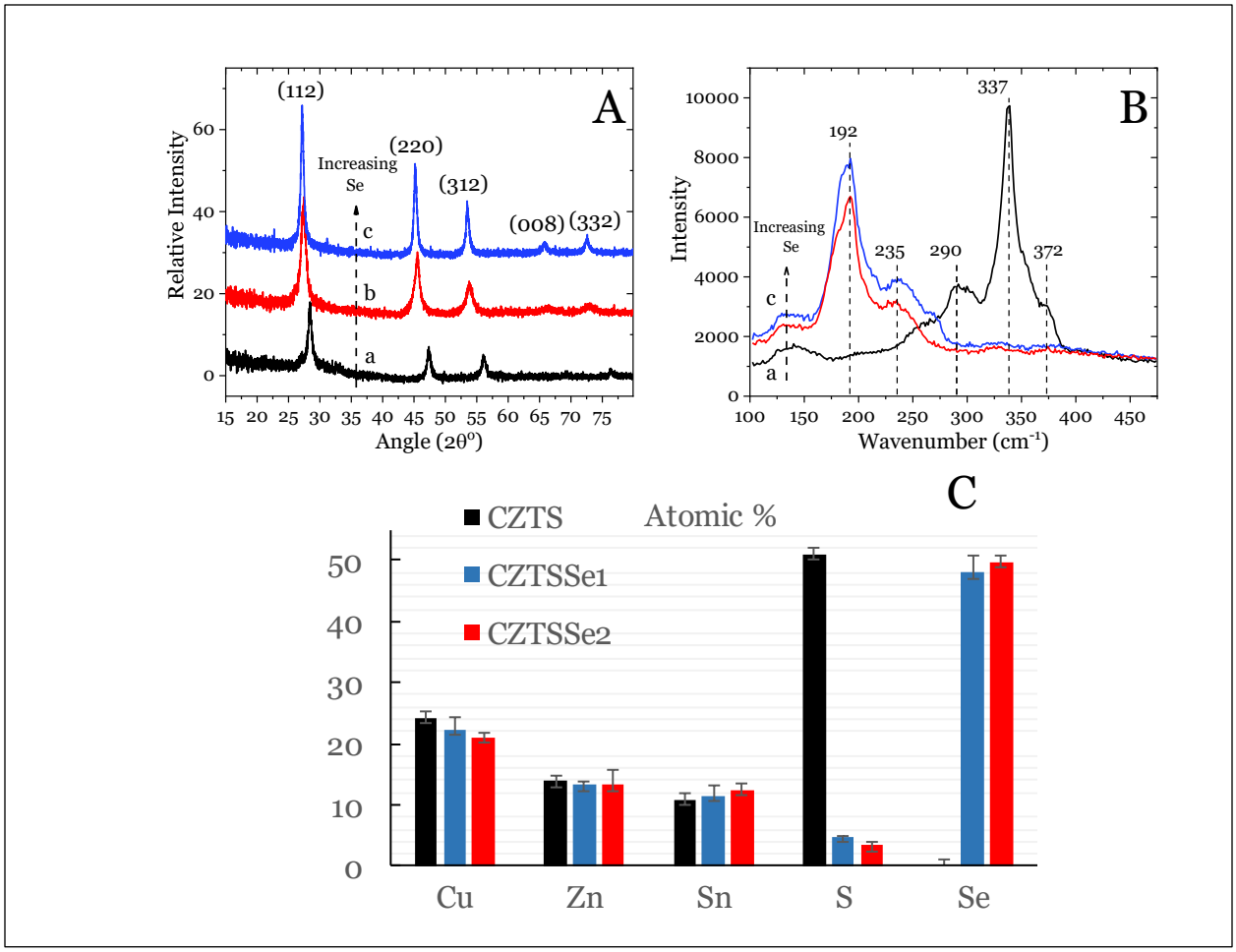

Figure 5-2: (A) X-ray diffractogram and (B) surface enhanced raman spectroscopy (SERS), and (C) EDS compositional analysis of CZTSSe NC aggregated samples when precursor contains S:Se molar ratio (a) 2:0, (b) 1:2, and (c) 1:4.

Table 5-2: FWHM data of the major XRD peaks for CZTSSe nanocrystal aggregated powders with S/Se ratio (a) 2:0, (b) 1:2, and (c) 1:4

	FWHM (degree)		
Planes	A	b	c
(112)	0.56	0.83	0.5
(220)	0.55	0.73	0.49
(312)	0.49	0.79	0.45
(332)	0.06	0.26	0.21

The optical properties of the as synthesized NC were evaluated using UV-vis absorption spectroscopy (Figure 5-3A). From the normalized spectroscopy, we observe an interesting distinction between CZTS and CZTSSe samples. The selenization of NC (sample b-c) minimizes the absorption peak which was prevalent in the CZTS NC (sample a). This absorption peak at ~450 nm had been identified as binary SnS phase in previous reports.[68,82] The $(Ah\upsilon)^2$ vs $h\upsilon$ was plotted to determine the band gap energy by extrapolating the linear region of the plot (Figure 5-3B). Previously, the selenization of CZTS film in Se vapor was reported to generate a large shift (~500 meV) in band gap energy.[50,172] However, a more conservative trend has emerged from the NC studies that show a relatively smaller shift (<70 meV) from selenization.[34,148] We observed that the band gap tuning was not dramatic, a shift of <50 meV was determined for CZTSSe NC. The band gap energies of the NCs (1.49-1.45 eV) were comparable to the experimental bulk values reported for CZTSSe samples.[190–192]

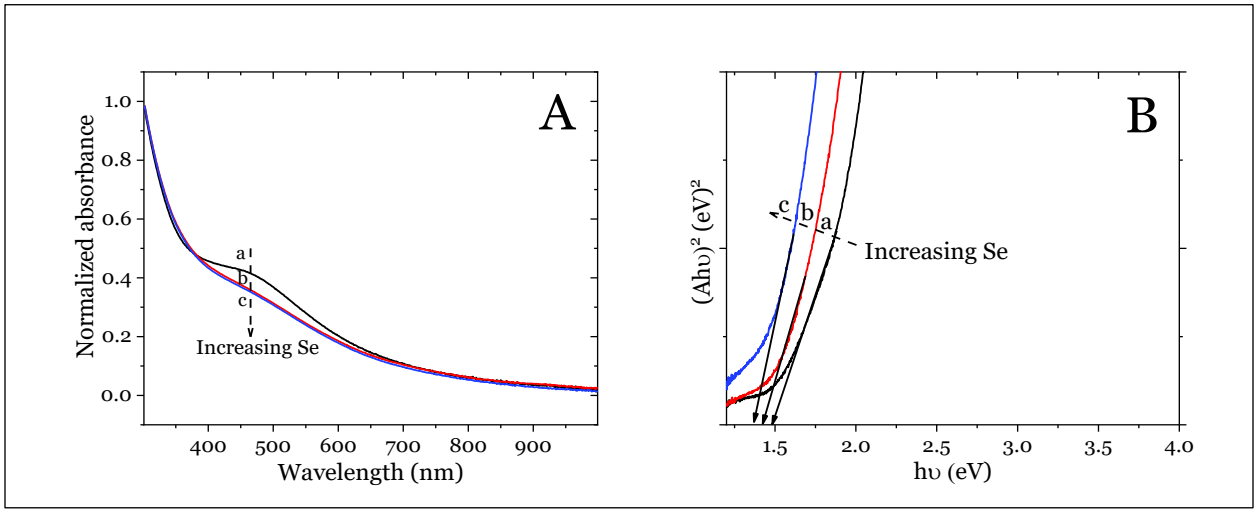

Figure 5-3: (A) Normalized UV-vis absorption spectroscopy showing reduction of binary SnS phase and (B) Tauc plot showing band gap energy tuning with increasing Se content in CZTSSe samples when precursor contains S:Se ratio (a) 2:0, (b) 1:2, and (c) 1:4.

A representative TEM image (Figure 5-4A) of CZTSSe NCs shows the particle dispersity. Figure 5-4B illustrates the size distribution. The particle ranges within ~10-30 nm with an average size (~18 nm) much larger than previously reported data.[148,181] The particle size is controlled by the burst nucleation upon injection of Se precursor solution where the subsequent growth time is same for all nucleates.[117]

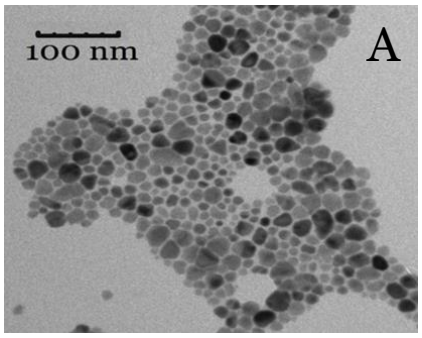

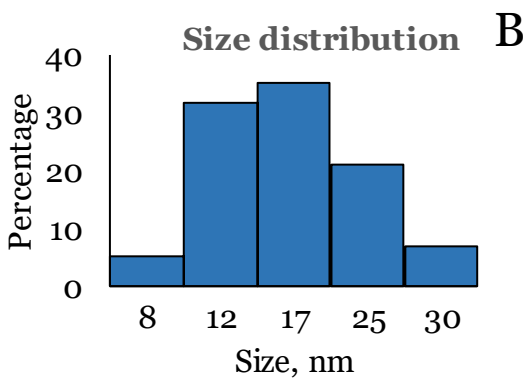

Figure 5-4: (A) TEM image showing dispersity and (B) particle size distribution in the CZTSSe NC sample.

5.3.3 CZTSSe photocathode characterization and electrochemical performance testing

To investigate the photosensitivity, thin films were formed by spray coating as described in the experimental section. Figure 5-5 A-B show the SEM of the resulting morphology and cross-sectional view of the sprayed film. A densely packed film of ~700 nm thickness was used as the working electrode in a three-electrode cell configuration.[68] An aqueous sodium polysulfide solution (0.7 M Na_2S and 0.07 M S) was taken as the electrolyte because polysulfide (S_n^{2-}/S_{n-1}^{2-}) is an important redox couple which finds numerous applications in battery technology.[42,44,45,153] To avoid sulfur poisoning of the traditional secondary reference electrodes, Pt wires were used as the counter and pseudo-reference electrodes. The stability of the current-voltage performance was recorded under chopped white light (flux-100 mW/cm^2) generated by holding the AM1.5 filter in front of a 300W Xe lamp to closely simulate the solar spectrum. Figure 5-5C shows a typical linear

sweep voltammetry response for CZTSSe electrode under dark and illuminated conditions. The reduction peak of polysulfide ($S_n^{2-} \longrightarrow S_{n-1}^{2-}$) was observed near -250 mV with respect to Pt pseudo reference. Beyond -630 mV, the drastic increase in cathodic current was contributed from the water reduction. Under illuminated condition, a more negative current density resulted from photo-assisted reduction of polysulfide at the electrode/electrolyte interface.[68] The stability of the photocurrent was investigated in the J-t plot (Figure 5-5D) with intermittent cycling of dark and illuminated conditions. The photocathodic responses from CZTS and CZTSSe thin films were compared at -500 mV applied bias. The results showed stable photo response in the aqueous polysulfide solution for both CZTS and CZTSSe electrodes. The most prominent feature of the J-t curves was that the photocurrent approximately doubled in the CZTSSe electrode. It is highly unlikely that the slight tuning of band gap energy would result in such drastic improvement. Shannon et al.[148] indicated that the grain boundary passivation by Se-rich surface reduces potential barrier for grain to grain charge transport. In addition, we observed reduced binary phases and increased grain growth in CZTSSe NC which contributed to the improved photocurrent density.

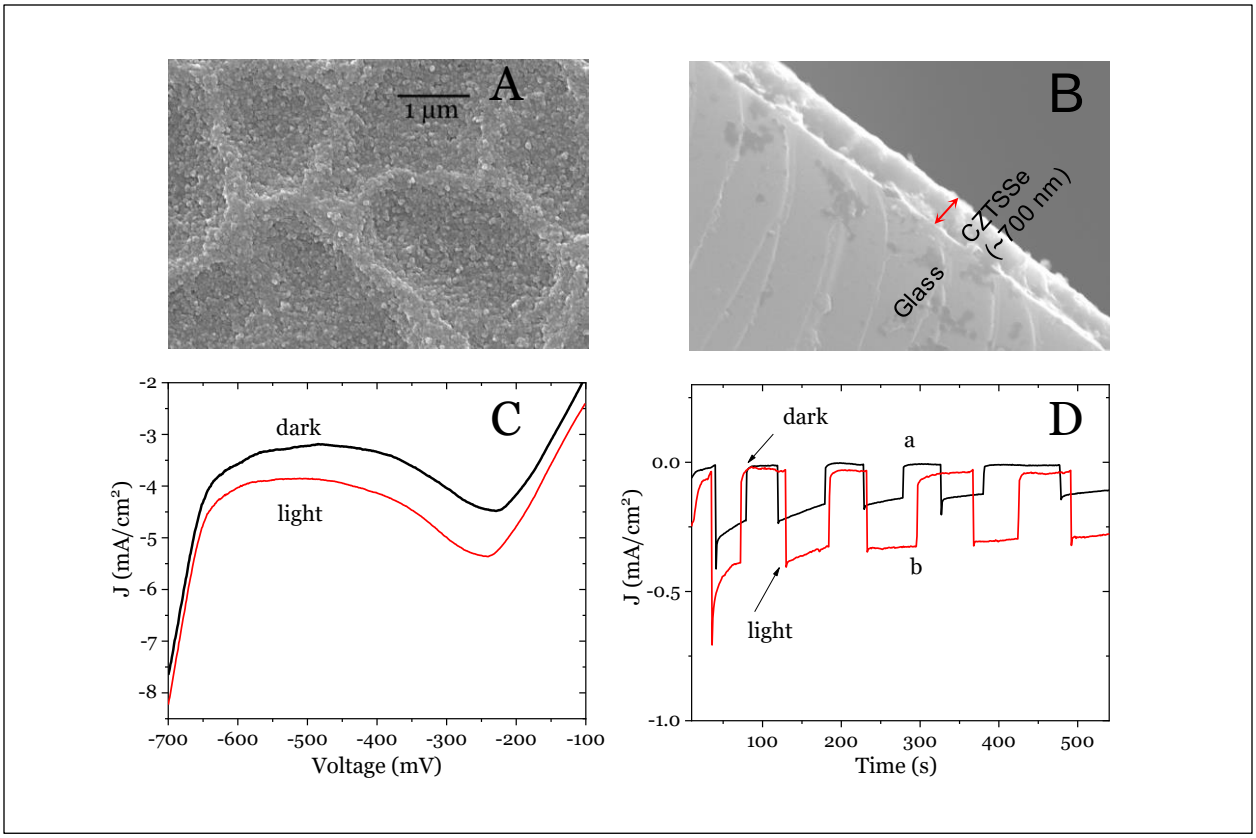

Figure 5-5: (A) Linear sweep voltammetry of CZTSSe photocathode showing cathodic current density with applied bias under dark vs solar irradiation. (B) Chronoamperometry showing stability of photocurrent density with time for (a) CZTS and (b) CZTSSe photocathode. A polysulfide solution with 0.7 M Na2S and 0.07M S in water was taken as the electrolyte solution with Pt wire as pseudo reference electrode.

5.4 Summary

In summary, we present a benign and reproducible procedure for synthesizing CZTSe nanocrystal without using hazardous chemicals like $NaBH_4$ or phosphine. A homogenous solution of oleylamine, selenium, and thioacetamide was used to synthesize close to pure CZTSe nanocrystal via hot injection method. A slight reduction in band gap energy was observed with an increasing degree of selenization. The selenization of CZTS nanocrystal led to larger grain size and reduced binary phase which contributed to a drastic increase in photocurrent generation in a photoelectrochemical cell.

Chapter 6

6 Conclusions and Future Research

6.1 Conclusion

CZTS thin film solar cells holds a great attention in the research of solar energy conversion. The p-type semiconductor is inexpensive, nontoxic with very high absorption coefficient and optimum energy band gap. The pure phase of CZTS forms within only a narrow thermodynamic window and the quaternary compound (CZTS) often coexists with other binary and ternary impure phases. The research presented here is focused on semiconductor liquid junction solar cell following other photo-electrochemical cells such as dye sensitized, and quantum dot sensitized solar cell. The solid-liquid junction cell implies easy fabrication and significant cost reduction compared to the solid-solid junction.

An instantaneous film deposition protocol was developed via spray techniques using a stable and flexible precursor solution. The air stability of the solution was increased by eliminating intermediate chemical reaction within the solution. The precursor solution was spray deposited onto preheated FTO and annealed at 470 ^{o}C under SnS and S atmosphere. Results from Raman studies have indicated minimal presence of impure phases with the film. The precursor solution was used to show binary phase evolution for the first time by probing the UV-vis absorption spectra. By varying the Cu and Sn composition variation, we found that impure SnS_x phase develops under Cu rich and Sn rich condition. To maximize the film performance, a Cu and Sn deficient film was suggested. In a PEC configuration, the photocathodes exhibited stable photocurrent for an extended period of time.

Next, a synthesis protocol for CZTS nanocrystal was established and the mechanisms behind the improved performance in K^+-doped CZTS NCs was revealed. K^+-doping leads to a

reduction in impurity phase and terminal-surface defects which leads to a longer-lived photoexcited state as probed by TAS. The improved lifetime of the excited state provides increased probability for charge extraction, leading to the higher photocurrent observed in the photoelectrochemical tests.

Subsequently, the photocatalytic reduction of polysulfide was demonstrated using CZTS photocathode. The polysulfide reduction represents the charging cycle in polysulfide-based flow batteries. The performance of the electrode was evaluated in terms of photocurrent generated under applied bias which showed significant improvement when the nanocrystals were doped with K^+. The catalytic activity was further improved by using Cu_2S which drastically reduced electrode overpotential and increased photocurrent generation. Probing the carrier lifetimes of the electrodes revealed that Cu^+ passivated surface defects sites and improved electron injection rate. The surface passivation resulted in higher carrier lifetime and eight times higher electron injection rate which ultimately increased photocurrent generation.

Lastly, we presented a benign and reproducible procedure for synthesizing CZTSSe nanocrystal without using hazardous chemical like $NaBH_4$ or phosphine. The bandgap tuning was investigated based on Se composition in the NCs. The selenization of CZTS nanocrystal led to larger grain size and reduced binary phase which contributed to a drastic increase in photocurrent generation in a photoelectrochemical cell.

Researches in the field of CZTS have been proved very fruitful in the past two decades. However, still lots of attention are needed to improve the PCE efficiency to meet the grid parity.

6.2 Future research projects

6.2.1 Incorporation of mesoscopic architecture as hole transporting layer for improved performance

One of the major challenges with the CZTS comes from the mismatch between the thickness required for light absorption and the minority carrier diffusion length. Approximately 1 μm thin CZTS film is required to absorb 95% energy of the incoming light but the minority carrier (electron) diffusion length in this p-type material is only about 200 nm, which is 8 times mismatch.[50] Based on the TAS data, it has been hypothesized that the incorporation of a mesoscopic layer of NiO in between the CZTS and the metal contact will greatly reduce the minority carrier diffusion length and improve the performance of CZTS electrode in liquid junction. The hole transfer capability of NiO was investigated using femtosecond laser spectroscopy. Another study has been proposed to probe the excited state lifetime of the charge carrier as function of nanocrystal size, composition and ligand type. Understanding the charge carrier lifetime of the material will allow finer tuning for reducing the nonradiative recombination rate.

Figure 6-1 shows the diffusion length can be reduced significantly by adopting the mesoscopic architecture. The higher rate of electron extraction should result in improved photovoltaic efficiency. However, the mesoscopic architecture must be chemically stable and must not hinder the hole transportation.

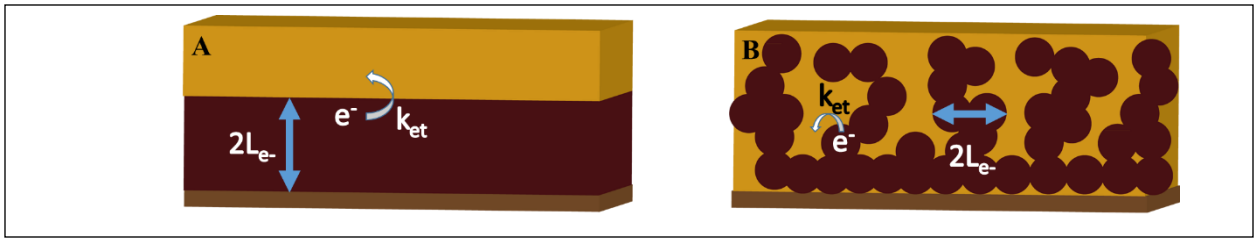

Figure 6-1: (A) Flat architecture vs (B) Mesoscopic architecture (porous three-dimensional network of nanoparticles) of NiO reduces minority carrier diffusion length.

6.2.1.1 NiO as hole transporting layer

The mesoscopic architecture of NiO was evaluated as NiO is a transparent p type semiconductor while the valence band of NiO is appropriately positioned with respect to CZTS valence band (Figure 6-2). The hole transfer capability of mesoscopic NiO was investigated using TAS in the following experiments.

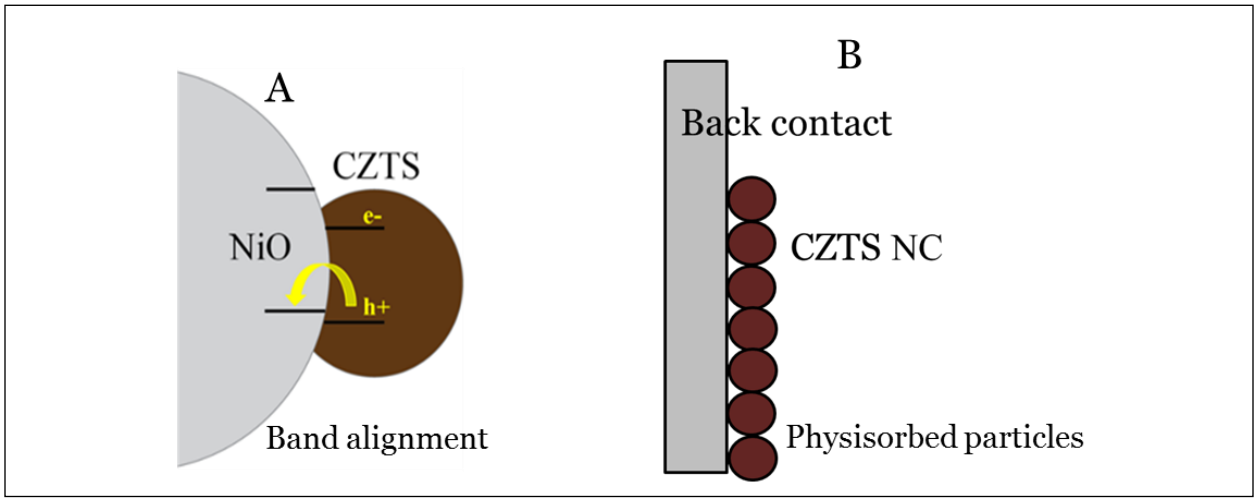

Figure 6-2: (A) Band alignment of CZTS with NiO. (B) Cartoon depicting CZTS NC physisorbed onto hole transporting back contact layer.

6.2.1.2 Experimental

6.2.1.2.1 Mesoporous film fabrication

Mesoscopic NiO layer was prepared by spin coating the NiO paste onto microscope glass slide and subsequently drying the film at high temperature. The NiO paste was prepared by adding 0.45 g NiO powder to a mixture of 1 mL ethanol, 0.1 g terpineol, and 0.03 g cellulose. The mixture was sonicated for 30 min and spin coated onto glass substrate at 1250 rpm for 15 s. The film was then annealed at 500 ^{o}C for 30 min to burn off carbon which leaves a porous architecture. A mesoscopic ZrO_2 film was also prepared by similarly for the control experiment.

6.2.1.2.2 Sample preparation for transient absorption spectroscopy

The TAS samples were prepared by soaking the NiO and ZrO_2 films in CZTS nanocrystal dispersion (10 mg/mL) for 1 hour for physical adsorption. The resulting films were then dried at 130 ^{o}C on air for 10 minutes.

6.2.1.2.3 Electrophoretic deposition of CZTS

For electrophoretic deposition of CZTS NC, the ligand exchanged NC were dispersed in dimethyl-sulfoxide (DMSO) with 10 mg/mL. The dispersion was diluted to .09 mg/mL by adding acetone prior to deposition. As shown in Figure 6-3, a custom-made header was placed on top of a 10 mL beaker which can hold two FTO electrodes submerged in the dispersion and separated by 0.5 mm. A DC potential of 20-40 V was applied across the two electrodes when a current less than 0.6 mA indicating negligible electrolytic breakdown of the dispersion medium. A 10 mL dispersion with acetone:DMSO of 1:120 was used and the deposition was continued for 5-10 minutes. The NCs were deposited on the positive electrode as the particles carried a negative charge. Figure 6-3E shows the zeta potential distribution of the NC dispersed in water. Na_2S treated

NC showed more negative surface charge compared to the sodium polysulfide treated NCs. As a result, Na_2S treated NCs were used in the deposition process which formed a more stable dispersion in the acetone and DMSO mixture. After deposition the electrodes were dried in a furnace tube at 350 ^oC under inert atmosphere for 10 min which removes the residual solvent from the films and improve adhesion to the porous support.

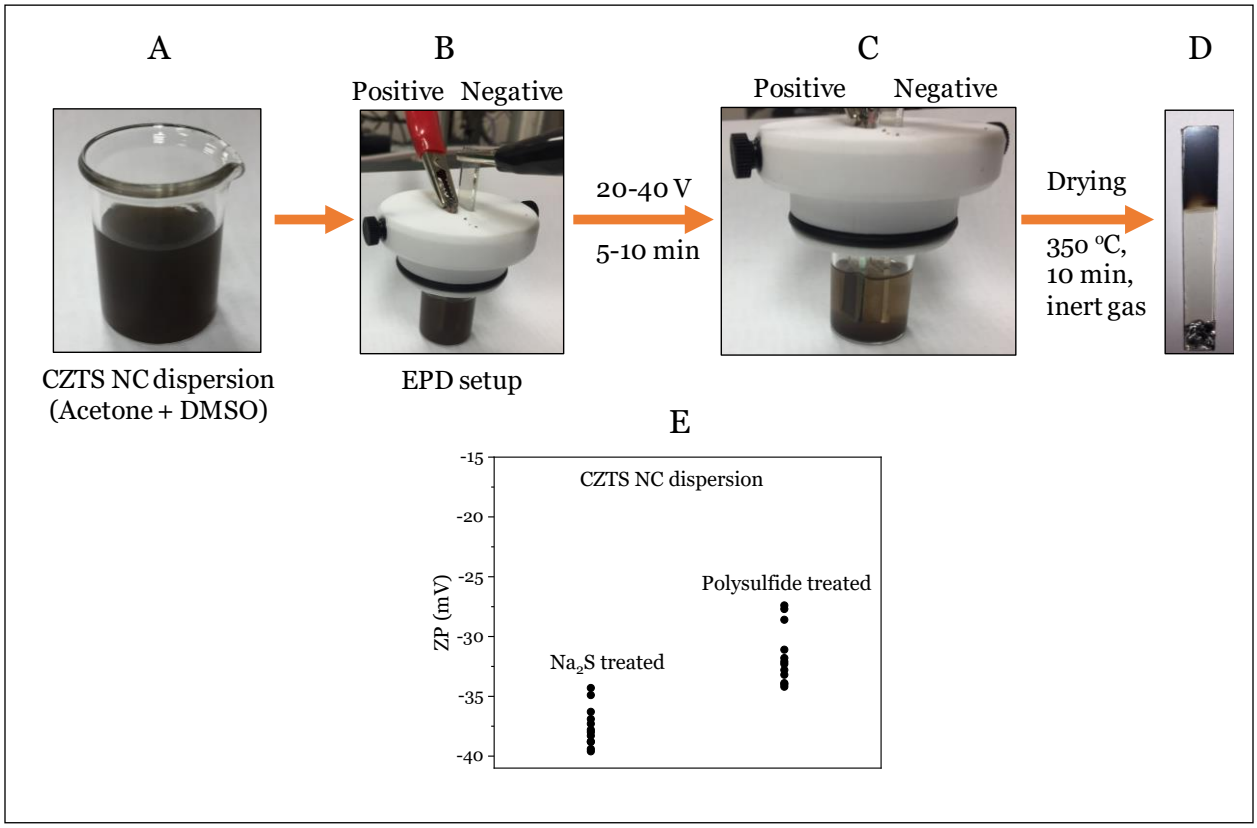

Figure 6-3: (A) Dispersion of CZTS NC in acetone and dimethyl-sulfoxide mixtures. (B) Electrophoretic deposition setup shows the custom-made arrangement of a header that can hold the electrodes submerged and separated by 0.5 mm. (C) Replenishing dispersion as the deposition progresses. (D) A film of CZTS NC electrophoretically deposited onto porous NiO support. (E) Zeta potential measurement of a CZTS NC dispersion in distilled water (pH~ 6.0) showing the Na_2S treated NCs had higher surface charge than sodium polysulfide treated NCs.

6.2.1.3 Probing hole transfer kinetics using transient absorption spectroscopy.

To study the hole transfer kinetics, the carrier lifetime of the CZTS NC was probed using transient absorption spectroscopy. Figure 6-4A shows faster decay of the transient absorption signal when CZTS was interfaced with mesoscopic NiO compared to ZrO_2. The additional transfer process from the CZTS NC to the NiO layer resulted in quenching of the signal while low valence band edge of insulating ZrO_2 prevents any charge transport. The carrier transfer rate is inverse of carrier lifetime which is linear combination of the constituent rate constants from processes such as radiative recombination, nonradiative recombination and charge transfer.[38]

$$\tau_{NiO} = \frac{1}{K_{nr}+K_{ht}} \quad (1)$$

$$\tau_{ZrO_2} = \frac{1}{K_{nr}} \quad (2)$$

$$K_{ht} = \frac{1}{\tau_{NiO}} - \frac{1}{\tau_{ZrO_2}} \quad (3)$$

Here, K_{nr} is the nonradiative recombination rate constant and K_{ht} is the hole transfer rate constant. It is assumed that hole transfer to NiO is the only difference between the two systems. Using equation (1) through (3), the K_{ht} was determined as 8.0×10^{11} s^{-1} (approx.). To crosscheck our assumption that the TAS signal correspond to the hole transfer, we introduced isopropanol as electron donor to CZTS colloidal dispersion since the HOMO of the isopropanol is above the valence band energy of CZTS and the LUMO is far above the conduction band (Figure 3-9B). The TAS data presented in Figure 6-4B shows faster decay when hole-scavenging isopropanol is present which implies the transient absorption is related to trapped holes on the sulfur ions present on the CZTS NC surface.

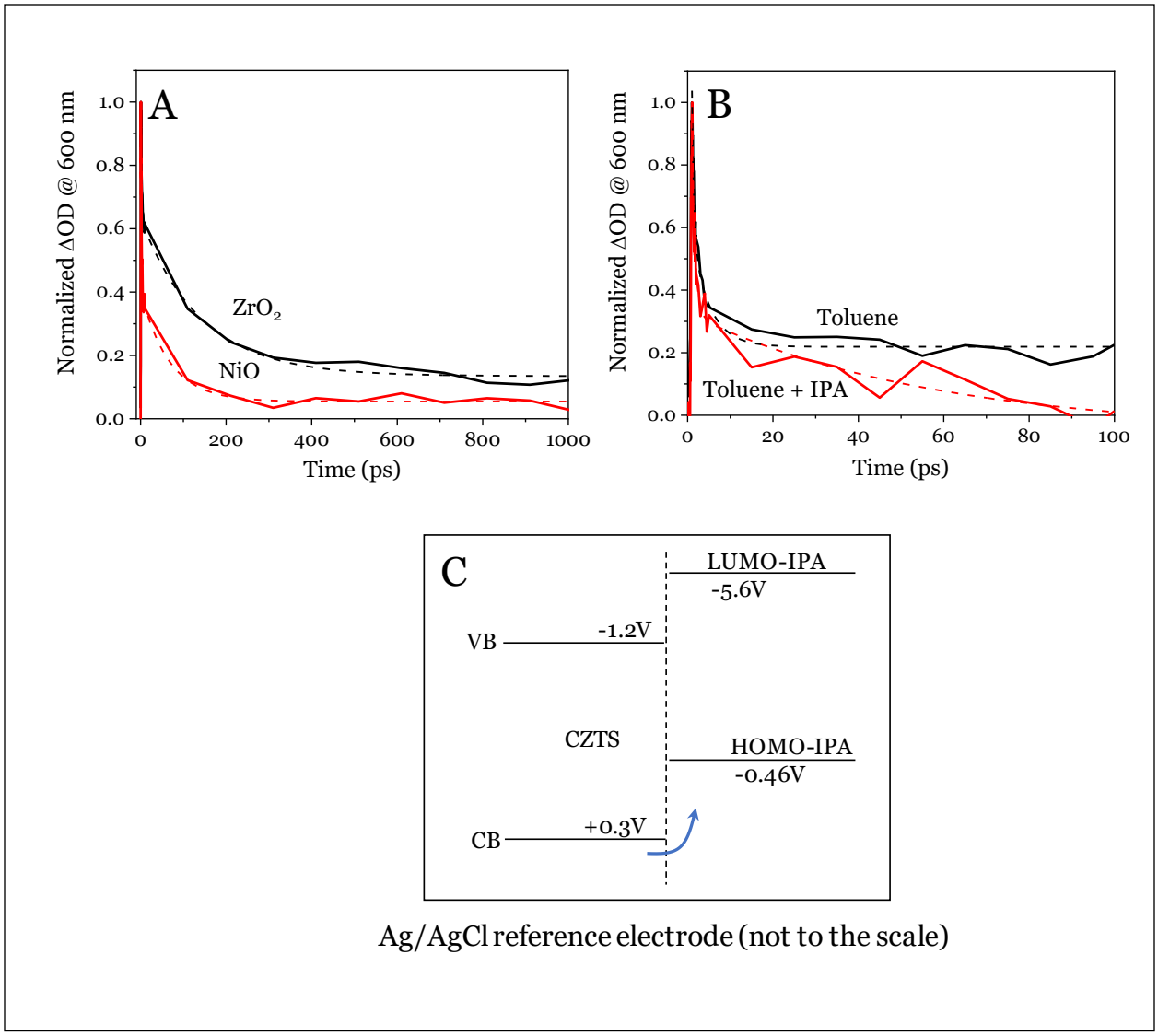

Figure 6-4: (A) Decay of transient absorption spectra at 600 nm with NiO and ZrO_2 support. NiO support showing quenching of the hole signal compared to the ZrO_2 insulator. (B) Decay of transient absorption at 600 nm in toluene and in 2:1 toluene-isopropanol solvent. The faster decay in the transient absorption is related to the introduction of electron donor to scavenge photogenerated holes and establish the origin of the transient signal. The rate constant for hole transfer is on the order of 109 s-1, which would be expected for an upper bound transfer rate in a diffusion-controlled system. (C) Band gap alignment of CZTS and HOMO and LUMO energy level of isopropanol with respect to Ag/AgCl reference electrode.

6.2.1.4 Characterization and performance testing.

The uv-vis absorption spectroscopy of the NiO and CZTS NC deposited films is shown in Figure 6-5A. The porous NiO film showed a sharp absorption edge at 320 nm which corresponds

to a band gap of 3.8 eV.[193,194] The absorption spectra of the EP deposited CZTS NC is shown with the NiO baseline. The absorbance reduced after heat treatment indicating removal of residual solvent from the film. Figure 6-5B shows the stylus profilometry of the NiO film. A NiO: ethanol ratio of 0.45:1 yielded a porous film with average thickness of 104 nm. The film showed high surface roughness as measured by the arithmetic and rms value (R_a = 126 nm, R_q = 250 nm). The SEM image of the NiO\CZTS film shows cracks and crest as expected in a mesoporous support. The electrochemical performance of the film is presented by the chronoamperometry data under dark and illuminated condition. A three electrode photoelectrochemical cell was used where the NiO\CZTS film was illuminated by simulated solar radiation. A 0.7 M sodium polysulfide solution in water was used as the electrolyte solution. A significant photocurrent of 0.25 mA/cm^2 was achieved from the electrode.

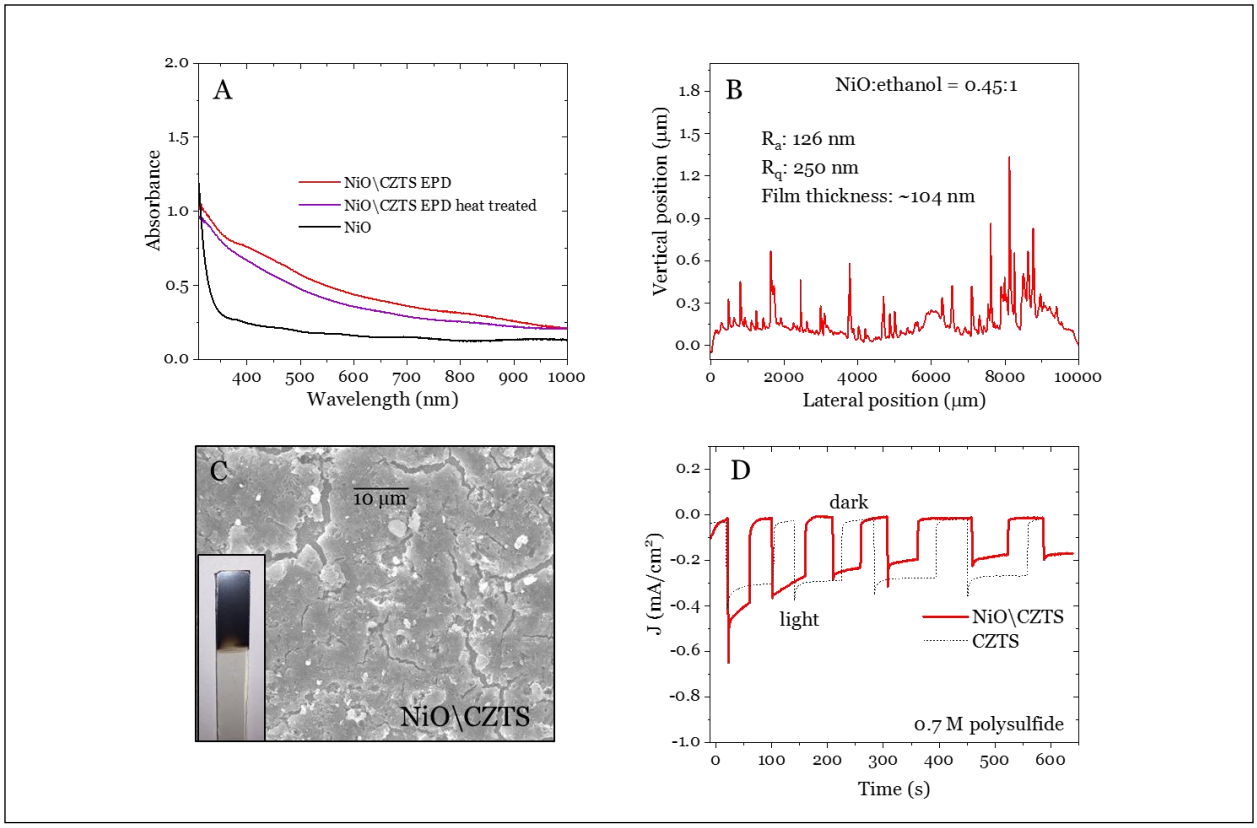

Figure 6-5: (A) UV-vis absorption spectroscopy of porous NiO, NiO\CZTS EPD film before and after heat treatment. (B) Stylus profilometry of a NiO porous film. (C) SEM image of NiO\ CZTS EPD film. (D) Chronoamperometry for the NiO\CZTS photocathode under dark and illuminated condition with 0.7M sodium polysulfide electrolyte at -500 mV applied bias with respect to Pt pseudo-reference electrode.

6.2.1.5 Optimization and future direction.

The photocurrent achieved in the experiment didn't supersede the photocurrent generated from the sprayed CZTS NC electrode onto bare FTO substrate. However, the preliminary data showed promises for further improving the electrode performance through optimization of the design parameters. In the NiO paste, the NiO: ethanol ratio determines the film thickness which is one of the most important parameters in the design of mesoscopic architecture. In our rudimentary investigation, we found that a film with 0.45:1 ratio (NiO: ethanol) performed better than the film with 0.65:1 ratio. Another important parameter would be the carbon content in the NiO paste which controls the porous architecture in the film.

The electrophoretic deposition parameters also play a critical role in the film structure and film quality. The electrical field is affected by the applied voltage when the distance between the electrodes is fixed. A weaker electric field results in slower deposition rate and affects the adhesion of CZTS NC to the porous support. We found that films deposited at 40 V performed better than films deposited at 20 V. This is perhaps because with higher electrical field strength the CZTS NC can be forced to reach the pores that was unavailable at lower voltage. However, the dispersion concentration must be kept low ($\leq$0. 09 mg/mL) as the particle aggregated near the electrode tend to stick to one another and create a non-adhesive superficial layer on top of the porous support.

The post deposition heat treatment removes the residual solvent within the film and improve the contact between the NiO support and the CZTS NC. A combination of time and temperature should be selected that minimizes the charge transfer resistance at the NiO-CZTS NC interface.

Mo can be used as an alternative to NiO, as it is commonly known as hole accepting, back contact in CZTS photovoltaics.[178,195–197] However, the Mo\CZTS contact has poor adhesion and it is chemically unstable, giving rise to MoS_2, Cu_2S, SnS at the interface when depositing the precursor elements.[195] Cu_2S causes short circuit as the resistance of this material is extremely low. MoS_2 gives better adhesion but it has low conductivity which increases the series resistance. Hence minimizing the MoS_2 layer thickness is extremely important. An intermediate buffer layer of Ag, TiN, ZnO, TiB_2, or SnS has been found to control the MoS_2 thickness in numerous studies .[178,195–197] Annealing of Mo in N_2 atmosphere also helps to reduce the MoS_2 thickness. However, CZTS nanocrystal doesn't necessarily need high temperature annealing in sulfur atmosphere, thus the problem of MoS_2 formation is less concerned with nanocrystal-based electrode. The mesoscopic

architecture of Mo can be obtained by controlled sputtering of Mo on mesoscopic ZrO_2 or SiO_2 layer.

6.2.2 Fabrication of solar rechargeable redox flow battery system

The photocatalytic reduction of polysulfide was presented in chapter 4 which presents opportunity to utilize a CZTS photocathode in a polysulfide based solar rechargeable redox flow battery.

Figure 6-6A demonstrates the role of a CZTS photocathode in a traditional polysulfide-iodide redox flow battery (PRFB) with the following configuration - Photosensitive semiconducting electrode | Electrolyte$_1$ (Na_2S_2/Na_2S_4) || Electrolyte$_2$ (NaI/NaI_3) | Counter electrode.

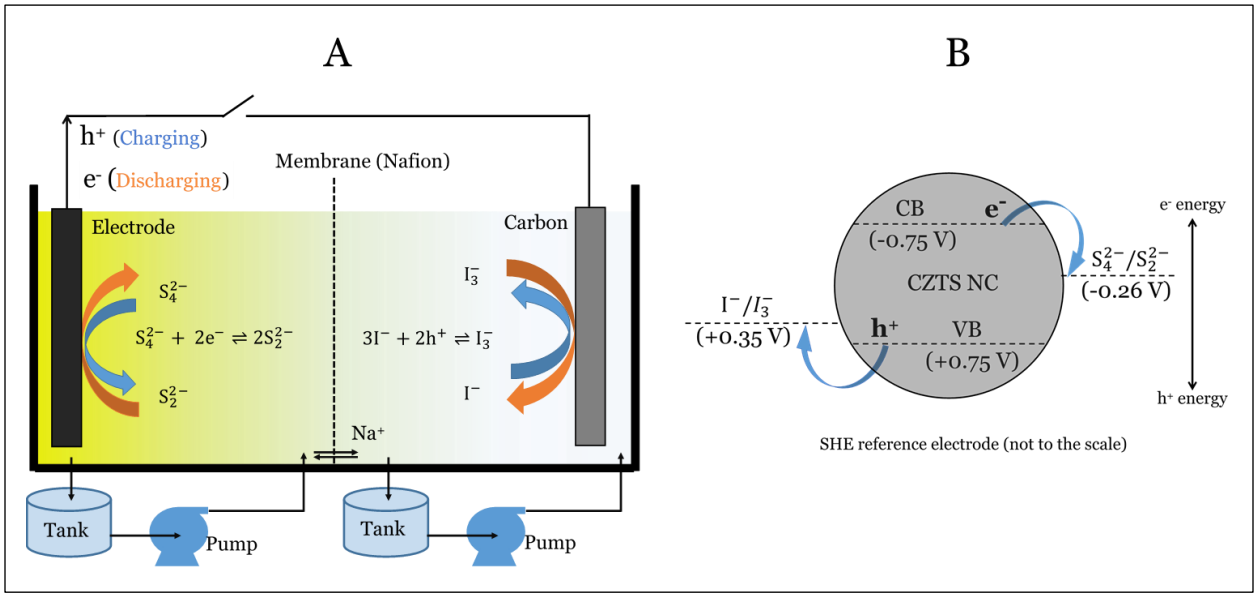

Figure 6-6: (A) Polysulfide-iodide based redox flow battery. (B) Charge transfer mechanism from CZTS nanocrystal to the redox species.

The special features of the RFB is that the energy storing electrolytes are not kept in the battery chambers. Two outside reservoirs hold the anolyte and catholyte separately. Each

electrolyte circulates from reservoir to electrode chamber in a loop. Each electrolyte contains a redox couple and the difference between the two redox levels contributes to the cell voltage. The electrolytes are separated by ion exchange membrane (e.g. Nafion) which selectively allows Na^+ ions to pass in order to balance the positive ions. The chemical reactions are as follows where the forward reactions represent the charging of the cell and the backward reactions represent the discharging cycle.[43]

$$S_4^{2-} + 2e^- \rightleftharpoons 2S_2^{2-}$$

$$3I^- + 2h^+ \rightleftharpoons I_3^-$$

In a traditional RFB, an electrical energy source drives the charging reaction of the cell. In the proposed system, the electrical energy source is reinforced by the solar energy which is absorbed at the CZTS photocathode. The relative energy band position of CZTS with respect to S_4^{2-}/S_2^{2-} and I^-/I_3^- is portrayed in

Figure 6-6B, the CB of CZTS is more negative than the standard redox potential of S_4^{2-}/S_2^{2-} and VB of CZTS (+0.75 V) is more positive than the standard redox potential of I^-/I_3^- (+0.35 V) with respect to NHE.[45,198,199] The photogenerated electron reduces the polysulfide and holes are transferred to the counter electrode where they oxidize the I^-. The photo generated charge carriers driving the reduction at cathode and oxidation at anode reinforces the charging of the cell which can be achieved through simultaneous conversion and storage of solar energy.

References

(1) Grätzel, M. Photoelectrochemical Cells. *Nature* **2001**, *414* (6861), 338–344.
(2) Holgate, S. A. *Understanding Solid State Physics*; CRC Press, 2009.
(3) Pundsack, T. J.; Chernomordik, B. D.; Béland, A. E.; Aydil, E. S.; Blank, D. A. Excited-State Dynamics in CZTS Nanocrystals. *J. Phys. Chem. Lett.* **2013**, *4* (16), 2711–2714.
(4) Ito, K. Copper Zinc Tin Sulphide-Based Thin Film Solar Cells; Wiley, 2015.
(5) Lewerenz, H.-J. Semiconductor Electrodes. Edited by H. O. Finklea. Elsevier, Amsterdam 1988. ISBN 0-444-42926-3. *Adv. Mater.* **1989**, *1* (3), 96–97.
(6) Chopra, K. L.; Paulson, P. D.; Dutta, V. Thin-Film Solar Cells: An Overview. *Prog. Photovoltaics Res. Appl.* **2004**, *12* (23), 69–92.
(7) Chapin, D. M.; Fuller, C. S.; Pearson, G. L. A New Silicon P-n Junction Photocell for Converting Solar Radiation into Electrical Power. *J. Appl. Phys.* **1954**, *25* (5), 676–677.
(8) Shockley, W.; Queisser, H. J. Detailed Balance Limit of Efficiency of P-n Junction Solar Cells. *J. Appl. Phys.* **1961**, *32* (3), 510–519.
(9) Jackson, P.; Hariskos, D.; Lotter, E.; Paetel, S.; Wuerz, R.; Menner, R.; Wischmann, W.; Powalla, M. New World Record Efficiency for Cu(In,Ga)Se2 Thin-Film Solar Cells beyond 20%. *Prog. Photovoltaics Res. Appl.* **2011**, *19* (7), 894–897.
(10) Razykov, T. M.; Ferekides, C. S.; Morel, D.; Stefanakos, E.; Ullal, H. S.; Upadhyaya, H. M. Solar Photovoltaic Electricity: Current Status and Future Prospects. *Sol. Energy* **2011**, *85* (8), 1580–1608.
(11) Wang, H. Progress in Thin Film Solar Cells Based on Cu 2 ZnSnS 4. *Int. J. Photoenergy* **2011**, *2011* (Figure 2).
(12) Chen, S.; Yang, J.-H.; Gong, X. G.; Walsh, A.; Wei, S.-H. Intrinsic Point Defects and Complexes in the Quaternary Kesterite Semiconductor Cu2ZnSnS4. *Phys. Rev. B* **2010**, *81* (24), 245204.
(13) Schäfer, W.; Nitsche, R. Tetrahedral Quaternary Chalcogenides of the Type Cu2□II□IV□S4(Se4). *Mater. Res. Bull.* **1974**, *9* (5), 645–654.
(14) Lu, X.; Zhuang, Z.; Peng, Q.; Li, Y. Wurtzite Cu2ZnSnS4 Nanocrystals: A Novel Quaternary Semiconductor. *Chem. Commun.* **2011**, *47* (11), 3141.
(15) Hajdeu-Chicarosh, E. Variable-Range Hopping Conduction in the Kesterite and Wurtzstannite Cu2ZnGeS4 Single Crystals. *Surf. Eng. Appl. Electrochem.* **2018**, *54* (3), 279–285.
(16) Jiang, M.; Y, X. Cu2ZnSnS4 Thin Film Solar Cells: Present Status and Future Prospects. In *Solar Cells - Research and Application Perspectives*; InTech, 2013.
(17) Paier, J.; Asahi, R.; Nagoya, A.; Kresse, G. Cu2 ZnSnS4 as a Potential Photovoltaic Material: A Hybrid Hartree-Fock Density Functional Theory Study. *Phys. Rev. B - Condens. Matter Mater. Phys.* **2009**, *79* (11), 1–8.
(18) Altamura, G.; Vidal, J. Impact of Minor Phases on the Performances of CZTSSe Thin-Film Solar Cells. *Chem. Mater.* **2016**, *28* (11), 3540–3563.
(19) Olekseyuk, I. D.; Dudchak, I. V.; Piskach, L. V. Phase Equilibria in the Cu2S-ZnS-SnS2 System. *J. Alloys Compd.* **2004**, *368* (1–2), 135–143.
(20) Mitzi, D. B.; Gunawan, O.; Todorov, T. K.; Barkhouse, D. A. R. Prospects and Performance Limitations for Cu-Zn-Sn-S-Se Photovoltaic Technology. *Philos. Trans. R. Soc. A Math. Phys. Eng. Sci.* **2013**, *371* (1996), 20110432–20110432.
(21) Suryawanshi, M. P.; Agawane, G. L.; Bhosale, S. M.; Shin, S. W.; Patil, P. S.; Kim, J. H.; Moholkar, A. V. CZTS Based Thin Film Solar Cells: A Status Review. *Mater. Technol.* **2013**, *28* (1–2), 98–109.
(22) Motohiro, H. K. and K. J. and S. Y. and T. K. and W. S. M. and T. F. and T. I. and T. Enhanced Conversion Efficiencies of Cu 2 ZnSnS 4 -Based Thin Film Solar Cells by Using Preferential Etching Technique. *Appl. Phys. Express* **2008**, *1* (4), 41201.
(23) Friedlmeier, T. M.; Wieser, N.; Walter, T.; Dittrich, H.; Schock, H. W. Heterojuncitons Based on Cu2ZnSnS4 and Cu2ZnSnSe4 Thin Films. In *14th European Conference of Photovoltaic Science and Engineering and Exhibition*; Bedford, UK, 1997; p 1242.
(24) Chalapathi, U.; Uthanna, S.; Sundara Raja, V. Growth and Characterization of Co-Evaporated Cu 2 ZnSnS 4 Thin Films. *J. Renew. Sustain. Energy* **2013**, *5* (3), 031610.
(25) Subramaniam, E. P.; Rajesh, G.; Muthukumarasamy, N.; Thambidurai, M.; Asokan, V.; Velauthapillai, D. Solar Cells of Cu2ZnSnS4thin Films Prepared by Chemical Bath Deposition Method. *Indian J. Pure Appl.*

Phys. **2014**, *52* (9), 620–624.
(26) Ennaoui, A.; Lux-Steiner, M.; Weber, A.; Abou-Ras, D.; Kötschau, I.; Schock, H.-W.; Schurr, R.; Hölzing, A.; Jost, S.; Hock, R.; et al. Cu2ZnSnS4 Thin Film Solar Cells from Electroplated Precursors: Novel Low-Cost Perspective. *Thin Solid Films* **2009**, *517* (7), 2511–2514.
(27) Wang, W.; Winkler, M. T.; Gunawan, O.; Gokmen, T.; Todorov, T. K.; Zhu, Y.; Mitzi, D. B. Device Characteristics of CZTSSe Thin-Film Solar Cells with 12.6% Efficiency. *Adv. Energy Mater.* **2014**, *4* (7), 1–5.
(28) Watson, D. F. Linker-Assisted Assembly and Interfacial Electron-Transfer Reactivity of Quantum Dot−Substrate Architectures. *J. Phys. Chem. Lett.* **2010**, *1* (15), 2299–2309.
(29) Schaller, R. D.; Klimov, V. I. High Efficiency Carrier Multiplication in PbSe Nanocrystals: Implications for Solar Energy Conversion. *Phys. Rev. Lett.* **2004**, *92* (18), 186601.
(30) Bisquert, S. G. and I. M.-S. and L. M. and N. G. and T. L.-V. and R. G. and L. J. D. and Q. S. and T. T. and J. Improving the Performance of Colloidal Quantum-Dot-Sensitized Solar Cells. *Nanotechnology* **2009**, *20* (29), 295204.
(31) Lee, H. J.; Yum, J.-H.; Leventis, H. C.; Zakeeruddin, S. M.; Haque, S. A.; Chen, P.; Seok, S. Il; Grätzel, M.; Nazeeruddin, M. K. CdSe Quantum Dot-Sensitized Solar Cells Exceeding Efficiency 1% at Full-Sun Intensity. *J. Phys. Chem. C* **2008**, *112* (30), 11600–11608.
(32) Chen, J.; Song, J. L.; Sun, X. W.; Deng, W. Q.; Jiang, C. Y.; Lei, W.; Huang, J. H.; Liu, R. S. An Oleic Acid-Capped CdSe Quantum-Dot Sensitized Solar Cell. *Appl. Phys. Lett.* **2009**, *94* (15), 153115.
(33) Martínez-Ferrero, E.; Seró, I. M.; Albero, J.; Giménez, S.; Bisquert, J.; Palomares, E. Charge Transfer Kinetics in CdSe Quantum Dot Sensitized Solar Cells. *Phys. Chem. Chem. Phys.* **2010**, *12* (12), 2819.
(34) Guo, Q.; Ford, G. M.; Yang, W.-C.; Walker, B. C.; Stach, E. A.; Hillhouse, H. W.; Agrawal, R. Fabrication of 7.2% Efficient CZTSSe Solar Cells Using CZTS Nanocrystals. *J. Am. Chem. Soc.* **2010**, *132* (49), 17384–17386.
(35) Heller, A.; Miller, B. Some Recent Progress in Semiconductor-Liquid Junction Solar Cells. *Electrochim. Acta* **1980**, *25* (1), 29–41.
(36) Hummel, R. E. *Electronic Properties of Materials*; Springer New York: New York, NY, 2011.
(37) Bard, A. J.; Faulkner, L. R. *Electrochemical Methods : Fundamentals and Applications*; Wiley, 2001.
(38) Kamat, P. V.; Tvrdy, K.; Baker, D. R.; Radich, J. G. Beyond Photovoltaics: Semiconductor Nanoarchitectures for Liquid-Junction Solar Cells. *Chem. Rev.* **2010**, *110* (11), 6664–6688.
(39) Dai, P.; Zhang, G.; Chen, Y.; Jiang, H.; Feng, Z.; Lin, Z.; Zhan, J. Porous Copper Zinc Tin Sulfide Thin Film as Photocathode for Double Junction Photoelectrochemical Solar Cells. *Chem. Commun.* **2012**, *48* (24), 3006.
(40) Perry, M. L.; Weber, A. Z. Advanced Redox-Flow Batteries: A Perspective. *J. Electrochem. Soc.* **2016**, *163* (1), A5064–A5067.
(41) Liu, P.; Cao, Y.; Li, G.-R.; Gao, X.-P.; Ai, X.-P.; Yang, H.-X. A Solar Rechargeable Flow Battery Based on Photoregeneration of Two Soluble Redox Couples. *ChemSusChem* **2013**, *6* (5), 802–806.
(42) Leung, P.; Li, X.; León, C. P. de; Berlouis, L.; Low, C. T. J.; Walsh, F. C. Progress in Redox Flow Batteries, Remaining Challenges and Their Applications in Energy Storage. *RSC Adv.* **2012**, *2* (27), 10125–10156.
(43) Weber, A. Z.; Mench, M. M.; Meyers, J. P.; Ross, P. N.; Gostick, J. T.; Liu, Q. Redox Flow Batteries: A Review. *J. Appl. Electrochem.* **2011**, *41* (10), 1137–1164.
(44) Skyllas-Kazacos, M.; Chakrabarti, M. H.; Hajimolana, S. a.; Mjalli, F. S.; Saleem, M. Progress in Flow Battery Research and Development. *J. Electrochem. Soc.* **2011**, *158* (8), R55.
(45) Ponce de León, C.; Frías-Ferrer, A.; González-García, J.; Szánto, D. A.; Walsh, F. C. Redox Flow Cells for Energy Conversion. *J. Power Sources* **2006**, *160* (1), 716–732.
(46) Darling, R. M.; Gallagher, K. G.; Kowalski, J. A.; Ha, S.; Brushett, F. R. Pathways to Low-Cost Electrochemical Energy Storage: A Comparison of Aqueous and Nonaqueous Flow Batteries. *Energy Environ. Sci.* **2014**, *7* (11), 3459–3477.
(47) Yu, X.; Manthiram, A. Highly Reversible Room-Temperature Sulfur/Long-Chain Sodium Polysulfide Batteries. *J. Phys. Chem. Lett.* **2014**, *5* (11), 1943–1947.
(48) Ito, K.; Nakazawa, T. Electrical and Optical Properties of Stannite-Type Quaternary Semiconductor Thin Films. *Jpn. J. Appl. Phys.* **1988**, *27* (Part 1, No. 11), 2094–2097.
(49) Dun, C.; Huang, W.; Huang, H.; Xu, J.; Zhou, N.; Zheng, Y.; Tsai, H.; Nie, W.; Onken, D. R.; Li, Y.; et al. Hydrazine-Free Surface Modification of CZTSe Nanocrystals with All-Inorganic Ligand. *J. Phys. Chem. C* **2014**, *118* (51), 30302–30308.
(50) Zhou, H.; Hsu, W.-C.; Duan, H.-S.; Bob, B.; Yang, W.; Song, T.-B.; Hsu, C.-J.; Yang, Y.; Ginley, D.; Green, M. A.; et al. CZTS Nanocrystals: A Promising Approach for next Generation Thin Film Photovoltaics. *Energy*

Environ. Sci. **2013**, *6* (10), 2822.
(51) Kumar, M.; Dubey, A.; Adhikari, N.; Venkatesan, S.; Qiao, Q. Strategic Review of Secondary Phases, Defects and Defect-Complexes in Kesterite CZTS-Se Solar Cells. *Energy Environ. Sci.* **2015**, *8* (11), 3134–3159.
(52) Yang, W.; Duan, H.-S.; Bob, B.; Zhou, H.; Lei, B.; Chung, C.-H.; Li, S.-H.; Hou, W. W.; Yang, Y. Novel Solution Processing of High-Efficiency Earth-Abundant Cu2ZnSn(S,Se)4 Solar Cells. *Adv. Mater.* **2012**, *24* (47), 6323–6329.
(53) Todorov, T. K.; Reuter, K. B.; Mitzi, D. B. High-Efficiency Solar Cell with Earth-Abundant Liquid-Processed Absorber. *Adv. Mater.* **2010**, *22* (20), E156–E159.
(54) Choudhary, G.; Hansen, H. Human Health Perspective of Environmental Exposure to Hydrazines: A Review. *Chemosphere* **1998**, *37* (5), 801–843.
(55) Todorov, T.; Mitzi, D. B. Direct Liquid Coating of Chalcopyrite Light-Absorbing Layers for Photovoltaic Devices. *Eur. J. Inorg. Chem.* **2010**, *2010* (1), 17–28.
(56) Cho, J. W.; Ismail, A.; Park, S. J.; Kim, W.; Yoon, S.; Min, B. K. Synthesis of Cu 2 ZnSnS 4 Thin Films by a Precursor Solution Paste for Thin Film Solar Cell Applications. *ACS Appl. Mater. Interfaces* **2013**, *5* (10), 4162–4165.
(57) Wang, G.; Zhao, W.; Cui, Y.; Tian, Q.; Gao, S.; Huang, L.; Pan, D. Fabrication of a Cu 2 ZnSn(S,Se) 4 Photovoltaic Device by a Low-Toxicity Ethanol Solution Process. *ACS Appl. Mater. Interfaces* **2013**, *5* (20), 10042–10047.
(58) Larramona, G.; Bourdais, S.; Jacob, A.; Choné, C.; Muto, T.; Cuccaro, Y.; Delatouche, B.; Moisan, C.; Péré, D.; Dennler, G. 8.6% Efficient CZTSSe Solar Cells Sprayed from Water–Ethanol CZTS Colloidal Solutions. *J. Phys. Chem. Lett.* **2014**, *5* (21), 3763–3767.
(59) Fischereder, A.; Rath, T.; Haas, W.; Amenitsch, H.; Albering, J.; Meischler, D.; Larissegger, S.; Edler, M.; Saf, R.; Hofer, F.; et al. Investigation of Cu2ZnSnS4 Formation from Metal Salts and Thioacetamide. *Chem. Mater.* **2010**, *22* (11), 3399–3406.
(60) Sun, Y.; Zheng, H.; Li, X.; Zong, K.; Wang, H.; Liu, J.; Yan, H.; Li, K. Reaction Routes for the Formation of a Cu2ZnSnS4 Absorber Material from Homogenous Ethanol-Based Solution. *Rsc Adv.* **2013**, *3* (44), 22095–22101.
(61) Tian, Q.; Cui, Y.; Wang, G.; Pan, D. A Robust and Low-Cost Strategy to Prepare Cu 2 ZnSnS 4 Precursor Solution and Its Application in Cu 2 ZnSn(S,Se) 4 Solar Cells. *RSC Adv.* **2015**, *5* (6), 4184–4190.
(62) Fischereder, A.; Rath, T.; Haas, W.; Amenitsch, H.; Albering, J.; Meischler, D.; Larissegger, S.; Edler, M.; Saf, R.; Hofer, F.; et al. Investigation of Cu_2ZnSnS_4 Formation from Metal Salts and Thioacetamide. *Chem. Mater.* **2010**, *22* (11), 3399–3406.
(63) Katagiri, H.; Saitoh, K.; Washio, T.; Shinohara, H.; Kurumadani, T.; Miyajima, S. Development of Thin Film Solar Cell Based on Cu2ZnSnS4 Thin Films. *Sol. Energy Mater. Sol. Cells* **2001**, *65* (1–4), 141–148.
(64) Jimbo, K.; Kimura, R.; Kamimura, T.; Yamada, S.; Maw, W. S.; Araki, H.; Oishi, K.; Katagiri, H. Cu2ZnSnS4-Type Thin Film Solar Cells Using Abundant Materials. *Thin Solid Films* **2007**, *515* (15), 5997–5999.
(65) Satheesh, K.; Jayavel, R. Synthesis and Electrochemical Properties of Reduced Graphene Oxide via Chemical Reduction Using Thiourea as a Reducing Agent. *Mater. Lett.* **2013**, *113*, 5–8.
(66) El-Sayed, B. A.; Sallam, M. M. Temperature and Frequency Dependent Electrical Transport in Thiourea and Tris (Thiourea) Copper (l) Sulphate. *J. Mater. Sci. Mater. Electron.* **1999**, *10*, 63–66.
(67) Maji, S. K.; Dutta, A. K.; Bhadu, G. R.; Paul, P.; Mondal, A.; Adhikary, B. A Novel Amperometric Biosensor for Hydrogen Peroxide and Glucose Based on Cuprous Sulfide Nanoplates. *J. Mater. Chem. B* **2013**, *1* (33), 4127.
(68) Mondal, A.; Scheinert, C.; Radich, J. G. Carrier Lifetime and Charge Separation in K+-Doped CZTS Nanocrystals. *ACS Appl. Energy Mater.* **2018**, acsaem.8b01168.
(69) Tiwari, D.; Koehler, T.; Lin, X.; Harniman, R.; Griffiths, I.; Wang, L.; Cherns, D.; Klenk, R.; Fermin, D. J. Cu 2 ZnSnS 4 Thin Films Generated from a Single Solution Based Precursor: The Effect of Na and Sb Doping. *Chem. Mater.* **2016**, *28* (14), 4991–4997.
(70) Jiang, C.; Liu, W.; Talapin, D. V. Role of Precursor Reactivity in Crystallization of Solution-Processed Semiconductors: The Case of Cu2ZnSnS4. *Chem. Mater.* **2014**, *26* (13), 4038–4043.
(71) Sun, Y.; Zheng, H.; Li, X.; Zong, K.; Wang, H.; Liu, J.; Yan, H.; Li, K. Reaction Routes for the Formation of a Cu2ZnSnS4 Absorber Material from Homogenous Ethanol-Based Solution. *RSC Adv.* **2013**, *3* (44), 22095.
(72) Fontané, X.; Calvo-Barrio, L.; Izquierdo-Roca, V.; Saucedo, E.; Pérez-Rodriguez, A.; Morante, J. R.; Berg, D. M.; Dale, P. J.; Siebentritt, S. In-Depth Resolved Raman Scattering Analysis for the Identification of Secondary Phases: Characterization of Cu2ZnSnS4 Layers for Solar Cell Applications. *Appl. Phys. Lett.* **2011**,

98 (18), 181905.
(73) Himmrich, M.; Haeuseler, H. Far Infrared Studies on Stannite and Wurtzstannite Type Compounds. *Spectrochim. Acta* **1991**, *47A* (7), 933–942.
(74) Fernandes, P. A.; Salomé, P. M. P.; da Cunha, A. F. Study of Polycrystalline Cu2ZnSnS4 Films by Raman Scattering. *J. Alloys Compd.* **2011**, *509* (28), 7600–7606.
(75) Cheng, a.-J.; Manno, M.; Khare, A.; Leighton, C.; Campbell, S. a.; Aydil, E. S. Imaging and Phase Identification of Cu 2 ZnSnS 4 Thin Films Using Confocal Raman Spectroscopy. *J. Vac. Sci. Technol. A Vacuum, Surfaces, Film.* **2011**, *29* (5), 051203.
(76) Dimitrievska, M.; Fairbrother, A.; Fontané, X.; Jawhari, T.; Izquierdo-Roca, V.; Saucedo, E.; Pérez-Rodríguez, A. Multiwavelength Excitation Raman Scattering Study of Polycrystalline Kesterite Cu 2 ZnSnS 4 Thin Films. *Appl. Phys. Lett.* **2014**, *104* (2), 021901.
(77) Valakh, M. Y.; Kolomys, O. F.; Ponomaryov, S. S.; Yukhymchuk, V. O.; Babichuk, I. S.; Izquierdo-Roca, V.; Saucedo, E.; Perez-Rodriguez, A.; Morante, J. R.; Schorr, S.; et al. Raman Scattering and Disorder Effect in Cu 2 ZnSnS 4. *Phys. status solidi - Rapid Res. Lett.* **2013**, *7* (4), 258–261.
(78) Fontané, X.; Izquierdo-Roca, V.; Saucedo, E.; Schorr, S.; Yukhymchuk, V. O.; Valakh, M. Y.; Pérez-Rodríguez, A.; Morante, J. R. Vibrational Properties of Stannite and Kesterite Type Compounds: Raman Scattering Analysis of Cu2(Fe,Zn)SnS4. *J. Alloys Compd.* **2012**, *539*, 190–194.
(79) Zhong, J.; Xia, Z.; Zhang, C.; Li, B.; Liu, X.; Cheng, Y.; Tang, J. One-Pot Synthesis of Self-Stabilized Aqueous Nanoinks for Cu 2 ZnSn(S,Se) 4 Solar Cells. *Chem. Mater.* **2014**, *26* (11), 3573–3578.
(80) Singh, A.; Geaney, H.; Laffir, F.; Ryan, K. M. Colloidal Synthesis of Wurtzite Cu 2 ZnSnS 4 Nanorods and Their Perpendicular Assembly. *J. Am. Chem. Soc.* **2012**, *134* (6), 2910–2913.
(81) Li, M.; Zhou, W.-H.; Guo, J.; Zhou, Y.-L.; Hou, Z.-L.; Jiao, J.; Zhou, Z.-J.; Du, Z.-L.; Wu, S.-X. Synthesis of Pure Metastable Wurtzite CZTS Nanocrystals by Facile One-Pot Method. *J. Phys. Chem. C* **2012**, *116* (50), 26507–26516.
(82) Chao, J.; Xie, Z.; Duan, X.; Dong, Y.; Wang, Z.; Xu, J.; Liang, B.; Shan, B.; Ye, J.; Chen, D.; et al. Visible-Light-Driven Photocatalytic and Photoelectrochemical Properties of Porous SnSx(x = 1,2) Architectures. *CrystEngComm* **2012**, *14* (9), 3163.
(83) Katagiri, H.; Jimbo, K.; Maw, W. S.; Oishi, K.; Yamazaki, M.; Araki, H.; Takeuchi, A. Development of CZTS-Based Thin Film Solar Cells. *Thin Solid Films* **2009**, *517* (7), 2455–2460.
(84) Fernandes, P. a.; Salomé, P. M. P.; da Cunha, a. F. Growth and Raman Scattering Characterization of Cu2ZnSnS4 Thin Films. *Thin Solid Films* **2009**, *517* (7), 2519–2523.
(85) Katagiri, H. Cu2ZnSnS4thin Film Solar Cells. *Thin Solid Films* **2005**, *480–481*, 426–432.
(86) Xie, M.; Zhuang, D.; Zhao, M.; Li, B.; Cao, M.; Song, J. Fabrication of Cu2ZnSnS4thin Films Using a Ceramic Quaternary Target. *Vacuum* **2014**, *101*, 146–150.
(87) Akhavan, V. A.; Goodfellow, B. W.; Panthani, M. G.; Steinhagen, C.; Harvey, T. B.; Stolle, C. J.; Korgel, B. A. Colloidal CIGS and CZTS Nanocrystals: A Precursor Route to Printed Photovoltaics. *J. Solid State Chem.* **2012**, *189*, 2–12.
(88) Kameyama, T.; Osaki, T.; Okazaki, K.; Shibayama, T.; Kudo, A.; Kuwabata, S.; Torimoto, T. Preparation and Photoelectrochemical Properties of Densely Immobilized Cu2ZnSnS4 Nanoparticle Films. *J. Mater. Chem.* **2010**, *20* (25), 5319.
(89) Walter, M. G.; Warren, E. L.; McKone, J. R.; Boettcher, S. W.; Mi, Q.; Santori, E. A.; Lewis, N. S. Solar Water Splitting Cells. *Chem. Rev.* **2010**, *110* (11), 6446–6473.
(90) Vaccarello, D.; Tapley, A.; Ding, Z. Optimization of the Cu2ZnSnS4 Nanocrystal Recipe by Means of Photoelectrochemical Measurements. *RSC Adv.* **2013**, *3* (11), 3512.
(91) Shinde, N. M.; Lokhande, C. D.; Kim, J. H.; Moon, J. H. Low Cost and Large Area Novel Chemical Synthesis of Cu2ZnSnS4 (CZTS) Thin Films. *J. Photochem. Photobiol. A Chem.* **2012**, *235*, 14–20.
(92) Pawar, S. M.; Pawar, B. S.; Moholkar, A. V.; Choi, D. S.; Yun, J. H.; Moon, J. H.; Kolekar, S. S.; Kim, J. H. Single Step Electrosynthesis of Cu2ZnSnS4 (CZTS) Thin Films for Solar Cell Application. *Electrochim. Acta* **2010**, *55* (12), 4057–4061.
(93) Abermann, S. Non-Vacuum Processed next Generation Thin Film Photovoltaics: Towards Marketable Efficiency and Production of CZTS Based Solar Cells. *Sol. Energy* **2013**, *94*, 37–70.
(94) Zhou, H.; Hsu, W.-C.; Duan, H.-S.; Bob, B.; Yang, W.; Song, T.-B.; Hsu, C.-J.; Yang, Y. CZTS Nanocrystals: A Promising Approach for next Generation Thin Film Photovoltaics. *Energy Environ. Sci.* **2013**, *6* (10), 2822.
(95) Dun, C.; Huang, W.; Huang, H.; Xu, J.; Zhou, N.; Zheng, Y.; Tsai, H.; Nie, W.; Onken, D. R.; Li, Y.; et al. Hydrazine-Free Surface Modification of CZTSe Nanocrystals with All-Inorganic Ligand. *J. Phys. Chem. C* **2014**, *118* (51), 30302–30308.

(96) Ito, K. An Overview of CZTS-Based Thin-Film Solar Cells. *Copper Zinc Tin Sulfide-Based Thin-Film Solar Cells*. John Wiley & Sons Ltd 2015, pp 1–41.
(97) Chen, S.; Walsh, A.; Luo, Y.; Yang, J.-H.; Gong, X. G.; Wei, S.-H. Wurtzite-Derived Polytypes of Kesterite and Stannite Quaternary Chalcogenide Semiconductors. *Phys. Rev. B* **2010**, *82* (19).
(98) Han, D.; Sun, Y. Y.; Bang, J.; Zhang, Y. Y.; Sun, H.-B.; Li, X.-B.; Zhang, S. B. Deep Electron Traps and Origin Ofp-Type Conductivity in the Earth-Abundant Solar-Cell Material Cu2ZnSnS4. *Phys. Rev. B* **2013**, *87* (15).
(99) Hsieh, Y.-T.; Han, Q.; Jiang, C.; Song, T.-B.; Chen, H.; Meng, L.; Zhou, H.; Yang, Y. Efficiency Enhancement of Cu 2 ZnSn(S,Se) 4 Solar Cells via Alkali Metals Doping. *Adv. Energy Mater.* **2016**, *6* (7), 1502386.
(100) Prabhakar, T.; Jampana, N. Effect of Sodium Diffusion on the Structural and Electrical Properties of Cu2ZnSnS4 Thin Films. *Sol. Energy Mater. Sol. Cells* **2011**, *95* (3), 1001–1004.
(101) Singh, O. P.; Sharma, A.; Gour, K. S.; Husale, S.; Singh, V. N. Fast Switching Response of Na-Doped CZTS Photodetector from Visible to NIR Range. *Sol. Energy Mater. Sol. Cells* **2016**, *157*, 28–34.
(102) Tong, Z.; Yan, C.; Su, Z.; Zeng, F.; Yang, J.; Li, Y.; Jiang, L.; Lai, Y.; Liu, F. Effects of Potassium Doping on Solution Processed Kesterite Cu 2 ZnSnS 4 Thin Film Solar Cells. *Appl. Phys. Lett.* **2014**, *105* (22), 223903.
(103) Zhao, Z.-Y.; Zhao, X. First-Principles Study on Doping Effects of Sodium in Kesterite Cu 2 ZnSnS 4. *Inorg. Chem.* **2014**, *53* (17), 9235–9241.
(104) Zhou, H.; Song, T.-B.; Hsu, W.-C.; Luo, S.; Ye, S.; Duan, H.-S.; Hsu, C.-J.; Yang, W.; Yang, Y. Rational Defect Passivation of Cu 2 ZnSn(S,Se) 4 Photovoltaics with Solution-Processed Cu 2 ZnSnS 4 :Na Nanocrystals. *J. Am. Chem. Soc.* **2013**, *135* (43), 15998–16001.
(105) Johnson, M.; Baryshev, S. V; Thimsen, E.; Manno, M.; Zhang, X.; Veryovkin, I. V; Leighton, C.; Aydil, E. S. Alkali-Metal-Enhanced Grain Growth in Cu2ZnSnS4 Thin Films. *Energy Environ. Sci.* **2014**, *7* (6), 1931–1938.
(106) Jackson, P.; Hariskos, D.; Wuerz, R.; Wischmann, W.; Powalla, M. Compositional Investigation of Potassium Doped Cu(In,Ga)Se2solar Cells with Efficiencies up to 20.8%. *Phys. status solidi - Rapid Res. Lett.* **2014**, *8* (3), 219–222.
(107) Williams, B. A.; Smeaton, M. A.; Trejo, N. D.; Francis, L. F.; Aydil, E. S. Effect of Nanocrystal Size and Carbon on Grain Growth during Annealing of Copper Zinc Tin Sulfide Nanocrystal Coatings. *Chem. Mater.* **2017**, *29* (4), 1676–1683.
(108) Chernomordik, B. D.; Ketkar, P. M.; Hunter, A. K.; Béland, A. E.; Deng, D. D.; Aydil, E. S. Microstructure Evolution During Selenization of Cu2ZnSnS4 Colloidal Nanocrystal Coatings. *Chem. Mater.* **2016**, *28* (5), 1266–1276.
(109) Williams, B. A.; Mahajan, A.; Smeaton, M. A.; Holgate, C. S.; Aydil, E. S.; Francis, L. F. Formation of Copper Zinc Tin Sulfide Thin Films from Colloidal Nanocrystal Dispersions via Aerosol-Jet Printing and Compaction. *ACS Appl. Mater. Interfaces* **2015**, *7* (21), 11526–11535.
(110) Chernomordik, B. D.; Béland, A. E.; Deng, D. D.; Francis, L. F.; Aydil, E. S. Microstructure Evolution and Crystal Growth in Cu2ZnSnS4 Thin Films Formed By Annealing Colloidal Nanocrystal Coatings. *Chem. Mater.* **2014**, *26* (10), 3191–3201.
(111) Chernomordik, B. D.; Béland, A. E.; Trejo, N. D.; Gunawan, A. A.; Deng, D. D.; Mkhoyan, K. A.; Aydil, E. S. Rapid Facile Synthesis of Cu2ZnSnS4 Nanocrystals. *J. Mater. Chem. A* **2014**, *2* (27), 10389.
(112) Steinhagen, C.; Panthani, M. G.; Akhavan, V.; Goodfellow, B.; Koo, B.; Korgel, B. A. Synthesis of Cu2ZnSnS4Nanocrystals for Use in Low-Cost Photovoltaics. *J. Am. Chem. Soc.* **2009**, *131* (35), 12554–12555.
(113) Chernomordik, B. D.; Béland, a. E.; Trejo, N. D.; Gunawan, a. a.; Deng, D. D.; Mkhoyan, K. a.; Aydil, E. S. Rapid Facile Synthesis of Cu2ZnSnS4 Nanocrystals. *J. Mater. Chem. A* **2014**, *2* (27), 10389.
(114) Korala, L.; Braun, M. B.; Kephart, J. M.; Tregillus, Z.; Prieto, A. L. Ligand-Exchanged CZTS Nanocrystal Thin Films: Does Nanocrystal Surface Passivation Effectively Improve Photovoltaic Performance? *Chem. Mater.* **2017**, *29* (16), 6621–6629.
(115) Chernomordik, B. D.; Béland, A. E.; Trejo, N. D.; Gunawan, A. A.; Deng, D. D.; Mkhoyan, K. A.; Aydil, E. S. Rapid Facile Synthesis of Cu2ZnSnS4 Nanocrystals. *J. Mater. Chem. A* **2014**, *2* (27), 10389–10395.
(116) Steinhagen, C.; Panthani, M. G.; Akhavan, V.; Goodfellow, B.; Koo, B.; Korgel, B. A. Synthesis of Cu_2ZnSnS_4 Nanocrystals for Use in Low-Cost Photovoltaics. *J. Am. Chem. Soc.* **2009**, *131* (35), 12554–12555.
(117) Kwon, S. G.; Hyeon, T. Formation Mechanisms of Uniform Nanocrystals via Hot-Injection and Heat-up Methods. *Small* **2011**, *7* (19), 2685–2702.
(118) Tsukigase, H.; Suzuki, Y.; Berger, M.-H.; Sagawa, T.; Yoshikawa, S. Synthesis of SnS Nanoparticles by SILAR Method for Quantum Dot-Sensitized Solar Cells. *J. Nanosci. Nanotechnol.* **2011**, *11* (3), 1914–1922.

(119) Hurtado, M.; Cruz, S. D.; Becerra, R. A.; Calderon, C.; Bartolo-Perez, P.; Gordillo, G. XPS Analysis and Structural Characterization of CZTS Thin Films Prepared Using Solution and Vacuum Based Deposition Techniques. *2014 IEEE 40th Photovoltaic Specialist Conference (PVSC)*. IEEE 2014.

(120) Nguyen, T. T. T.; Shin, H.-Y.; Kim, G. Y.; Kim, J. R.; Jo, W.; Yoon, S.; Lee, K. D.; Kim, J. Y. Raman Scattering Studies of Cu2ZnSnS4 Thin Films: Local Distribution of the Secondary Phase Cu2−x S and the Effect of KCN Etching on Cu2−x S. *J. Korean Phys. Soc.* **2015**, *66* (1), 117–122.

(121) Dimitrievska, M.; Boero, F.; Litvinchuk, A. P.; Delsante, S.; Borzone, G.; Perez-Rodriguez, A.; Izquierdo-Roca, V. Structural Polymorphism in "Kesterite" Cu2ZnSnS4: Raman Spectroscopy and First-Principles Calculations Analysis. *Inorg. Chem.* **2017**, *56* (6), 3467–3474.

(122) Guc, M.; Levcenko, S.; Bodnar, I. V; Izquierdo-Roca, V.; Fontane, X.; Volkova, L. V; Arushanov, E.; Pérez-Rodríguez, A. Polarized Raman Scattering Study of Kesterite Type Cu2ZnSnS4 Single Crystals. *Sci. Rep.* **2016**, *6* (1).

(123) Ming, J.; Tan, R.; Lee, Y. H.; Pedireddy, S.; Baikie, T.; Ling, X. Y.; Wong, L. H. Understanding the Synthetic Pathway of Single Phase Quarternary Semiconductor Using Surface-Enhanced Raman Scattering : A Case of Wurtzite Cu ZnSnS Nanoparticles. **2014**.

(124) Li, W.; Su, Z.; Tan, J. M. R.; Chiam, S. Y.; Seng, H. L.; Magdassi, S.; Wong, L. H. Revealing the Role of Potassium Treatment in CZTSSe Thin Film Solar Cells. *Chem. Mater.* **2017**, *29* (10), 4273–4281.

(125) Rey, G.; Babbe, F.; Weiss, T. P.; Elanzeery, H.; Melchiorre, M.; Valle, N.; Adib, B. El; Siebentritt, S. Post-Deposition Treatment of Cu 2 ZnSnSe 4 with Alkalis. *Thin Solid Films* **2017**, *633*, 162–165.

(126) Zhao, Z. Y.; Zhao, X. First-Principles Study on Doping Effects of Sodium in Kesterite Cu2ZnSnS4. *Inorg. Chem.* **2014**, *53* (17), 9235–9241.

(127) Zhou, H.; Song, T.-B.; Hsu, W.-C.; Luo, S.; Ye, S.; Duan, H.-S.; Hsu, C.-J.; Yang, W.; Yang, Y. Rational Defect Passivation of Cu2ZnSn(S,Se)4 Photovoltaics with Solution-Processed Cu2ZnSnS4:Na Nanocrystals. *J. Am. Chem. Soc.* **2013**, *135* (43), 15998–16001.

(128) Li, J.; Wang, D.; Li, X.; Zeng, Y.; Zhang, Y. Thin-Film Solar Cells: Cation Substitution in Earth-Abundant Kesterite Photovoltaic Materials (Adv. Sci. 4/2018). *Adv. Sci.* **2018**, *5* (4), 1870021.

(129) Xiao, W.; Wang, J. N.; Zhao, X. S.; Wang, J. W.; Huang, G. J.; Cheng, L.; Jiang, L. J.; Wang, L. G. Intrinsic Defects and Na Doping in Cu2ZnSnS4: A Density-Functional Theory Study. *Sol. Energy* **2015**, *116*, 125–132.

(130) Berera, R.; van Grondelle, R.; Kennis, J. T. M. Ultrafast Transient Absorption Spectroscopy: Principles and Application to Photosynthetic Systems. *Photosynth. Res.* **2009**, *101* (2–3), 105–118.

(131) Diguna, L. J.; Shen, Q.; Sato, A.; Katayama, K.; Sawada, T.; Toyoda, T. Optical Absorption and Ultrafast Carrier Dynamics Characterization of CdSe Quantum Dots Deposited on Different Morphologies of Nanostructured TiO2 Films. *Mater. Sci. Eng. C* **2007**, *27* (5–8), 1514–1520.

(132) Manser, J. S.; Kamat, P. V. Band Filling with Free Charge Carriers in Organometal Halide Perovskites. *Nat. Photonics* **2014**, *8* (9), 737–743.

(133) Phuong, L. Q.; Okano, M.; Yamada, Y.; Yamashita, G.; Morimoto, T.; Nagai, M. Ultrafast Free-Carrier Dynamics in Cu 2 ZnSnS 4 Single Crystals Studied Using Femtosecond Time-Resolved Optical Spectroscopy. **2014**, *231902*.

(134) Pundsack, T. J.; Chernomordik, B. D.; Béland, A. E.; Aydil, E. S.; Blank, D. A. Excited-State Dynamics in CZTS Nanocrystals. *J. Phys. Chem. Lett.* **2013**, *4* (16), 2711–2714.

(135) Khare, A.; Himmetoglu, B.; Cococcioni, M.; Aydil, E. S. First Principles Calculation of the Electronic Properties and Lattice Dynamics of Cu 2 ZnSn(S 1−x Se x) 4. *J. Appl. Phys.* **2012**, *111* (12), 123704.

(136) Persson, C. Electronic and Optical Properties of Cu2ZnSnS4 and Cu2ZnSnSe4. *J. Appl. Phys.* **2010**, *107* (5), 053710.

(137) Radich, J. G.; Dwyer, R.; Kamat, P. V. Cu2S Reduced Graphene Oxide Composite for High-Efficiency Quantum Dot Solar Cells. Overcoming the Redox Limitations of S 2 – /Sn 2– at the Counter Electrode. *J. Phys. Chem. Lett.* **2011**, *2* (19), 2453–2460.

(138) Zhang, J. Z.; O'Neil, R. H.; Roberti, T. W. Femtosecond Studies of Interfacial Electron-hole Recombination in Aqueous CdS Colloids. *Appl. Phys. Lett.* **1994**, *64* (15), 1989–1991.

(139) Baral, S.; Fojtik, A.; Weller, H.; Henglein, A. Photochemistry and Radiation Chemistry of Colloidal Semiconductors. 12. Intermediates of the Oxidation of Extremely Small Particles of Cadmium Sulfide, Zinc Sulfide, and Tricadmium Diphosphide and Size Quantization Effects (a Pulse Radiolysis Study). *J. Am. Chem. Soc.* **1986**, *108* (3), 375–378.

(140) Dibbell, R. S.; Watson, D. F. Distance-Dependent Electron Transfer in Tethered Assemblies of CdS Quantum Dots and TiO 2 Nanoparticles. *J. Phys. Chem. C* **2009**, *113*, 3139–3149.

(141) Zheng, K.; Žídek, K.; Abdellah, M.; Zhang, W.; Chábera, P. Ultrafast Charge Transfer from CdSe Quantum Dots to P-Type NiO : Hole Injection vs . Hole Trapping. 1–10.
(142) Pernik, D. R.; Tvrdy, K.; Radich, J. G.; Kamat, P. V. Tracking the Adsorption and Electron Injection Rates of CdSe Quantum Dots on TiO2: Linked versus Direct Attachment. *J. Phys. Chem. C* **2011**, *115* (27), 13511–13519.
(143) Tvrdy, K.; Frantsuzov, P. A.; Kamat, P. V. Photoinduced Electron Transfer from Semiconductor Quantum Dots to Metal Oxide Nanoparticles. *Proc. Natl. Acad. Sci.* **2010**, *108* (1), 29–34.
(144) Chakrapani, V.; Tvrdy, K.; Kamat, P. V. Modulation of Electron Injection in CdSe−TiO2System through Medium Alkalinity. *J. Am. Chem. Soc.* **2010**, *132* (4), 1228–1229.
(145) Radich, J. G.; Peeples, N. R.; Santra, P. K.; Kamat, P. V. Charge Transfer Mediation through CuxS. The Hole Story of CdSe in Polysulfide. *J. Phys. Chem. C* **2014**, *118* (30), 16463–16471.
(146) Colombara, D.; Dale, P. J.; Kissling, G. P.; Peter, L. M.; Tombolato, S. Photoelectrochemical Screening of Solar Cell Absorber Layers: Electron Transfer Kinetics and Surface Stabilization. *J. Phys. Chem. C* **2016**, *120* (29), 15956–15965.
(147) Guijarro, N.; Prévot, M. S.; Sivula, K. Enhancing the Charge Separation in Nanocrystalline Cu2ZnSnS4 Photocathodes for Photoelectrochemical Application: The Role of Surface Modifications. *J. Phys. Chem. Lett.* **2014**, *5* (21), 3902–3908.
(148) Riha, S. C.; Parkinson, B. A.; Prieto, A. L. Compositionally Tunable Cu 2 ZnSn(S 1– x Se x) 4 Nanocrystals: Probing the Effect of Se-Inclusion in Mixed Chalcogenide Thin Films. *J. Am. Chem. Soc.* **2011**, *133* (39), 15272–15275.
(149) Wang, J.; Zhang, P.; Song, X.; Gao, L. Cu2ZnSnS4 Thin Films: Spin Coating Synthesis and Photoelectrochemistry. *RSC Adv.* **2014**, *4* (41), 21318–21324.
(150) Yang, W.; Oh, Y.; Kim, J.; Jeong, M. J.; Park, J. H.; Moon, J. Molecular Chemistry-Controlled Hybrid Ink-Derived Efficient Cu2ZnSnS4 Photocathodes for Photoelectrochemical Water Splitting. *ACS Energy Lett.* **2016**, *1* (6), 1127–1136.
(151) Ghorpade, U.; Suryawanshi, M.; Shin, S. W.; Gurav, K.; Patil, P.; Pawar, S.; Hong, C. W.; Kim, J. H.; Kolekar, S. Towards Environmentally Benign Approaches for the Synthesis of CZTSSe Nanocrystals by a Hot Injection Method: A Status Review. *Chem. Commun.* **2014**, *50* (77), 11258–11273.
(152) Kameyama, T.; Osaki, T.; Okazaki, K.; Shibayama, T.; Kudo, A.; Kuwabata, S.; Torimoto, T. Preparation and Photoelectrochemical Properties of Densely Immobilized Cu2ZnSnS4 Nanoparticle Films. *J. Mater. Chem.* **2010**, *20* (25), 5319.
(153) Bartolozzi, M. Development of Redox Flow Batteries. A Historical Bibliography. *J. Power Sources* **1989**, *27* (3), 219–234.
(154) Zhou, H.; Hsu, W.-C.; Duan, H.-S.; Bob, B.; Yang, W.; Song, T.-B.; Hsu, C.-J.; Yang, Y. CZTS Nanocrystals: A Promising Approach for next Generation Thin Film Photovoltaics. *Energy Environ. Sci.* **2013**, *6* (10), 2822.
(155) Zeng, X.; Zhang, W.; Xie, Y.; Xiong, D.; Chen, W.; Xu, X.; Wang, M.; Cheng, Y. B. Low-Cost Porous Cu2ZnSnSe4film Remarkably Superior to Noble Pt as Counter Electrode in Quantum Dot-Sensitized Solar Cell System. *J. Power Sources* **2013**, *226*, 359–362.
(156) Zhang, Y.; Shi, C.; Dai, X.; Liu, F.; Fang, X.; Zhu, J. Pyrolysis Preparation of Cu2ZnSnS4thin Film and Its Application to Counter Electrode in Quantum Dot-Sensitized Solar Cells. *Electrochim. Acta* **2014**, *118*, 41–44.
(157) Xu, J.; Yang, X.; Yang, Q.-D.; Wong, T.-L.; Lee, C.-S. Cu_2ZnSnS_4 Hierarchical Microspheres as an Effective Counter Electrode Material for Quantum Dot Sensitized Solar Cells. *J. Phys. Chem. C* **2012**, *116* (37), 19718–19723.
(158) Cao, Y.; Xiao, Y.; Jung, J. Y.; Um, H. D.; Jee, S. W.; Choi, H. M.; Bang, J. H.; Lee, J. H. Highly Electrocatalytic Cu2ZnSn(S1- XSex)4counter Electrodes for Quantum-Dot-Sensitized Solar Cells. *ACS Appl. Mater. Interfaces* **2013**, *5* (3), 479–484.
(159) Hodes, G. Electrocatalytic Electrodes for the Polysulfide Redox System. *J. Electrochem. Soc.* **1980**, *127* (3), 544.
(160) Faber, M. S.; Lukowski, M. A.; Ding, Q.; Kaiser, N. S.; Jin, S. Earth-Abundant Metal Pyrites (FeS 2 , CoS 2 , NiS 2 , and Their Alloys) for Highly Efficient Hydrogen Evolution and Polysulfide Reduction Electrocatalysis. *J. Phys. Chem. C* **2014**, *118* (37), 21347–21356.
(161) Lando, D.; Manassen, J.; Hodes, G.; Cahen, D. Transient Photocurrents and Conversion Losses in Polysulfide-Based Photoelectrochemical Cells. *J. Am. Chem. Soc.* **1979**, *101* (14), 3969–3971.
(162) Berera, R.; van Grondelle, R.; Kennis, J. T. M. Ultrafast Transient Absorption Spectroscopy: Principles and Application to Photosynthetic Systems. *Photosynth. Res.* **2009**, *101* (2–3), 105–118.

(163) Nakamura, R.; Makuta, S.; Tachibana, Y. Electron Injection Dynamics at the SILAR Deposited CdS Quantum Dot/TiO 2 Interface. *J. Phys. Chem. C* **2015**, *119* (35), 20357–20362.
(164) Sykora, M.; Petruska, M. A.; Alstrum-acevedo, J.; Bezel, I.; Meyer, T. J.; Klimov, V. I. Photoinduced Charge Transfer between CdSe Nanocrystal Quantum Dots and Ru - Polypyridine Complexes. *J. Phys. Chem* **2006**, *107 (37)*, 9984–9985.
(165) Klimov, V.; Bolivar, P. H.; Kurz, H. Ultrafast Carrier Dynamics in Semiconductor Quantum Dots. *Phys. Rev. B* **1996**, *53* (3), 1463–1467.
(166) Guijarro, N.; Lana-Villarreal, T.; Shen, Q.; Toyoda, T.; Gómez, R. Sensitization of Titanium Dioxide Photoanodes with Cadmium Selenide Quantum Dots Prepared by SILAR: Photoelectrochemical and Carrier Dynamics Studies. *J. Phys. Chem. C* **2010**, *114* (50), 21928–21937.
(167) Guijarro, N.; Shen, Q.; Giménez, S.; Mora-Seró, I.; Bisquert, J.; Lana-Villarreal, T.; Toyoda, T.; Gómez, R. Direct Correlation between Ultrafast Injection and Photoanode Performance in Quantum Dot Sensitized Solar Cells. *J. Phys. Chem. C* **2010**, *114* (50), 22352–22360.
(168) Todorov, T. K.; Tang, J.; Bag, S.; Gunawan, O.; Gokmen, T.; Zhu, Y.; Mitzi, D. B. Beyond 11% Efficiency: Characteristics of State-of-the-Art Cu 2 ZnSn(S,Se) 4 Solar Cells. *Adv. Energy Mater.* **2013**, *3* (1), 34–38.
(169) Liu, F.; Zhu, J.; Wei, J.; Li, Y.; Hu, L.; Huang, Y.; Takuya, O.; Shen, Q.; Toyoda, T.; Zhang, B.; et al. Ex Situ CdSe Quantum Dot-Sensitized Solar Cells Employing Inorganic Ligand Exchange To Boost Efficiency. *J. Phys. Chem. C* **2014**, *118* (1), 214–222.
(170) Zeng, R.; Zhang, T.; Dai, G.; Zou, B. Highly Emissive, Color-Tunable, Phosphine-Free Mn:ZnSe/ZnS Core/Shell and Mn:ZnSeS Shell-Alloyed Doped Nanocrystals. *J. Phys. Chem. C* **2011**, *115* (7), 3005–3010.
(171) Murray, C. B.; Norris, D. J.; Bawendi, M. G. Synthesis and Characterization of Nearly Monodisperse CdE (E = Sulfur, Selenium, Tellurium) Semiconductor Nanocrystallites. *J. Am. Chem. Soc.* **1993**, *115* (19), 8706–8715.
(172) Zhao, Y.; Han, X.; Li, W.; Liu, L.; Tanaka, T. Synthesis of the Cu2ZnSn(S,Se)4 Alloys with Tunable Phase Structure and Composition via a Novel Non-Toxic Solution Method. *RSC Adv.* **2013**, *3* (48), 26160.
(173) Wei, H.; Ye, Z.; Li, M.; Su, Y.; Yang, Z.; Zhang, Y. Tunable Band Gap Cu2ZnSnS4xSe4(1−x) Nanocrystals: Experimental and First-Principles Calculations. *CrystEngComm* **2011**, *13* (7), 2222.
(174) Repins, I.; Beall, C.; Vora, N.; DeHart, C.; Kuciauskas, D.; Dippo, P.; To, B.; Mann, J.; Hsu, W.-C.; Goodrich, A.; et al. Co-Evaporated Cu2ZnSnSe4 Films and Devices. *Sol. Energy Mater. Sol. Cells* **2012**, *101*, 154–159.
(175) Lee, Y. S.; Gershon, T.; Gunawan, O.; Todorov, T. K.; Gokmen, T.; Virgus, Y.; Guha, S. Cu 2 ZnSnSe 4 Thin-Film Solar Cells by Thermal Co-Evaporation with 11.6% Efficiency and Improved Minority Carrier Diffusion Length. *Adv. Energy Mater.* **2015**, *5* (7), 1401372.
(176) Guo, Q.; Ford, G. M.; Yang, W.-C.; Walker, B. C.; Stach, E. a.; Hillhouse, H. W.; Agrawal, R. Fabrication of 7.2% Efficient CZTSSe Solar Cells Using CZTS Nanocrystals. *J. Am. Chem. Soc.* **2010**, *132* (49), 17384–17386.
(177) Brammertz, G.; Buffière, M.; Oueslati, S.; ElAnzeery, H.; Ben Messaoud, K.; Sahayaraj, S.; Köble, C.; Meuris, M.; Poortmans, J. Characterization of Defects in 9.7% Efficient Cu 2 ZnSnSe 4 -CdS-ZnO Solar Cells. *Appl. Phys. Lett.* **2013**, *103* (16), 163904.
(178) Shin, B.; Zhu, Y.; Bojarczuk, N. A.; Jay Chey, S.; Guha, S. Control of an Interfacial MoSe 2 Layer in Cu 2 ZnSnSe 4 Thin Film Solar Cells: 8.9% Power Conversion Efficiency with a TiN Diffusion Barrier. *Appl. Phys. Lett.* **2012**, *101* (5), 053903.
(179) Sun, M.; Yang, X. Phosphine-Free Synthesis of High-Quality CdSe Nanocrystals in Noncoordination Solvents: "Activating Agent" and "Nucleating Agent" Controlled Nucleation and Growth. *J. Phys. Chem. C* **2009**, *113* (20), 8701–8709.
(180) Peng, X.; Schlamp, M. C.; Kadavanich, A. V.; Alivisatos, A. P. Epitaxial Growth of Highly Luminescent CdSe/CdS Core/Shell Nanocrystals with Photostability and Electronic Accessibility. *J. Am. Chem. Soc.* **1997**, *119* (30), 7019–7029.
(181) Liu, Y.; Yao, D.; Shen, L.; Zhang, H.; Zhang, X.; Yang, B. Alkylthiol-Enabled Se Powder Dissolution in Oleylamine at Room Temperature for the Phosphine-Free Synthesis of Copper-Based Quaternary Selenide Nanocrystals. *J. Am. Chem. Soc.* **2012**, *134* (17), 7207–7210.
(182) Wei, Y.; Yang, J.; Lin, A. W. H.; Ying, J. Y. Highly Reactive Se Precursor for the Phosphine-Free Synthesis of Metal Selenide Nanocrystals. *Chem. Mater.* **2010**, *22* (20), 5672–5677.
(183) Koo, B.; Patel, R. N.; Korgel, B. A. Synthesis of CuInSe 2 Nanocrystals with Trigonal Pyramidal Shape Different Nanocrystals Can Be Synthesized with Optical Gaps at The. *J. Am. Chem. Soc.* **2009**, 3134–3135.
(184) Allen, F. H.; Kennard, O.; Watson, D. G.; Brammer, L.; Orpen, A. G.; Taylor, R. Tables of Bond Lengths Determined by X-Ray and Neutron Diffraction. Part 1. Bond Lengths in Organic Compounds. *J. Chem. Soc.*

Perkin Trans. 2 **1987**, No. 12, S1.
(185) Wiberg, K. B.; Wang, Y. A Comparison of Some Properties of C=O and C=S Bonds. *Arkivoc* **2010**, *2011* (5), 45.
(186) Fabian, J.; Viola, H.; Mayer, R. Quantitative Beschreibung Der UV-S-Absorptionen Einfacher Thiocarbonylverbindungen. *Tetrahedron* **1967**, *23* (11), 4323–4329.
(187) Guo, Q.; Ford, G. M.; Hillhouse, H. W.; Agrawal, R. Sulfide Nanocrystal Inks for Dense Cu(In 1− x Ga x)(S 1− y Se y) 2 Absorber Films and Their Photovoltaic Performance. *Nano Lett.* **2009**, *9* (8), 3060–3065.
(188) Xia, D.; Li, J.; Xu, M.; Zhao, X. Electrodeposited and Selenized CIGS Thin Films for Solar Cells. *J. Non. Cryst. Solids* **2008**, *354* (12–13), 1447–1450.
(189) Pal, M.; Mathews, N. R.; Paraguay-Delgado, F.; Mathew, X. Phase Controlled Solvothermal Synthesis of Cu2ZnSnS4, Cu2ZnSn(S,Se)4 and Cu2ZnSnSe4 Nanocrystals: The Effect of Se and S Sources on Phase Purity. *Mater. Chem. Phys.* **2015**, *166*, 201–206.
(190) Shavel, A.; Arbiol, J.; Cabot, A. Synthesis of Quaternary Chalcogenide Nanocrystals: Stannite Cu 2 Zn x Sn y Se 1+ x +2 Y. *J. Am. Chem. Soc.* **2010**, *132* (13), 4514–4515.
(191) Chen, S.; Walsh, A.; Yang, J.-H.; Gong, X. G.; Sun, L.; Yang, P.-X.; Chu, J.-H.; Wei, S.-H. Compositional Dependence of Structural and Electronic Properties of Cu2ZnSn(S,Se) 4 Alloys for Thin Film Solar Cells. *Phys. Rev. B* **2011**, *83* (12), 125201.
(192) Riha, S. C.; Parkinson, B. A.; Prieto, A. L. Solution-Based Synthesis and Characterization of Cu 2 ZnSnS 4 Nanocrystals. *J. Am. Chem. Soc.* **2009**, *131* (34), 12054–12055.
(193) Reguig, B. A.; Regragui, M.; Morsli, M.; Khelil, A.; Addou, M.; Bernède, J. C. Effect of the Precursor Solution Concentration on the NiO Thin Film Properties Deposited by Spray Pyrolysis. *Sol. Energy Mater. Sol. Cells* **2006**, *90* (10), 1381–1392.
(194) Wang, K.-C.; Jeng, J.-Y.; Shen, P.-S.; Chang, Y.-C.; Diau, E. W.-G.; Tsai, C.-H.; Chao, T.-Y.; Hsu, H.-C.; Lin, P.-Y.; Chen, P.; et al. P-Type Mesoscopic Nickel Oxide/Organometallic Perovskite Heterojunction Solar Cells. *Sci. Rep.* **2015**, *4* (1), 4756.
(195) Scragg, J. J.; Kubart, T.; Wätjen, J. T.; Ericson, T.; Linnarsson, M. K.; Platzer-Björkman, C. Effects of Back Contact Instability on Cu 2 ZnSnS 4 Devices and Processes. *Chem. Mater.* **2013**, *25* (15), 3162–3171.
(196) Cui, H.; Liu, X.; Liu, F.; Hao, X.; Song, N.; Yan, C. Boosting Cu2ZnSnS4 Solar Cells Efficiency by a Thin Ag Intermediate Layer between Absorber and Back Contact. *Appl. Phys. Lett.* **2014**, *104* (4), 2–6.
(197) Chen, H.-J.; Fu, S.-W.; Wu, S.-H.; Tsai, T.-C.; Wu, H.-T.; Shih, C.-F. Impact of SnS Buffer Layer at Mo/Cu $_2$ ZnSnS $_4$ Interface. *J. Am. Ceram. Soc.* **2016**, *7*, n/a-n/a.
(198) Huang, S.; Luo, W.; Zou, Z. Band Positions and Photoelectrochemical Properties of Cu 2 ZnSnS 4 Thin Films by the Ultrasonic Spray Pyrolysis Method. *J. Phys. D. Appl. Phys.* **2013**, *46* (23), 235108.
(199) Boschloo, G.; Hagfeldt, A. Characteristics of the Iodide/Triiodide Redox Mediator in Dye-Sensitized Solar Cells. *Acc. Chem. Res.* **2009**, *42* (11), 1819–1826.